Title
THE MICROMECHANICS OF FRACTURE OF PEARLITIC STRUCTURAL STEELS

Author
Guest, Peter J.

Publication Date
1969-12-01

UCRL-19106
c. 2

THE MICROMECHANICS OF FRACTURE OF PEARLITIC STRUCTURAL STEELS

Peter J. Guest
(D. Eng.)

December 1969

AEC Contract No. W-7405-eng-48

LAWRENCE RADIATION LABORATORY
UNIVERSITY of CALIFORNIA BERKELEY

UCRL-19106

DISCLAIMER

TABLE OF CONTENTS

THE MICROMECHANICS OF FRACTURE OF PEARLITIC STRUCTURAL STEELS

Peter J. Guest

Inorganic Materials Research Division, Lawrence Radiation Laboratory,
Department of Mechanical Engineering, College of Engineering,
University of California, Berkeley, California

ABSTRACT

Few quantitative investigations studying fracture and the related fracture properties of hot rolled ferrite-pearlite structural steels have been made. The intent of this investigation was to provide fracture toughness data that can be made available in structural specifications and applied in structural design as well as to understand the micro-characteristics of fracture. A mechanical and metallurgical analysis has been carried out on the pearlitic, martensitic and spheroidized carbide structures of plain carbon hypoeutectoid steels in the temperature range -320°F to +150°F. The quantitative measurement of the microcharacteristics associated with cleavage fracture were determined by the use of the stress wave emission technique, which essentially monitors the elastic wave produced by discontinuous crack movements. The measured mechanical properties were correlated with information obtained from optical and scanning electron microscopy techniques. The analysis shows that as the volume fraction of pearlite is increased from 0 to 1, the plane strain fracture toughness decreased by 65% at +70°F and by 61% at -320°F. The data showed there to be a $d^{-1/2}$ relationship between the plane strain fracture toughness and ferrite grain size. The micromechanical analysis showed that by increasing the volume fraction of pearlite from 0 to 1, the microcrack density increased by a factor of 8 at -100 F and by a factor of 9 at -320°F.

LIST OF SYMBOLS

K	stress intensity parameter describing the elastic stress field in the vicinity of the crack. The value of K at instability is referred to as the fracture toughness and is expressed as psi-in$^{1/2}$.
I	subscript denoting first or opening mode of fracture. Referred to as plane-strain condition.
C	subscript denoting critical value of any parameter.
σ_{UYS}	upper yield stress at 0.20 percent offset where indicated, psi.
σ_{LYS}	lower yield stress , psi.
σ_{UTS}	ultimate tensile stress, psi.
σ_f^*	true fracture stress, psi.
σ_{max}	maximum nominal stress, psi.
B	specimen thickness, in.
W	specimen width, in.
H_p	half specimen length, in.
a	1/2 crack length, in.
ν	Poisson's ratio.
E	Young's modulus.
P	applied load, lbs.
R	plastic zone size subscript β used to denote critical value of plastic zone size.
ρ	notch radius, in.
ω	notch flank angle, degrees

ϵ_L	Luder's band strain, in/in
ε_f	true fracture strain, in/in
$\dot{\epsilon}$	strain rate, second^{-1}
θ	temperature, degrees Kelvin
d	ferrite grain size diameter, in
V_{fp}	volume fraction of pearlite
S_p	inter-lamellar spacing of pearlite, in
CVN	Charpy V-notch impact absorbed energy, ft-lbs.
A	area of cross section at the ligament of a Charpy V-notch impact specimen, in^2
p.c.f.	plastic constraint factor
N_{SWE}	total number of stress waves emitted
g	acceleration, ft/sec^2
m.d.	microcrack density
nd	effective length of microcrack density zone, in
h	height of step created in the formation of river patterns, in
ℓ	length of river pattern, in
U	energy associated with crack extension, in-lb/in^2
e	length between load points, in

I. INTRODUCTION

Of the many types of steels available for commercial usage, hot rolled ferrite-pearlite steels are the most commonly used in structural applications. These applications such as structural members, pipe lines and pressure vessels require a high resistance to unstable fracture and high strength to weight factors. The ferrite-pearlite steels can be heat treated to meet these requirements. Although these steels are of commercial and research interest and information is available in structural design regarding strength to weight ratios, few quantitative investigations studying fracture and the related fracture toughness properties have been made. Hence, fracture toughness data which can be related to structural design are not presently available in structural specifications. Charpy impact data on energy absorption are often available but cannot be directly related to structural design. The fracture mechanics approach used in this investigation allows the quantitative determination of fracture toughness in terms of the mechanical and microstructural parameters present.

The main purpose of this investigation was to analyze ferrite-pearlite steels in terms of their microstructure and determine the relevant fracture properties. As these steel systems are so complex, the metallurgical and mechanical effects, and environmental conditions were varied so that a quantitative study of the separate variables was possible. The microstructure was controlled through heat treating and the structures studied are of a pearlitic, martensitic and spheroidized carbide nature. The mechanical effects are those pertaining to the tensile and fracture loading conditions. The testing temperature was varied between 70°F and -320°F in order to study the environmental effects.

The fracture toughness for all structures was determined by using the fracture mechanics approach. Although fracture mechanics was developed and has been used for evaluating fracture toughness[1-3] of high strength steels, this technique is used in defining the plane strain fracture toughness, K_{IC}, which is a basic material property, applicable to the materials studied. The critical stress intensity was interpreted in terms of the specimen thickness and the plastic zone size. Use was made of a standard fracture specimen[4] and methods of fracture testing.

A primary object of this investigation was to develop a fracture criteria based on the tensile and fracture properties determined in the study, which will describe macroscopic crack propagation behavior in terms of thermomechanical treatments and metallurgical effects. Recently, attempts have been made in the development of fracture theories pertaining to specific areas. Hahn and Rosenfield,[5,6] Averbach,[7] and Tetelman et al.[8] have attempted to explain gross macroscopic behavior as observed in fracture toughness and Charpy impact tests. Smith[9] has outlined the general prerequisites for any model of cleavage fracture. As there are certain contradictory aspects to these proposed theories, one of these, that of Hahn and Rosenfield, is examined in detail and used to develop from the observed data a fracture criterion. This criterion relates microstructural contributions of structure and grain size to the environmental conditions and mechanical properties as yield stress and plane-strain fracture toughness. The criterion is applicable to hypoeutectoid plain carbon steels with yield strengths ranging from 25,000 psi to 70,000 psi. This means that if the yield stress at room-temperature is known, then values at other temperatures and structural conditions can be calculated. Similarly this applies for the true fracture stress

and fracture toughness properties. Included in the criterion is the plastic constraint factor, p.c.f., which describes the effect of triaxility at the tip of a notch on the elevation of the yield stress.[6]

Since there is a vast amount of Charpy V-notch impact data, CVN, currently available, an attempt was made to describe the existence of a correlation between CVN and K_{IC}. Also the dangers of converting one set of data to another without regard to microstructural conditions are emphasized. Recent correlations of Rolfe et al.[10] and Wells[11] are examined in terms of their development and application to the data obtained in this investigation.

The stress wave emission technique[12-14] was used in the study of the fracture process. This relatively new technique monitors the elastic wave produced by discontinuous crack movements. Further, it was shown how a quantitative measurement of these waves can be related to and used in determining some micro-characteristics associated with cleavage fracture. These microcharacteristics pertain to microcrack formation in the critical plastic zone at the notch root. Determination of the number of microcracks was accomplished with the stress wave emission technique. Tetelman et al.[15] used the probability of microcracking in the critical zone as part of a fracture criterion. In this investigation, the microcrack density concept was used to describe the microstructural region over which microcracking occurs prior to fracture. As part of a fracture criterion a relationship relating the number of stress waves emitted to this microstructural region is presented.

Optical microscopy and scanning electron microscopy techniques were used to provide information to correlate with measured mechanical properties. Also, observations of fracture surface fractographs were made

in conjunction with the measured stress wave emissions to assist in analyzing the microdynamics.

II. EXPERIMENTAL

A. Program

Structural steels in the hot rolled condition of varying carbon content from 0.19%C to 0.78%C were obtained commercially. This was done to ensure this study was carried out on materials that are being commonly used in structural applications. The range of carbon content, was selected so that the volume fraction of pearlite could be varied. The effects of interlamellar spacing were studied over the available range of percentage pearlite.

The preparation and testing program consisted of three primary phases, the material preparation and heat treatment to obtain the desired structure, the mechanical testing to determine the mechanical and fracture properties and thirdly, the microscopic evaluation of these properties by the use of the scanning electron microscope (S.E.M.).

Although the main purpose of this study was the analysis of the ferrite-pearlite structure in terms of their microdynamic behavior, the martensitic and spheroidized structures were also studied, but in less detail. These latter structures enable a comparison between the properties of structural steels to be made, where the carbon was contained in lamellar plates, dispersed as spheroids or in the form of lens shaped needles.

B. Material Preparation

The chemical composition of the steels obtained are listed in Table I. Four different carbon levels were purchased while the decarburized steel was obtained by decarburizing part of the 1019 carbon steel. The decarburization was performed by melting the 1019 C steel in a vacuum furnace and allowing wet hydrogen to be bled in as

the decarburizing atmosphere at 1750 °C for 72 hours. The furnace was purged with helium gas before and after the decarburization. Except for the 1040, the Cr-Mo-Ni contents were approximately the same. In this report the steel number listed is the reference number to the carbon content of the particular steel.

1. Fabrication

All material obtained was in the form of hot rolled bar, 1 in. thick by 2-1/2 in. wide, each steel bar being 10 ft long.

Standard Charpy V-notch and tensile specimens were machined from the bars with the tensile axis in the rolling direction and the "V"-notches cut at right angles to the rolling direction. The tensile specimens used were according to ASTM designation: E8-65T and are shown in Fig. 1

Fracture specimens were also machined from the bars with the tensile axis in the rolling direction or longitudinal direction. The fracture specimen design used was a modified wedge-opening-load (WOL) type to facilitate two pin loading and is shown in Fig. 2 . This specimen design is often referred to as the compact tension specimen for fracture testing which is discussed by Wessel[4] and for which the stress intensity factors were determined by Srawley and Gross.[16]

2. Heat Treatment

The machined specimens for all mechanical testing were first austenitized at 900°C for 30 minutes before quenching to the desired isothermal temperature. To obtain fine pearlite, specimens were quenched in a barium choride salt bath, held at 550°C for 15 minutes, and finally water quenched. To obtain coarse pearlite, the salt bath temperature was varied due to the variation in alloy content of the steels. Rinebolt[17] and time-temperature-transformation curves were referred to in order to correctly ascertain the salt bath temperatures. For the decarburized steel and the 0.19% carbon level the isothermal temperature used was 650°C for 60 minutes; for 0.43% carbon, 625°C for 30 minutes; for 0.56% carbon, 650°C for 15 minutes; for 0.78% carbon, 675°C for 30 minutes.

The isothermal temperature for the 0.43 and 0.56% carbon levels were lower than normally could be selected as the effect of alloying elements Cr and Ni in the 0.43% carbon steel and perhaps Mn in the 0.56% carbon steel served to suppress the transformation curves in each case. Figures 3 and 4 show the microstructure of the carbon steels heat treated to obtain fine pearlite and coarse-pearlite respectively.

Martensitic structures were obtained in all cases by quenching rapidly into an iced brine solution after austenitizing at 900°C for 30 minutes. Figure 5 shows examples of the martensitic structures obtained for 0.19% carbon and 0.78% carbon steels.

The spheroidized carbide structure, Fig. 6 , was obtained by tempering the quenched steel by reheating at 700°C for 4 hours followed by an oil quench.

C. Mechanical Testing

1. Tensile Testing

Tensile tests were carried out to determine the tensile properties on all the structures treated in this research. These tests were performed at a crosshead speed of 0.002 in./sec at both room temperature and the liquid nitrogen temperature. Additional tests were performed, with the tensile specimen immersed completely in an alcohol-dry ice mixture at a temperature of -95°F, for the fine and coarse pearlitic structures. At the low test temperatures, the tests were only run when the baths became quiescent and thermal contractions had ceased.

All tensile tests were performed on a Materials Testing Systems (M.T.S.) 300 kips capacity universal testing system.

The tensile properties of steels with all structures were determined by testing specimens having the design shown in Fig. 1. When the upper and lower yield points were not clearly defined, the stress corresponding to 0.2% offset was used.

2. Charpy Impact Testing

The impact properties were determined by testing a total of 40 standard Charpy V-notch specimens at room temperature and at liquid nitrogen temperature for the pearlitic, martensitic and spheroidized structures. Tests at -100°F were also performed for the fine and coarse pearlitic structures. The tests were performed on a pendulum-type impact testing machine adjusted to 120 ft-lb capacity. The criteria used from these tests were energy absorbed to fracture and fracture appearance.

3. Fracture Testing

Fracture tests were performed on single edge notched 1 in. thick specimens at a specimen extension rate of 0.01 in./sec. The fracture properties

were determined using approximately 100 specimens. All these tests were performed on the 300 kips capacity M.T.S. machine which is illustrated in Fig. 7, including the fracture specimen set up and related instrumentation for room temperature testing. The thickest specimens possible, considering the plate thickness, were utilized realizing that even in these, the thickness would not be adequate for plane strain conditions at higher temperatures. Plane strain conditions and hence an accurate value of stress intensity was obtained at the lower temperatures with the specimen thickness utilized.

This specimen design accommodates two pin loading for increased ease of preparation and testing over the WOL (wedge-opening-loaded) type from which it was developed. The stress intensity coefficient $\frac{KBW}{P}^{1/2}$, where B is the specimen thickness and W the specimen width, for this design, was determined by Srawley and Gross (16) using the boundary collation procedure, the results of which are in excellent agreement with published experimental compliance data (4) for this specimen configuration. The results of this procedure, in terms of

$$\frac{K_{I.Crit}BW^{1/2}}{P_{Crit}} = f\left(\frac{a}{w}\right) \qquad (1)$$

where P is the critical applied load, a is the specimen crack length and $f(\frac{a}{w})$ is the correction function due to the finite specimen width, were used in determining the plane strain critical stress intensity factor, $K_{I.Crit}$ for all fracture tests performed in the course of this study. In Fig. 8, $\frac{w}{H_p}$ ratios of 1.25 and 1.5 are shown where H_p is half the specimen length. In this study the $\frac{w}{H_p}$ ratios varied between 1.25 and 1.5. This figure was derived from boundary collocation procedures referred to in Reference 16.

All fracture specimens were pre-fatigue cracked at a sufficiently low load to allow a minimum of 10,000 cycles to grow the fatigue crack, at a cycling rate of 6 c/sec. This minimized the fatigue effect on the bluntness of the crack tip which should be as sharp as possible for low-temperature testing. The flaw so introduced simulated those flaws commonly found in assembled engineering structures.

The test procedure used for the high temperature tests consisted of immersing the specimen in hot water and allowing the temperature to stabilize by allowing it to cool slowly from a higher temperature. The equipment is shown in Fig. 9. The temperature was monitored by thermometer and thermocouple connected to the specimen. Only when the desired temperature was attained was the test started.

The test procedure for the low temperature tests made use of an apparatus built and adapted to this form of testing after that described by Wessel and Olleman.[19] The test set up and apparatus is shown in Fig. 10. The apparatus makes use of nitrogen vapor as both the refrigerant and testing medium so that predetermined low termperatures, such as -100°F and -200°F used in this research, were readily obtained and accurately stabilized with an automatic control and recording system. The refrigerant in the form of nitrogen vapor is allowed to enter the test chamber, by way of a flow regulating system, through the copper coil wound around the grips and specimen and escapes into the chamber through the perforations in the coil close to the specimen. A string of three control thermocouples installed on the specimen top, notch and bottom face areas are connected to the potentiometer-type temperature controller. This controller energizes and opens or de-energizes and closes the magnetic needle valve according to the thermocouple signals.

At liquid nitrogen temperature the specimen was immersed and as in

all cases of low temperature testing the test was only run when thermal contractions had ceased and the medium became quiescent.

Instrumentation for the fracture tests included a crack opening displacement (C.O.D.) gauge, discussed by Srawley and Brown,[18] which was used to monitor the crack opening with increasing load. The COD gauge is a double cantilever beam type gauge positively mounted as illustrated in Figs. 8 and 11 with resistance strain gauges epoxy resin bonded to the arms to form a bridge arrangement. The output of the gauge was monitored continuously on a high speed strip chart recorder as was the corresponding load. Also, the gauge output was monitored together with load on an X-Y recorder.

4. Stress Wave Emission Technique

The stress wave emission technique developed by Green et al.[12-14] was utilized to study the dynamic behavior of slow crack propagation in the single edge notched (SEN) specimens. Elastic waves are caused by the discontinuous growth of a crack before catastrophic failure and by the use of a suitable piezoelectric transducer attached to the specimen these emissions can be detected. For specimens as thick as those used in this study, this technique provides a sensitive method for acquiring information on the crack growth before catastrophic cleavage.

The set up is shown schematically in Fig. 12 and Fig. 13 shows the complete instrumentation used and the related circuitry in analyzing the generated signal of the piezoelectric transducer. In order to realize the best possible data, care was taken to set up the equipment to obtain the most effective characteristic responses of the components and hence eliminating extraneous noise signals.

Under increasing load and changes in environmental conditions an elastic

wave produced by crack movement is initiated. Associated with this crack advance is a small amount of energy release. As these generated signals are small, amplification is required and a filter used to filter out extraneous noise signals. An Endevco accelerometer, model 2234E, was used as the piezoelectric transducer which had a sensitivity of 59.4 picocoulomb/g and major resonant frequency of 32 KHz. Referring to the schematic, Fig. 12 , the signal from the accelerometer corresponding to a stress wave emission was amplified by a charge amplifier and the gain increased by a voltage amplifier. The amplified signal was then passed through the band pass filter set for low pass of 40 KHz and high pass of 25 KHz which effectively filtered hydraulic noise and other low frequency signals. The filtered signal was then fed in parallel to the Ampex recorder which had a maximum frequency response of 40 KHz at 15 in./sec and the oscilloscope screen for observation. At the conclusion of each test, the recorded signal was played into the oscillograph at 1-7/8 in./sec (one-eighth of the recorder speed and hence one-eighth of the highest recorded frequency of 40 KHz) so as to be accommodated by the frequency response of the galvanometer (5 KHz). The combined effective gain of the system used was between 450 and 45,000 comprising the charge amplifier gain at 1 g of approximately 150; the tape recorder gain of approximately 3 and the voltage amplifier gain of 1 to 100. The procedure described was established in this manner so that many tests could be carried out in succession.

D. Microscopy

1. Metallography

Microstructures of the materials investigated were determined by using standard metallographic techniques. These fine and coarse pearlitic

microstructures are shown in Figs. 3 and 4 ; while those of the martensitic and spheroidized carbide structures are shown in Figs. 5 and 6 .

These microstructures, for the pearlitic structures, were used in determining the average ferritic grain size, the volume fraction of pearlite and the average interlamellar pearlite spacing.

The method employed to determine the pearlite content was by point counting and the ferritic grain size and interlammelar spacing of pearlite by lineal analysis.[20] For the former, a plastic transparency containing very small dots was superimposed on a photomicrograph at 400× magnification and the number of dots falling on the pearlite colonies was counted. The percentage of pearlite calculated is the volume fraction of pearlite. The lineal intercept method involves the determination of the number of ferritic grain boundaries intersected along a series of straight lines superimposed on a photomicrograph at 400× magnification. The ratio of the total distance of traverse to the total number of intercepts gives the mean intercept grain diameter. The interlamellar spacing of pearlite was determined by counting the lamellae intersected along a number of equal straight line traverses of the pearlitic colonies superimposed on the photomicrographs at 1000× magnification. The ratio of the length of traverse to the number of intersections is the mean interlamellar pearlite spacing.

The specimens were cut from the tensile specimens unstrained area and after wet grinding in several stages to a finish equivalent to number 600 paper were micropolished on a rotary wheel in a solution of distilled water and .05μ alumina. The specimens were then etched for 5 to 10 secs with Nital[21] (1.5 ccs of nitric acid and 100 ccs of alcohol).

carbon content. Referring to the tables, the stresses were calculated using the load-displacement tensile charts and in particular the true fracture stress was computed using A_f, the cross sectional area at fracture. The true fracture strain, ϵ_f^*, was computed by using the following relationship $\ln \left(\frac{A_o}{A_f} \right)$ where A_o is the initial cross sectional area. The percentage elongation values (and Luders band strain, ϵ_L) were measured from the load-displacement charts. Referring to the figures, it is seen that, in general, the yield strength is higher for fine pearlite than for coarse. This increase is further accentuated as the volume fraction of pearlite is increased. The grain size effect is noticeable in these figures, particularly Fig. 18 where the true fracture stress for the 1000 carbon steel is much less than those succeeding values up to a volume fraction of pearlite of 1.0. It can also be noted in the tables that the fine pearlite structure exhibits greater reduction of area than the coarse pearlite, particularly as the carbon content level is increased. This was shown by Gensamer et al.[22] when he noted that the coarse pearlite structures were lower in ductility. Butcher and Petit[23] observed that the main reason for the ductility of pearlite is the discontinuous nature of the cementite lamellae and the small ratio of the amount of cementite to the amount of ferrite. It is noted that as the volume fraction of pearlite is increased the tensile strength increases more than the yield strength. Burns et al.[24] in their investigation of the fracture characteristics of ferrite-pearlite structures showed this to be due to a greater work hardening rate in pearlite.

The tensile properties obtained are all within the experimental ranges common to these materials. The yield strength values for the 0.43%

carbon steel was observed to be high in comparison to the other carbon steels studied. Tetelman and McEvily[25] showed the effect of certain alloying additions in the flow stress of ferrite to effectively increase the strength levels of carbon steels. Although the 0.43% steel studied had somewhat larger amounts of P, Si, Cu, Cr, Ni, Mo and V, the effect of these additional amounts might only account for an increase in the strength level of about 6000 psi. This does not fully explain the high yield strength value obtained. The anomalous behavior of this particular steel with respect to its yield strength is therefore noted.

The tensile properties for the martensitic structures were observed to be very low except in 0.19% carbon steel. This was due to the premature failure of some of the tensile specimens during testing as a result of quench cracks in the materials. These quench cracks were prevalent in the 0.78%, 0.56% and 0.43% carbon steels.

The yield strength of the spheroidized carbide structure was observed to increase with increasing carbon content. This is shown in Fig. 19 plotted at -320°F. Throughout, the tensile properties of the spheroidized carbides were superior to those of the pearlitic structures. It is thought that the dispersed carbide particles helped prevent long-range dislocation movement, but unlike the lamellae prevalent in pearlitic structures, fewer severe stress concentration sites were available for the initiation of fracture. Only specimens devoid of quench cracks were used in determining these properties.

2. Charpy V-notch Impact Observations

The measured results of the Charpy impact tests are tabulated in Table VIII for the structures studied at -320°F, -100°F and +70°F. It can be seen that there is no significant change in the absorbed energy values as

the pearlite spacing is varied from coarse to fine. The recorded energy values for the 0.19% carbon steel at 70°F are low because the true values exceeded the capacity of the machine used. Rinebolt[17] has shown that for similar structures these values should vary between 140 and 200 ft-lbs. The 120 ft-lb machine limitation caused the recorded values to be low.

3. Fracture Observations

Table IX summarizes the results of the fracture toughness tests performed as varying temperatures between -320°F and 150°F on the pearlite structures studied. Figure 20 illustrates these results at -320°F, -100°F and 70°F as a function of the volume fraction of pearlite while Figs. 21-24 summarize the fracture toughness results for all structures plotted as a function of temperature.

Referring to Figs. 21 through 24 the fracture toughness parameter shown plotted is the critical value of fracture toughness of the materials. The temperature dependence of K_{IC} is clearly illustrated. Contrary to the sharp transition normally illustrated in Charpy-V-notch impact data plotted as a function of temperature, there is no clear transition temperature illustrated for K_{IC} data. Also shown on these plots is the dependence of K_{IC} on the size requirement of the test specimen in order to obtain valid K_{IC} data. Brown and Srawley[26] established that for strength levels of $(\frac{K_{IC}}{\sigma_{LYS}})$ for similar materials as studied here, the size requirement for B should be $B \geq 2.5(\frac{K_{IC}}{\sigma_{LYS}})^2$ where B is the specimen thickness. The effects of using this criterion on the fracture toughness data for the pearlite structure are shown in the figures. More recently Wessel[4] has shown that for materials of the same yield

strength levels as presented here, consistent results for K_{IC} might be obtained at levels as low as $B \geq \left(\frac{K_{IC}}{\sigma_{LYS}}\right)^2$. The effects of this criterion are also shown on the figures. Therefore, the fracture toughness data observed for all materials fall into three catagories. In the low temperature region, the fracture behavior is substantially elastic, and fracture occurs by cleavage. The middle temperature region exhibits significant plastic flow prior to cleavage, as evidenced by non-linearity of the load-displacement curve. In the higher temperature region, fracture was by cleavage, but only after a period of excessive slow crack growth. Hence, for this latter condition, the fracture toughness data are actually for K_C, and hence are higher than the true plane strain fracture toughness if one had plane strain conditions. This observed behavior is further illustrated in Figs. 25 and 26 which show the fracture surfaces of the fine and coarse pearlite structures at temperatures representative of the three aforementioned temperature regions, i.e., -320°F, 70°F and 100°F. At -320°F, there was no observed slow crack growth but only flat fracture typical of cleavage ahead of the fatigued region. The 0.19 and 0.43% carbon steel specimens shown tested at room temperature indicate a small ductile region evident of slow crack growth before cleavage occurred. Cleavage was the observed mode of fracture for 0.56 and 0.78% carbon steel at room temperature. For the higher temperature fracture tests, the 0.19, 0.43, and 0.56% carbon level steels shown an increased amount of slow crack growth, particularly in the 0.43% carbon steel, before cleavage occurred. The 0.19% carbon steel failed by tearing after excessive slow crack growth while the 0.78% carbon steel cleaved after a minimal amount of slow crack growth not evident in these figures.

In conjunction with the observations discussed above, Figs. 27-30

illustrate the behavior of fracture specimens of the 0.19 and 0.78% carbon steels under fracture tests conditions at +70°F, -100°F and -320°F. Here the load is shown as a function of crack opening displacement. At 70°F, the curves both exhibited a period of slow crack growth before cleavage occurred. At -100°F, only the 0.19% carbon steel revealed a period of slow crack growth before failure whereas the 0.78% carbon steel exhibited a linear load-displacement relationship preceding cleavage fracture. At -320°F, both steels exhibited linear elastic behavior prior to cleavage failure. In all cases the maximum load and crack length failure were used in computing the plane strain fracture toughness.

Various effects were observed as illustrated in Fig. 20 pertaining to pearlite spacing and percentage pearlite content. The fine pearlite structure was generally observed to have higher K_{IC} values than the coarse pearlite structures. The values of K_{IC} at the lower volume fraction of pearlite values are lower than would be expected in comparison to the K_{IC} data for the 0.56 and 0.78% carbon steels. This point is discussed in detail in a later section. Three illustrative temperatures, 70°F, -100°F and -320°F are shown plotted in Fig. 20.

The relative fracture toughness to yield strength levels as a function of volume fracture of pearlite is shown in Fig. 31, the data of which are tabulated in Table XI. At the temperatures shown, a broad spectrum of $(\frac{K_{IC}}{\sigma_{LY}})$ levels for the pearlitic structures is illustrated. The -320°F data are representative of the low toughness, brittle condition and the 70°F data is representative of the low strength, high toughness condition.

Referring to Figs. 21 through 24, the K_{IC} data for the martensitic structures are shown plotted together with the data for the pearlitic and spheroidized carbide structures. Table X also summarizes the measured

fracture properties of the martensitic and spheroidized carbide structures. The figures show that in all cases except the 0.19% carbon steel, the martensite structure exhibits lower fracture toughness than the pearlitic structures. As expected, only in the case of low percentage carbon content is the martensite very tough. Figure 32 shows the fracture surfaces of the 0.19, 0.43 and 0.78% carbon steels at 70°F and -320°F. It was not possible to obtain the K_{IC} for the 0.56% carbon steel as the single edge notch fracture specimens failed during fatiguing of fine cracks due to quench cracks at the pin holes. The fracture surfaces showed a cleavage mode of fracture, except for the 0.19% carbon steel where the shear lips illustrated the extensive amount of plastic flow which accompanied crack growth at 70°F.

The spheroidized carbide structures all were observed to exhibit higher K_{IC} values than the pearlitic structures. This is consistent with earlier observations by Gensamer et al.[22] who found the spheroidal structures markedly superior in ductility to pearlite of the same yield strength. At room temperature, the K_{IC} data for 0.19 and 0.43% carbon levels were unattainable due to the gross plastic deformation of the fracture specimens. Figure 33 illustrates the behavior of the spheroidized carbide structures as observed.

Figure 34 shows the K_{IC} data and true fracture stress, σ_f^* data for spheroidized carbide at -320°F plotted as a function of carbon content. As observed, K_{IC} and σ_f^* exhibit similar behavior patterns as the carbon content is increased. Hahn and Rosenfield[27] studied the effect of adding THO_2 particles to iron and showed the cleavage strength was increased over that of the base metal. This enhanced resistance was thought to be a

consequence of particles limiting the slip distance of dislocations and thus the ability of pile-ups to act as stress concentrators. The model presented, which predicts a maximum σ_f^* for the largest volume fractions and the smallest particle diameter, applies well for the data reported here to 0.56% carbon steel where the σ_f^* is a maximum and a further increase in the volume fraction of cementite shows a sharp drop in σ_f^*. Obviously there are many factors contributing to this effect, namely the size of the carbide particles, the dispersion of the particles and the ferrite grain size. Table II shows the ferrite grain size of the 0.19% carbon level to be four times that of the remaining three carbon levels which have the same ferrite grain size. Apparently there is a critical balance between the number of carbide particles present, their size and dispersion. The fracture behavior of spheroidized carbon steel is quite different where the fracture mode is of a ductile nature, as was shown by Liu and Gurland.[28,29] For low carbon steels (0.065 and 0.3%C), they found the true fracture stress at room temperature decreased as the volume fraction of carbide was increased. For high carbon steel (> 55%C), the critical parameter was the interparticle spacing with all compositions falling on the same curve which showed that the true fracture stress decreased with increasing interparticle spacing.

Hodgson and Tetelman[30] found that in similar fine microstructures of quenched and tempered structures the cleavage fracture stress increased with decreasing interparticle spacing. Also, the cleavage fracture stress increased with decreasing particle diameter. Similar effects were observed in this research and Fig. 34 shows σ_f^* first to increase with carbon content and then to decrease.

4. Stress Wave Emission Observations

All the fracture tests performed were instrumented to record the stress wave activity associated with crack growth. The stress wave emission records were analyzed for those tests run at -320°F for all the structures studied. These are tabulated in Table XIV. Data are presented in Table XV for coarse pearlite structures for tests performed at -200°F, while Table XVI contains data of fine and coarse pearlite structures for fracture tests performed at -100°F. Tabulated is information pertaining to the time duration, the number of waves observed, the wave amplitude range and the average stress wave amplitude in acceleration (g) units for 0 to peak. The recording sensitivity in acceleration (g) units is tabulated so as to explain why the average amplitude is computed when the sensitivity was low enough (0.5 g) to accommodate the recorded waves. Illustrative records are shown in Figs. 35-42 . These records clearly show the variation in amplitude and frequency of occurrence of the monitored stress waves for the structures studied. The wave amplitude is directly related to the size of the crack jump so the emission records qualitatively describe the nature of the discontinuous crack growth in the material. As illustrated in the figures, the stress waves during the period preceding cleavage fracture became more frequent and the wave magnitude was increased. Gerberich[31] has suggested a semi-empirical relationship as follows:

$$\Delta A \sim \frac{gEe}{2K^2} \qquad (2)$$

where ΔA is the incremental area swept out by the advancing crack, g is the stress wave 0 to peak amplitude, E is the material elastic modulus, e is the length between the specimen load points, and K is the applied

stress intensity factor. This indicates that as the wave amplitude is increased, the stress intensity is also increased for equidistant crack jumps until the critical stress intensity is reached at which point catastrophic failure occurs. From the data for 1019 carbon steel, K_{IC} = 40 ksi-in$^{1/2}$, g = 0.02 and 0.001 for the observed upper and lower bounds, e = 1.25 inches , m the constant of proportionality = 0.02 and E = 30×10^{6} psi.[31] The calculated incremental area swept out by the advancing crack represented by these two SWE amplitudes represent $\Delta A = 4.7\times10^{-6}$ and 0.23×10^{-6} inches.^{2} This corresponds to a circular grain diameter of 245×10^{-5} inches and 55×10^{-5} inches which is equivalent to the average grain size observed of 70×10^{-5} inches.

Figure 35 shows the wave record for 1000 carbon steel at -320°F. The large number of stress waves (N_{SWE} = 322) are indicative of the micro-crack behavior in the larger ferrite grains of the material. The magnitude of these waves indicate the relatively large crack jumps involved as the stress intensity factor associated with these jumps is low. Also the energy of the wave is related to the wave amplitude[12] in the form,

$$\Delta U \sim g \qquad (3)$$

hence the larger the wave magnitude, the more energy is associated with the crack jump. This is shown in Fig. 39 where the energy released with each crack jump for the martensitic structure, as indicated by the large wave amplitudes, is greater than the energy released with the crack propagation for the pearlitic structures.

The longer time period associated with tests of the spheroidized carbide structures (e.g. 25 seconds) shown in Fig. 41 , coupled with the stress wave behavior (e.g. 0.024 g, average amplitude) show

the discontinuous crack jumps to be larger than those of the pearlitic structures, (e.g. 20 seconds and 0.016 g average amplitude). This suggests the microcrack formation in the pearlite lamellae to be more dense, and hence more critical, than the microcracks formed at the spheroidal particle-matrix interface.

C. Microscopy Investigation

1. Metallographic Observations

Figures 15 and 16 illustrate coarse pearlite microstructures of 1000, 0.19, 0.43, 0.56, and 0.78% carbon steel tensile specimens tested at -320°F. These photomicrographs were taken of samples machined from the region and in the plane of the fracture surface. The 1019 carbon steel micrograph shows evidence of twinning in the ferrite grain while the remaining structures do not reveal any changes in the microstructure. Twinning is also evident in the micrograph of 1019 fine pearlite steel at -320F shown in Fig. 14. Figure 16 illustrates the large ferritic grain size of the 1000 carbon steel and also the gross twinning that occurred at -320°F. Similar behavior was observed by Hahn et al.[32] where mechanical twinning was found to be associated with cleavage fracture at low temperatures. Twinning is eliminated as the test temperature is raised as illustrated by the micrograph of 1000 carbon steel tested at -100°F.

Figure 3 and 4 reveal the wide range of pearlite spacings for both fine and coarse structures. In all cases the pearlite spacings, S_p, listed in Table I, are average values computed from typical areas of the structures. Also to be noted is the discontinuous nature of the cementite lamellae in the pearlite colonies. This is thought to be the main reason for the ductility of pearlite.

Figure 6 shows the spheroidized carbide structures for four carbon levels. The alignment of the particles clearly reveals the sites of the former martensitic needles.[33] The ferrite matrices are also evident, with the ferrite grain size for the 0.19% C steel being approximately four times that of the other three carbon steels.

Typical martensitic structures are shown in Fig. 5 where the prior austenitic grain size is visible in the 0.19% carbon steel; it is not visible in the 0.78% carbon steel. The martensitic structure for the 0.78% carbon steel is comprised of individual martensite needles of differing sizes and shapes.

2. Fractographic Observations

Scanning electron micrographs of typical features associated with fracture of carbon steels are shown in Figs. 45–53 . Figure 43 shows typical cleavage in pearlite and ferrite and in the case of 0.19% carbon steel tested at -320°F, the fine pearlite structure exhibits cleavage "tongues" which are uniquely associated with cleavage fracture[34] and are indicative of twinning in the ferrite. Burghard and Stoloff[35] show these tongues are formed when a cleavage crack, propagating along an {100} plane, is diverted along the {112} twin-matrix inferface of an intersecting twin while the main crack propagates around the twin. The steps bounding the tongue on three sides were formed by deformation and fracture of the ligament between the two local cracks. This final stage results in the rejoining of the diverted crack segment with the main crack which continues to propagate on the main cleavage plane. Although twinning was observed in the 0.19% C steel, coarse pearlite structure, (Fig. 15), an anomalous behavior was observed in that no cleavage tongues were present in the ferrite. (See Fig. 43d). However, "river patterns," characteristic of cleavage fracture were exhibited. Also to be noted is the sharp cleavage fatigue interface indicating no prior slow crack growth before cleavage. The 0.43% C steel, fine pearlite, tested at -320°F, shows in Fig. that in cleavage in pearlite, there were approximately 13 cleaved pearlitic lamellae involved with a single cracked region. Since this compared approximately to the size of a quarter of a grain in the 1019 steel, perhaps this is why the stress wave emission amplitudes do not vary a great deal when considering ferritic versus pearlitic microstructures. Figure 45 illustrates in the 0.56% C steel secondary cracking and also the

large number of pearlitic lamellae involved in cleavage of pearlite. The breaking up of pearlite indicates the high toughness of the structures. Figure 46 illustrates the linking of the pearlite colonies in the 0.78% C steel. Also there were approximately twelve cementite lamellae involved in a single region of cleavage fracture.

Figures 47–51 illustrate the fracture surfaces of 0.19, 0.43, 0.56 and 0.78% C steels tested at -100°F and 70°F. Evidence of plastically induced cleavage in the slow crack growth region is observed in the 0.19% C steel shown in Fig. 47 . Friedel et al.[36] have shown there to be a relationship between the step height and the length of the rivers contained in cleavage river patterns. This relationship is of the form

$$h^2 \propto \ell \qquad (4)$$

where h is the height of the step created and ℓ is the length of the river. Friedel[36] further explains the river pattern formation to be created by a random distribution of screw dislocations of opposite signs piercing the cleavage surface. Applying this relationship to the river patterns observed in Fig. 47 , it is observed that the step height is increased as the square root of the propagation distance measured from the source (see Fig. 54). While Friedel showed that the relationship for mild steel at -320°F was approximately $h^2 = 10\ell$, the present investigation showed that at 70°F, $h^2 \approx 120\ell$. This indicates that at room temperature the mechanism of fracture is quite different as there is twelve times the surface area involved during the step formation process. Friedel did not report room temperature tests, but suggested that higher energy absorption is associated with plastic deformation. The Charpy impact results in this investigation, where the energy absorbed to fracture was 1.5 ft-lbs at -320°F and > 120 ft-lbs at 70°F, are consistent with the

observations of fracture surfaces and suggestions by Friedel. The coalescence of the river patterns indicates the direction along which the rivers coalesce. Figure 48 illustrates the changes occurring in the crack path. The coalescence of the river patterns observed in the ferrite strip located between the pearlite areas indicates the crack path steps up, and it is also evident that less energy is expended in the fracture of the pearlite. Figure 49 shows the microcracks evident in the 0.19% C steel at -100°F. At this temperature no tongues are evident because no mechanical twinning occurred. Dimple rupture of both ferrite and pearlite is shown in the slow crack growth region of the 0.43% C steel. Figure 50 of 0.56% C steel indicates there were eighteen cementite lamellae involved in the cleavage of pearlite. The size of the cleavage steps were determined by counting the number of lamellae involved. The cleavage fatigue interface region also indicates the absence of slow crack growth prior to fracture at this temperature (-200°F) for 0.56% C steel. Comparing Figs. 51 to 46 for 0.78% C steel tested at 70°F and -320°F, respectively, reveals the fracture step within the pearlite colonies to be different. They were approximately 8μ and 14μ respectively. This shows that cleavage nuclei are small in area at room temperature. Cleavage in a tensile specimen at room temperature is more ordered than cleavage in the fracture specimen.

Figures 52 and 53 show fracture surfaces of 0.56 and 0.78% C steels tested at 100°F. Patterns of continually changing cleavage in pearlite were observed as shown in Fig. 52 for 0.56% C steel. This corresponds to a large change in fracture toughness for this material (65 ksi-in.$^{1/2}$ at +100°F to 40 ksi-in.$^{1/2}$ at -320°F). The pearlite colonies are broken up considerably compared with those at room temperature and -320°F. This indicates more energy had been absorbed in the fracture process.

Figure 53 shows cleavage steps and the many orientations of the pearlite colonies cleaved by the crack propagation.

IV. DISCUSSION

A. General

In order to study the micromechanics of fracture of structural steels, care must be taken in the consideration of the many parameters involved. In this respect one of them, the grain size effect, plays an important role in the strengthening of ferrite-pealite steels by increasing their resistance to cleavage fracture (Cottrell,[37] Petch,[38,39] Hahn et al.,[32] Tetelman and McEvily[25]). This results because the brittle fracture stress and yield stress are both raised by decreasing the grain size. The yield stress, σ_{LYS}, is also greatly affected by the temperature conditions, the material structure, the strain rate and the state of stress in the part. The true cleavage fracture stress, σ_f^*, although perhaps also temperature and strain rate independent, is very dependent on grain size. This discussion begins with the normalization of the variation in grain size of the materials studied so that in the following sections it may be shown how other variables affect the observed macroscopic crack propagation behavior.

Also discussed is the correlation of Charpy V-notch impact data (CVN) with plane strain fracture toughness data (K_{IC}) to illuminate the possibilities of converting existing CVN data to K_{IC} values for different material structures.

Also, the stress wave emission technique will be discussed in terms of its usage to help determine the microcharacteristics of fracture, whether these be grain by grain crack movements or the development of non-propagating microcracks.

B. Correction for Grain Size Effect

1. Development of a Corrected Value for Lower Yield Stress, σ_{LYS}

The grain size dependence of σ_{LYS} is described by the Hall-Petch[40,41] equation by

$$\sigma_{LY} = \sigma_i + K_y d^{-1/2} \qquad (5)$$

where σ_i and K_y are constants and d is the average ferrite grain diameter. During inhomogeneous yielding of pearlite-ferrite steels, both constituents undergo plastic deformation. Therefore any description of the lower yield stress should include as well the effect of the presence of pearlite. Kouwenhoven[42] describes the σ_{LY} of such steels in terms of a modified Hall-Petch relationship

$$\sigma_{LY_{(comp)}} = f_\alpha (\sigma_{i\alpha} + K_y d^{-1/2}) + f_p \sigma_p \qquad (6)$$

where f_α and f_p are the volume fractions of ferrite and pearlite, respectively, $\sigma_{LY_{(comp)}}$ is the lower yield stress for the ferrite-pearlite composite, $\sigma_{i\alpha}$ is the value of $\sigma_{i_{(comp)}}$ for a completely ferritic steel and σ_p is the value of $\sigma_{L_{(comp)}}$ for a steel with a completely pearlitic structure. Here $f_p = 1-f_\alpha$. The term $\sigma_{i\alpha} + K_y d^{-1/2}$ represents, here, the Hall-Petch equation for σ_{LYS} of a completely ferritic material.

Therefore an expression can be obtained which will correct the measured values of lower yield stress in terms of ferrite grain size and pearlite content for the structures studied. This can be expressed as follows:

$$\sigma_{LY_{(corrected)}} = \sigma_{LY_{(measured)}} - f_\alpha K_y (d^{-1/2} - d_{average}^{-1/2}) \qquad (7)$$

where $d_{avg}^{-1/2}$ is the average ferrite grain size of 0.19, 0.43, 0.56 carbon steels. The grain size of the 1000 steel was excluded from this

average. The result would have reflected a false average too close to that of the 1000 steel, since its grain size was nearly an order of magnitude larger than the rest. The values of K_y for a completely ferritic steel and for any combination of ferrite-pearlite were determined from slopes drawn through Kouvenhoven's data for steels ranging from 0.01 to 0.9 volume fraction of pearlite. These values were K_y = 820 psi-in$^{1/2}$ and 1000 psi-in$^{1/2}$ respectively.

2. Development of a Corrected Value for the True Fracture Stress, σ_f^*

The grain size dependence of the true fracture stress is associated with the Cottrell-Petch theory[36-39] where σ_f^* is proportional to $d^{-1/2}$ so that

$$\sigma_f^* = K_f\, d^{-1/2} \tag{8}$$

where K_f is a constant and d is the grain diameter. Since the theory does not account for observed values of K_y and that other factors apart from grain size also influence σ_f^*, a criteria for cleavage was developed from actual experiments. Hahn and Rosenfield[5] related σ_f^* to grain size d through a study of hypoeutectoid steels and determined two equations. One was for the case where $\sigma_f^* > \sigma_{LYS}$ and the other was for $\sigma_f^* = \sigma_{LYS}$ giving

$$\sigma_f^* = [30{,}000 + K_f\, d^{-1/2}][1 + \epsilon^*];\ \sigma_f^* > \sigma_{LYS} \tag{9}$$

where K_f is 2980 psi-in$^{1/2}$ and

$$\sigma_f^* = 50{,}000 + K_f\, d^{-1/2};\ \ \sigma_f^* = \sigma_{LYS}\ . \tag{10}$$

In Eq. (9), ϵ^* is the engineering strain preceding fracture. The other symbols are as before.

Therefore, an expression can be determined which will correct the

measured true fracture stress values in terms of the grain size. This can be expressed as follows,

$$\sigma_{f^*_{(corrected)}} = \sigma_{f^*_{(measured)}} - K_f[1+\epsilon^*][d^{-1/2} - d_{avg}^{1/2}] \qquad (11)$$

3. Application of Corrections

The corrected values of σ_{LYS} and σ_f^* are tabulated for the pearlitic structures in Tables III through VII. These corrections are also illustrated in Figs. 55 and 56 for σ_{LYS} and σ_f^* as a function of the volume fraction of pearlite, respectively.

Considering Fig. 55 first, it can be seen that the lower yield stress is dependent on the pearlite content and probably on the inter-lamellar spacing as well as on temperature. As the strain rate in all tensile specimens was the same, no dependency on rate was determined. The dependency on the pearlite spacing, although secondary to grain size, is greater as the pearlite content is increased. This effect is accentuated at lower temperatures. Puttick[43] has shown that plastic flow can be nucleated at the ends of cementite plates and that deformation is accommodated by fine slip in ferrite parallel to the lamellae where the resolved shear stress is sufficiently high. This indicates that the length of pearlite colonies should also determine the mechanical properties of pearlite as well as the pearlite spacing. Also, the coarser the inter-lamellar spacing the more likely slip is to occur parallel to the cementite plates.

Figure 56 shows a slight dependency on the volume fraction of pearlite of the true fracture stress and a better defined dependency on the pearlite spacing at -320°F. The true fracture stress should be independent of temperature[5] except for modulus changes. The effect of

the increasing pearlite content is to provide an increasing number of strain-concentration sites and hence more favorable fracture initiation sites for cleavage.[44] The finer pearlite spacing serves to increase the fracture resistance. However, both of these effects must not be greatly reflected in the cleavage fracture stress since it is nearly independent of all parameters.

C. Development of Semi-Empirical Equations

1. Derivation of Theoretical Yield Stress

Hahn and Rosenfield[5] determined a semi-empirical relationship that accurately described data for a fine grained mild steel (12 μ diameter) in which σ_{YS} is given as a function of strain rate and temperature. This relationship is as follows,

$$\sigma_{LYS} = \sigma_{LY_o} + 195{,}000 \text{ psi} - 11{,}000 \text{ psi } \theta^{1/2} + 8{,}000 \text{ psi } \log \dot{\epsilon} \quad (12)$$

where $\sigma_{LY_o} = 52{,}600$ psi is the static yield stress at room temperature for a strain rate, $\dot{\epsilon}$ of 10^{-3} per second; θ is the temperature in degrees Kelvin and $\dot{\epsilon}$ is the strain rate in sec^{-1} units.

An advantage of a relationship of this form is that the contributions of strain rate and temperature are separated from metallurgical factors. As the majority of Hahn and Rosenfield's data were for a 0.39 volume fraction of pearlite, the grain size dependence was not included. However, Kouvenhoven's study provides the necessary information and enables the grain size dependence to be included. A slope $d^{-1/2}$ versus yield strength drawn through Kouvenhoven's data for volume fraction of pearlite ranging from 0.1 to 0.59 can be represented by

$$\sigma_{LYS} = 6200 + K_y d^{-1/2} \quad (13)$$

where K_y = 1,000 psi-in.$^{1/2}$. Here σ_{LYS} is synonymous with σ_{LYS_o} as given in Eq. (12). Combining these equations (12) and (13) the following relationship is obtained,

$$\sigma_{LYS_{\theta,\dot{\epsilon}}} = 201{,}200 + K_y\, d^{-1/2} - 11{,}000 \text{ psi } \theta^{1/2} + 8000 \text{ psi } \log \dot{\epsilon} \tag{14}$$

In this research, the strain rate was kept constant. However, other factors pertaining to the material structure can be introduced into such a relationship as Eq. (14) based on the data accumulated. The relationship derived from the plot of the corrected values of σ_{LY} as a function of volume fraction of pearlite in Fig. 55 is as follows,

$$\sigma_{LYS_{\theta,\ V_{fp},d,S_p}} = f_\alpha \left[125{,}000 + K_y d^{-1/2} - 7{,}060\ \theta^{1/2}\right] + f_p \left[200{,}000 + 300\ S_p^{-1/2} - 11{,}000\ \theta^{1/2}\right] \tag{15}$$

where K_y = 820 psi-in.$^{1/2}$ for a completely ferritic microstructure and K_y = 1000 psi-in.$^{1/2}$ for a ferrite-pearlite steel; S_p is the pearlite spacing and the other symbols are as previously described. This derivation describes the effect on yield stress of the grain size, the temperature change, the inter-lamellar spacing and the pearlite content.

2. Derivation of the Theoretical True Fracture Stress

Since the true fracture stress is independent of temperature and strain rate the only parameters described by the data to be included as dependencies are the grain size, the inter-lamellar spacing and pearlite content. Equation (9) includes the grain size effect. Therefore using this equation, the following derived relationship describes the accumulated

data relating the true fracture stress to the volume fraction of pearlite as shown in Fig. 56

$$\sigma^{*}_{f_{V_{fp},d,S_p}} = f_\alpha [30{,}000 + K_f\, d^{-1/2}][1 + \overset{*}{\epsilon}] + f_p[63{,}000 + 500\, S_p^{-1/2}] \qquad (16)$$

where the symbols used are as previously described and $K_f = 2980$ psi-in$^{1/2}$.

3. Development of the Plastic Constraint Factor

An important feature of the crack extension mechanism is the stress intensification and triaxiality existing ahead of a sharp crack loaded under plane strain conditions. First consider the plastic constraint developed by plastic yielding at a notch. Hill[45] originally showed that the stress is elevated at the tip of the notch due to plastic constraint, as given by

$$pcf_{max} = \frac{\sigma_{max}}{\sigma_{YS}} = [1 + \frac{\pi}{2} - \frac{\omega}{2}] \qquad (17)$$

where σ_{max} is the maximum nominal stress and σ_{YS} is the yield stress and ω is the flank angle of the notch. For a straight cut as in a crack, $\omega = 0$ and the maximum plastic constraint factor is 2.57 for the Tresca yield criterion and 2.82 for a Von-Mises yield criterion. Under the set of circumstances where crack nucleation just below the crack tip leads to unstable cleavage fracture, Hahn and Rosenfield[6] have defined the value of the constraint factor which can be calculated from σ_f^{*}:

$$\sigma_{max} = \sigma_f^{*}$$
$$pcf = \frac{\sigma_f^{*}}{\sigma_{YS_{\theta,\dot{\epsilon}}}} \qquad (18)$$

where $K = K_{IC}$

where $K = K_{IC}$ signifies the equations to be valid just prior to crack extension and $\sigma_{YS}{}_{\theta,}$ is that associated with the temperature and strain rate conditions at the crack tip. To be noted is that pcf can only range between one and pcf_{max}. This equation represents a failure criterion and by describing the plastic constraint factor and the cleavage fracture stress in terms of the loading conditions and microstructural parameters, this then represents a criterion for cleavage fracture. Hahn and Rosenfield analyzed Krafft's[46] data on the critical stress intensity to propagate a crack in mild steel at low temperature and high strain rates and found that the plastic constraint factor varied with the stress intensity to yield stress ratio by

$$pcf = 1 + \beta \frac{K}{\sigma_{YS}} \tag{19}$$

where β is a constant of about 2 inches$^{-1/2}$.

This relationship indicated that at at pcf of unity or $\sigma_f^* = \sigma_{YS}$, the fracture toughness would be zero whereas at low temperatures and $\sigma_f^* = \sigma_{YS}$ there exists a finite value for K_{IC}, as borne out by Low and as shown in this investigation. To determine a relationship that would more correctly relate the plastic constraint factor to the stress intensity-yield stress ratio, the data gathered in this investigation were plotted as shown in Fig. 57. The following modified equation was obtained:

$$pcf = \delta\left(\frac{K_{IC}}{\sigma_{LYS}}\right)^{1/2} - 0.4 \tag{20}$$

where δ is a constant of about 2.8 inches$^{-1/4}$.

This equation together with Eq. (18) gives the failure criterion.

As seen in Fig. 57 a finite value of stress intensity is obtained when $\sigma_f^* = \sigma_{LY}$ and the pcf values at high $\frac{K_{IC}}{\sigma_{LYS}}$ values are still within the theoretical criterion.

Further, for the type and structure of the carbon steels studied in this investigation, Eqs. (15, 16, 18, and 20) provide a fracture criterion. Although it is recognized that the analysis is of a semi-empirical nature the experimental results obtained and their interpretation support the approach taken. Other criterion of cleavage fracture (7-9) attempt to explain gross macroscopic fracture behavior as observed in fracture toughness and Charpy impact tests and some of these are considered in a later section.

D. Discussion of Fracture Criteria

1. Application to Fracture Toughness

Table XII contains data pertaining to the calculated values of plane-strain fracture toughness, K_{IC}, using Eq. (20). In conjunction, Eqs. (15) and (16) were used to calculate the lower yield stress, σ_{LYS}, and true fracture stress, σ_f^*. Figure 58 shows the data plotted at -320°F, -100°F, and 70°F as a function of the volume fraction of pearlite, V_{fp}. Comparing this figure with Fig. 20 of the measured values, it can be seen that the calculated K_{IC} values rise sharply at low values of V_{fp}. Use of Eq. (20) predicts K_{IC} correctly and the differences between the measured K_{IC} values and the calculated ones for 1000 and 1019 carbon steels are accentuated. That is, the average grain size used in calculating K_{IC} was about equal to that for the 1043 and 1056 carbon steels, but was much smaller than that for the 1000 and 1019 carbon steels. If fine grained 1000 and 1019 carbon steels had been tested, the observed fracture toughness values would have been

much greater. The values of K_{IC} are approximately those of the measured values of K_{IC} for 1056 and 1078 carbon steels for all temperatures shown. In all cases there is a secondary effect shown due to the pearlite spacing. The fine pearlite structure consistently has calculated K_{IC} values higher than those of the coarse pearlite structure. This is further shown in Fig. 59 where the calculated K_{IC} values are plotted as a function of the interlamellar spacing, $S_p^{-1/2}$. The effect is apparently secondary as the actual $S_p^{-1/2}$ values obtained from the data are 165 in.$^{-1/2}$ for the coarse pearlite and 190 in.$^{-1/2}$ for the fine pearlite, corresponding to K_{IC} values of 35 ksi-in.$^{1/2}$ and 39 ksi-in.$^{1/2}$, respectively. This difference in K_{IC} values is hardly of importance; the effect of the pearlite content is of much greater significance as is the temperature effect.

The importance of the ferrite grain size effect for low carbon steels is illustrated in Fig. 60, the data for which are tabulated in Table XIII. The two curves shown in Fig. 60 are those for 0% and 23% pearlite structures at -320°F. Also shown plotted are actual K_{IC} values for 1000 and 1019 fine and coarse pearlite structures as a function of $d^{-1/2}$. The data were obtained by calculating K_{IC} from Eq. (20) and σ_{LY} and σ_f^* from Eqs. (15) and (16), respectively. The ferrite grain diameter values, $d^{-1/2}$ of 16, 36.7 and 50 in.$^{-1/2}$ are those averaged from the fine and coarse pearlite structures of 1000, 1019, and 1043 carbon steels, respectively. To be noted is that an average pearlite spacing of $Sp^{-1/2} = 213$ for the 1019 fine and coarse pearlite structures was used in Eq. (15) and (16). The slope of the calculated curve for 0% pearlite is steeper than that of 23% pearlite indicating the effect of the increase in pearlite content. Increasing pearlite content serves to suppress the slope of the K_{IC} grain size relationship due to its effect

on the σ_f^*/σ_{LYS} ratios at the various grain sizes.

2. Correlation of Charpy Impact and Fracture Toughness Properties

Although the plane strain fracture toughness of structural materials can be related to structural design, K_{IC} values are not presently included in structural specifications. However, Charpy impact test results are found in various toughness specifications but CVN data cannot be quantitatively used as a structural design parameter. Therefore, some correlation to convert existing CVN data into meaningful K_{IC} data, mindful of the many mechanical and microstructural parameters involved, is of importance. Some recent attempts have been made to establish the existence of a correlation between K_{IC} and CVN data. Barson and Rolfe[10] and Wells[11] have established relationships which are shown in Fig. 61, illustrating the data obtained in this investigation. Shown plotted is $\frac{K_{IC}^2}{E}$ in psi-inch as a function of CVN in inch-lbs and includes data of fine and coarse pearlite structures, martensitic and spheroidized carbide structures for all carbon steels tested at 70°F, -100°F and -320°F. The expression developed by Rolfe et al. is as follows

$$\frac{K_{IC}^2}{E} = 0.048\,(CVN)^{3/2} \qquad (21)$$

where E is the elastic modulus, K_{IC} is in psi-$in^{1/2}$ units and CVN is in inch-lb units. This correlation was established for low carbon steels of pearlitic and quenched and tempered structures and for a quenched and tempered nickel steel. As shown in the figure this correlation does not apply to the data obtained in this research. This accentuates the care that must be taken with respect to prior history and mechanical testing in converting existing CVN data to K_{IC} values. A better correlation is the one shown developed by Wells and described by the following.

$$\frac{K_c^2}{E} = 0.5 \frac{CVN}{A} \qquad (22)$$

where K_c is the plane stress intensity factor in psi-in$^{1/2}$, A is the area of the cross-section at the ligament in inches^2 and the other symbols and their units are as before. This expression was developed by considering the crack extension force, G_c, determined by measuring the crack opening displacement (C.O.D.) of a Charpy impact specimen. As G_c = (C.O.D.) σ_{YS} and $K_C^2 = EG_c$ the relationship shown in Eq. (22) was formed. It can be seen that the stress-intensity factor can be related to the impact value if, experimentally, the C.O.D. is related to the energy/unit area obtained from impact tests. The importance of this relationship is that the K_c value is correctly related to the incremental work done to fracture and related also to the proportion of crack travel. The differences between the Wells and Rolfe correlations are apparently due to some over riding microstructural effects on any relationship between K_{IC} and CVN. Until these factors are known, it is dubious as to how valid such correlations might be.

3. Microcharacteristics of Fracture

So far semi-empirical equations founded on measured data have been considered and developed as a fracture criterion. It will be discussed here how an extension of this criterion based on theoretical considerations can be developed and interpreted in terms of micromechanical behavior.

Hill's[45] slip line theory for blunt notches describe the plastic constraint factor by

$$pcf = [1 + \ell n(1 + \frac{R}{\rho})] \qquad (23)$$

where ρ is the notch radius and R is the plastic zone size. It is seen

that as the plastic zone increases, the plastic constraint increases. Further, there is a limiting value of R, shown by Tetelman and McEvily[25] beyond which the plastic constraint factor reaches a maximum. This can be expressed as follows

$$R_\beta = \rho\left[e^{pcf_{max}-1}-1\right] \qquad (24)$$

where R_β is the critical plastic zone radius at which pcf becomes a maximum. This equation has been found to apply for blunt notches and, apparently, for very sharp notches like cracks. Tetelman found that as ρ was decreased for finer machined notches, R/ρ increased from 1 to 3 or 4, where 3.8 is the value of R/ρ where pcf is a maximum. The maximum value for R/ρ was obtained at a value of $\rho = 0.002$ inches. However, the omission of the fact that ρ increases as the plastic zone increases during testing affects the above analysis for sharp cracks since blunting results in a continually changing crack tip radius.

Gerberich et al.[48] has carried this analysis further and suggested that this increase in the pcf with very sharp notches may be apparent. It was shown that pcf_{max} could not be obtained in very sharp cracks until some finite plastic flow had occurred over a critical region. This led to a fracture analysis in terms of this critical region in which microcracking occurred before unstable fracture. Since R and ρ are functions of K^2 it was shown that the value describing this microstructural region was taken as some multiple n, of the grain size d, and gave a fracture criterion given by,

$$\frac{K}{\sigma_{LYS}} = \pi \text{ pcf } \left[\left\{e^{\text{pcf}} - 1 - \right\} \left\{\frac{nd}{2}\right\}^{1/2}\right], \epsilon_c^* > \frac{\sigma_{LYS}}{E} \quad (25a)$$

and

$$\frac{K}{\sigma_{LYS}} \leq [\pi nd]^{1/2}; \quad \epsilon_c^* \leq \frac{\sigma_{LYS}}{E} \quad (25b)$$

where ϵ_c^* is the critical total strain. This equation in conjunction with Eq. (18) represents a dual cleavage fracture criterian with that given earlier by Eqs. (15), (16), (18) and (20). This criterion is concerned with the microstructural region where nonpropagating microcracks are formed, whereas, the other is concerned with the mechanical and structural effect attributed to cleavage. Equation (25) shows that if the number of grains in the length nd of the critical region described can be determined, then K_{IC} could be determined.

Tetelman, et al.[15] using the microcrack density observed from tensile samples[47] attempted to determine the probability of microcracking in the critical zone at the notch root and relate this to the fracture criterion. As an alternative, the microcrack density can be used in determining n in Eq. (25). This would necessitate the determination of the number of microcracks formed in the critical zone prior to fracture. The stress wave emission technique can be used in determining the microcrack density, (m.d.). Gerberich et al.[48] in considering the microcrack density zone as a cylinder of diameter, nd, across the speciment thickness, t, derived the following expression,

$$nd = \frac{4 N_{SWE}}{\pi t(md)}^{1/2} \quad (26)$$

where N_{SWE} is the number of stress waves emitted and md is the microcrack density.

This criterion was examined in this investigation to determine whether this theoretical approach provided as good a fracture criteria as that derived from semi-empirical considerations. Tables XVII-XIX summarize the calculated values of the microcrack densities, m.d., and effective length of the microcrack density zones, nd, determined from measured values of K_{IC}, σ_{LYS} and N_{SWE} from the data. Also included is the multiple n, associated with the grain size, d which determines the size of the critical zone. These tables summarize the calculated data for -320°F, -200°F and -100°F. Figure 62 shows the calculated values of nd, plotted as a function of the volume fraction of pearlite, V_{fp}. This plot shows the critical microcrack density zone to decrease in length rapidly as V_{fp} is increased. The effect of increased V_{fp} on nd is of little significance for 0.43 to 0.78% carbon steels. Figure 63 shows the plot of m.d., calculated from stress wave emission data as a function of the volume fraction of pearlite. This plot shows the increase in m.d., as V_{fp} is increased and illustrates also the temperature effect. The effect of decreasing the temperature serves to restrict the formation of large numbers of microcracks. However, the microcracks formed may cover a larger region as indicated in the fractographs of Figs. 46 and 51. These illustrate that cleavage occurs over larger areas at -320°F than at 70°F. This indicates that the microcrack density is smaller at low temperatures as those microcracks which form quickly propagate and induce cleavage fracture. Kaechele and Tetelman[15] using tensile tests estimated m.d. to be $11\times10^5/\text{inches}^3$. In comparison the calculated values for m.d. in this investigation range from $0.6\times10^5/\text{inches}^3$ to $48.7\times10^5/\text{inches}^3$ indicating this theoretical approach to be significant. As shown by both these plots, the pearlite colonies are very conducive to the formation of

microcracks due to the many potential sites available. It is interesting to note that while m.d. is increased with increasing V_{fp}, the critical microcrack density zone length decreases as was indicated in Fig. 62. This means that the pearlite colonies provide a predominant effect in the nucleation of critical microcracks. These may then lead to cleavage fracture at a stress intensity level somewhat lower than if no pearlite were present. It is of interest also that n is a function of grain size d, and the volume fractions of ferrite and pearlite. This is described in the following relationship derived from the data shown plotted in Fig. 62 for varying temperatures,

$$n\,d = f_{\alpha}\,[C_1\,d^{1/4}] + f_p\,C_2 \qquad (27)$$

where $C_1 = 0.182$ inches$^{3/4}$ and $C_2 = 0.014$ inches. Figure 64 shows the curve which utilizies actual grain size data for the calculation and illustrates that n is a function of the ferrite grain size, d.

Tables XVII - XIX indicate that 0.01 and 0.04 are the approximate upper and lower values for the microcrack density zone length, nd. Using these values as bounds, the stress intensity to lower yield strength can be calculated for plastic constraint factors ranging from 1 to the theoretical maximum of 2.57. These upper and lowerbounds are shown plotted on Fig. 65 . As the measured data are almost entirely included within these bounds, then this shows the theoretical interpretation gives about the same fit to the data as the semi-empirical approach.

A schematic drawing relating the important microcharacteristics discussed is shown in Fig. 66 . This model portrays the calculated values of md, nd, and d for 1000, 1019, 1043, 1056 and 1078 carbon steels fracture tested at -320 F. Shown are the microstructural regions for these steels

in which the parameters associated with cleavage fracture are indicated. This schematic also can be used in describing the physical significance of nd. Microcracking was found to occur in the ferrite grains for the 1000 and 1019 carbon steels. However, for the 1043, 1056 and 1078 carbon steels, as the pearlite content was increased, the probability of microcracks occurring in the pearlite was increased. This shows that the multiple n, of the length nd, reflects the number of grain size only in the 1000 and 1019 carbon steels. Further, this indicates that for increasing pearlite content, the multiple n must be described in terms of some other microstructural unit such as the prior austenitic grain size or the pearlitic colony size. As observed in the fractograph of Fig. 44 for 0.43% C steel at -320 F, it was found that cleavage occurred over approximately 13 lamellae. As observed in the photomicrograph of Fig. 15 for 0.56% C steel at -320°F, again cleavage occurred over approximately the same number of cementite lamellae. This indicates that cleavage does occur in small steps over a group of ferrite-cementite lamellae. In Figs. 44 and 15 it is observed that the microstructural unit appropriate to the high volume fraction pearlite steels might be some multiple of the pearlite colony size.

Finally, the data obtained and the resulting analyses show that the plastic constraint approach to a cleavage fracture criterion is reasonable in that the role of ferrite grain size and microcrack density on cleavage fracture has been demonstrated.

V. CONCLUSIONS

This investigation has resulted in the following primary conclusions:

1. Fracture criteria have been developed that empirically describe the lower yield stress and true fracture stress of plain carbon hypoeutectoid steels in the range -320°F to +150°F, provided the room temperature values are known.

2. The lower yield stress and true fracture stress were utilized in a criterion which numerically describes the plastic constraint factor, as deduced from crack extension experiments.

3. Use of the fracture criterion enables the prediction of plane strain fracture toughness values for this class of hypoeutectoid steels investigated.

4. A theoretical derivation of the plastic constraint factor was developed and interpreted in terms of the micromechanical behavior of carbon steels.

5. The microcrack density determined from fracture tests by using the stress wave emission technique for these steels ranged between $0.6 \times 10^5/\text{in.}^3$ and $48.7 \times 10^5/\text{in.}^3$, which is in agreement with Kaechele and Tetelman's result of $11 \times 10^5/\text{in.}^3$ obtained from tensile tests.

6. The agreement cited in five indicates that the stress wave emission technique is a sensitive and accurate method for determining crack growth characteristics.

7. The fracture toughness data obtained over the range of mechanical and metallurgical variables for these steels can be applied to structural design problems and made use of in structural specifications.

8. Charpy V-notch impact and plane strain fracture toughness correlations are not generally valid.

9. The formation of microcracks and the critical microcrack region preceding cleavage are related to the ferrite grain size when the carbon content is less than 0.2%C, and above this value they are related to the pearlite colony size.

10. The correlation between observed mechanical properties and information obtained from surface fractography and stress wave emissions enabled a complete study of the fracture processes to be made.

ACKNOWLEDGMENT

The author wishes to express his appreciation and deep gratitude to Professor Earl R. Parker for his continued guidance and encouragement during the present investigation and particularly during the course of his studies at the University of California. Without this, the successful completion of the author's studies could not have been realized.

Appreciation is also expressed to Mr. William W. Gerberich for his advice and support in this investigation and during the author's association with him at the Lawrence Radiation Laboratory. Thanks are due also to Dr. Yosef Katz for his help and support.

The author also wishes to express his gratitude to Professor Frank E. Hauser for his advice and guidance while graduate advisor to the author in the Department of Mechanical Engineering. Thanks are due to both Professors Frank E. Hauser and Iain Finnie for their review of this manuscript.

The assistance of the technical staff of the Inorganic Materials Research Division of the Lawrence Radiation Laboratory is recognized, particularly Gloria Pelatowski (preparation of line drawings), Lee Johnson (metallography), Phila Witherell (photography), Pat Shand (preparation of manuscript) and J. A. Patenaude and Duane Newhart (machining). The assistance of the Sterescan Scanning Electron Microscope operated by M. Nemanic of the Electronics Research Laboratory, University of California is acknowledged.

This work was done under the auspices of the U. S. Atomic Energy Commission through the Inorganic Materials Research Division of the Lawrence Radiation Laboratory.

REFERENCES

1. J. E. Srawley and W. F. Brown, Jr., Fracture Toughness Testing and Its Applications, (ASTM Special Technical Publ. No. 381, 1965), pp. 133-196.
2. J. E. Campbell, Report No. 207, Defense Materials Information Center, Battelle Memorial Institute, Ohio.
3. J. E. Srawley, Plane-Strain Fracture Toughness, in Fracture; An Advanced Treatise, Vol. IV (Engineering Fracture Design), H. Liebowitz, ed., (Academic Press, New York, 1969), p. 45.
4. E. T. Wessel, "State of the Art of the WOL Specimens for K_{IC} Fracture Toughness Testing," Eng. Fracture Mech., 1, 77-103 (1968).
5. A. R. Rosenfield and G. T. Hahn, "Numerical Description of the Ambient Low-Temperature and High Strain-Rate Flow and Fracture Behavior of Plain Carbon Steel," Trans. ASM, 59, 962 (1966).
6. G. T. Hahn and A. R. Rosenfield, "Experimental Determination of Plastic Constraint Ahead of a Sharp Crack Under Plane Strain Conditions," Trans. ASM., 59, 909 (1966).
7. B. L. Averbach, Some Physical Aspects of Fracture, in Fracture; An Advanced Treatise Vol. I (Microscopic and Macroscopic Fundamentals), H. Liebowitz, ed., (Academic Press, New York, 1965), p. 441.
8. A. S. Tetelman, T. R. Wilshaw and C. A. Rau, Jr., "The Critical Tensile Stress Criterion for Cleavage," Int. J. Fracture Mech., 4 (2), 147 (1968).
9. E. Smith, "Cleavage Fracture in Mild Steel," ibid, p. 131.
10. J. M. Barman and S. T. Rolfe, "Correlations Between K_{IC} and CVN Test Results in the Transition Temperature Range," U.S.S. Corporation report submitted to ASTM for publication, 1969.

11. A. A. Wells, "Fracture Control of Thick Steels for Pressure Vessels," Brit. Welding J., May 1968, p. 221.

12. W. W. Gerberich and C. E. Hartbower, "Some Observations on Stress Wave Emission as a Measure of Crack Growth," Int. J. Fracture Mech., 3, (3), 185-192 (1967).

13. C. E. Hartbower, W. W. Gerberich and P. P. Crimmings, "Monitoring Subcritical Crack Growth by Detection of Elastic Stress Waves," Welding J., Research Supplement, January, 1968.

14. C. E. Hartbower, W. W. Gerberich, and H. Liebowitz, "Investigation of Crack-Growth Stress-Wave Relationships," Eng. Fracture Mech., 1, 291-308 (1968).

15. L. E. Kaechele and A. S. Tetelman, "A Statistical Investigation of Microcrack Formation," Acta Met., 17, 463 (1969).

16. J. E. Srawley and B. Gross, "Stress Intensity Factors for Crackline Loaded Edge-Crack Specimens," NASA TND-3820, 1966.

17. J. A. Rinebolt, "Effect of Pearlite Spacing on Transition Temperature of Steel at Four Carbon Levels," Trans. ASM, 46 1527-1543(1954).

18. W. F. Brown, Jr. and J. E. Srawley, "Plane Strain Crack Toughness Testing of High Strength Metallic Materials," ASTM STP No. 410, 1967.

19. E. T. Wessel and R. D. Olleman, "Apparatus for Tension Testing at Subatmospheric Temperatures," ASTM Bulletin, TP10 June 1953.

20. E. E. Underwood, "Quantitative Metallography," Parts 1 and 2, Metals Engineering Quarterly, 1, Nov. 1961.

21. C. J. Smithells, Metals Reference Book, Vol. 1, Third Edition, (Butterworth and Company, Ltd., London, 1962).

22. M. Gensamer, E. B. Pearsall, W. S. Pellini and J. R. Low, Jr., "The Tensile Properties of Pearlite, Bainite and Spheroidite," Trans. ASM, 30, 983-1020 (1942).

23. B. R. Butcher and H. R. Pettit, "Tensile Deformation and Cracking of Plain High Carbon Steels Containing Pearlite," J. Iron and Steel Inst., 204, 469-477 (1966).

24. K. W. Burns and F. B. Pickering, "Deformation and Fracture of Ferrite-Pearlite Structures," J. Iron and Steel Inst., p. 899-906, Nov. 1964.

25. A. S. Tetelman and A. J. McEvily, Jr., Fracture of Structural Materials, (John Wiley and Sons, Inc., New York, 1967).

26. W. F. Brown, Jr. and J. E. Srawley, Plain Strain Crack Toughness Testing of High Strength Metallic Materials, ASTM Special Technical Publication No. 410, 1967.

27. G. T. Hahn and A. R. Rosenfield, "The Influence of a Fine Dispersion on the Cleavage Strength of Iron," Trans. AIME, 239, 668-674 (1967).

28. C. T. Liu and J. Gurland, "The Fracture Behavior of Spheroidized Carbon Steels," Trans. ASM, 61, 156-167 (1968).

29. C. T. Liu and J. Gurland, "The Strengthening Mechanism in Spheroidized Carbon Steels," Trans. AIME, 242, 1535-1542 (1968).

30. D. E. Hodgson and A. S. Tetelman, "The Effect of Microstructure on the Cleavage Strength of Quenched and Tempered Steels Fracture," Proceedings of the Second International Conference on Fracture, Brighton, England, April 1969; Paper 22 (Chapman and Hall, Ltd., London).

31. Unpublished data from W. W. Gerberich.

32. G. T. Hahn, B. C. Averbach, W. S. Owen, M. Cohen, "Initiation of Cleavage Microcracks in Polycrystalline Iron and Steel," in Fracture, B. L. Averbach, et al., eds., (M.I.T. Press, Cambridge, Mass, 1959).

33. R. M. Brick, R. B. Gordon and W. Phillips, Structure and Properties of Alloys, 3rd. Edition, (McGraw-Hill Book Company, New York, 1965), Chapter 9.

34. J. Plateau, G. Henry and J. Friedel, "Cleavage Crack Propagation," First International Conference on Fracture, Sendai, Japan, (1965).

35. H. C. Burghard, Jr. and N. S. Stoloff, "Cleavage Phenomena and Topographic Features," in Electron Fractography, (ASTM Special Technical Publication, No. 436, 1967).

36. J. Friedel, "Propagation of Cracks and Work Hardening," in Fracture, B. L. Averbach, et al., eds. (M.I.T. Press, Cambridge, Mass, 1959).

37. A. H. Cottrell, "Theory of Brittle Fracture in Steel and Similar Metals," Trans. AIME, 212, 192 (1958).

38. N. J. Petch, Phil. Mag., 3, 1089 (1958).

39. N. J. Petch, "The Ductile-Cleavage Transition in Alpha-Iron," in Fracture, B. L. Averbach, et al., eds., (M.I.T. Press, Cambridge, Mass., 1959).

40. E. O. Hall, "The Deformation and Aging of Mild Steel: III. Discussion of Results, Proc. Phys. Soc. (London), B 64, 747 (1951).

41. N. J. Petch, "The Cleavage Strength of Polycrystals," J. Iron and Steel Inst., p. 25, May 1953.

42. H. J. Kouwenhoven, "The Influence of Ferrite Grain Size and Volume Fraction of Pearlite on the Lower Yield Strength and Luders Strain of Carbon Steel," Trans. ASM, 62, (2), 437 (1969).

43. K. E. Puttick, "The Structure, Deformation and Fracture of Pearlite," Part I - Structure, J. Iron and Steel Inst., p. 161, Feb. 1957.

44. J. M. Bucher, J. D. Grozier and J. F. Enrietto, "Strength and Toughness of Hot-Rolled Ferrite-Pearlite Steels," in Fracture; An Advanced Treatise, Vol. VI (Fracture of Metals), H. Liebowitz, ed., (Academic Press, New York, 1969).

45. R. Hill, Mathematical Theory of Plasticity, (Clarendon Press, Oxford, England, 1950).

46. J. M. Krafft, "A Rate Spectrum of Strain Hardenability and of Fracture Toughness," Report of N.R.L. Progress, January 1966.

47. J. R. Low, Jr., "A Review of the Microstructural Aspects of Cleavage Fracture," in Fracture, B. L. Averbach, et al., eds. (John Wiley and Sons, Inc., New York, 1959), p. 68.

48. W. W. Gerberich, V. F. Zackay, E. R. Parker, and D. E. Porter, "The Role of Grain Boundaries on Crack Growth," Sixteenth Sagamore Army Materials Research Conference on Ultra Fine Grain Metals, August 1969.

Table I. Chemical composition of steels

Steel No.	%C	%Mn	%Si	%S	%P	%Cr	%Mo	%Ni	%V	%Cu
0	0.0025	0.02	< 0.02	0.010	0.014	-	-	-	-	-
2	0.19	0.86	0.05	0.023	0.006	0.07	<0.01	0.01	-	0.05
4	0.43	0.75	0.30	0.021	0.016	0.20	0.03	0.20	0.025	0.15
6	0.56	0.62	0.20	0.037	0.008	0.05	<0.01	0.015	-	0.02
8	0.78	0.76	0.22	0.021	0.014	0.12	0.015	0.015	-	0.07

Table II. Lineal analysis data for pearlitic and spheroidized carbide structures

Steel	Structure	Average ferrite grain diameter d, ins × 10^5	Volume fraction of pearlite V_{fp}	Average pearlite spacing s_p, ins × 10^5
1000	Treated for fine pearlite	410.	0	-
	Treated for coarse pearlite	337.	0	-
1019	Fine pearlite	67.	27	1.8
	Coarse pearlite	83.	19	2.5
	Spheroidized carbide	20.2		
1043	Fine pearlite	23.	67	2.2
	Coarse pearlite	31.	50	3.3
	Spheroidized carbide	5.4		
1056	Fine pearlite	25.	87	2.8
	Coarse pearlite	33.	82	3.6
	Spheroidized carbide	5.45		
1078	Fine pearlite	-	100	2.8
	Coarse pearlite	-	100	3.7
	Spheroidized carbide	4.95		

Table III. Tensile properties of 1078 carbon steel for varying structures and temperatures

Steel	Structure	Test temp. °F	Measured tensile properties				ϵ^* % elong.	% reduct. of area	ϵ_L Luders band strain	ϵ_f True fracture strain	Corrected tensile props. for grain size effect (ksi)	
			σ_{UYS} ksi	σ_{LYS} ksi	σ_{ULT} ksi	σ_f^* ksi					σ_{LYS}	σ_f^*
1078	Fine pearlite	RT		65.8†	131	162	17	24	0.25	0.274	65.8	162
				70.0†	133	167.5	12	25	0.15	0.31	70	167.5
		-100	90.4	85.7	153.1	187.5	15.8	22.5	4.25	0.254	85.7	187.5
		-320		167.5††		167.5		0.08		0.01	167.5	167.5
	Coarse pearlite	RT		53.6†	121	143	18	19	0.187	0.2085	53.6	143
		-100	76.6	74.5	141.7	166	16	17	4.0	0.183	74.5	166
		-320		151††		151	-	-	-	0	151	151
	Martensite	RT				20.4†††				0		
		-320				46†††	-	-	-	0		
	Spheroidized carbide	RT	83.6	77	98	152	25	45	2.075	0.595		
		-320		157.2††		160	-	2.02	-	0.0198		

† 0.2% offset used for yield stress

†† yield synonomous with cleavage

††† failed prematurely

Table IV. Tensile properties for 1056 carbon steel for varying structures and temperatures

Steel	Structure	Test temp. °F	Measured tensile properties σ_{UYS} ksi	σ_{LYS} ksi	σ_{ULT} ksi	σ_f^* ksi	ϵ^* % elong.	% reduct. of area	ϵ_L Luders band strain	ϵ_f True fracture strain	Corrected tensile props. for grain size effect (ksi) σ_{LYS}	σ_f^*
1056	Fine pearlite	RT	50	50	103	149	23	37.5	0.45	0.47	51.56	193
			53	51	106.8	143	19	29	0.25	0.432	52.56	185.5
		-100	77.5	73.5	130	172	23.9	30	0.6	0.365	75.06	215.8
		-320		136.2 †		136.2	-	-	-	0	137.76	171.8
	Coarse pearlite	RT	50	49	102.5	141	25	33	0.55	0.395	50.76	177.5
			46.5	46	99.5	121.8	19	20.4	0.5	0.247	47.76	156.7
		-100	78.3	69.4	121	160	26	28.6	1.0	0.336	71.16	196.8
		-320		122 †		122	-	-	-	0	123.76	151.2
				143 †		143	-	-	-	0	144.76	172.2
	Martensite	RT				26.6††	-	-	-	0		
		-320				42.9††	-	-	-	0		
	Spheroidized carbide	RT	64.4	64.4	83.6	145.5	28.5	55	2.15	0.8		
		-320	173	159	166	187	11.9	11.8	3	0.53		

† Yield synonomous with cleavage

†† Failed prematurely

Table V. Tensile properties for 1043 carbon steel for varying structures and temperatures

Steel	Structure	Test temp. °F	Measured tensile properties				ϵ^* % elong.	% reduct. of area	ϵ_L Luders band strain	ϵ_f True fracture strain	Corrected tensile props. for grain size effect (ksi)	
			σ_{UYS} ksi	σ_{LYS} ksi	σ_{ULT} ksi	σ_f^* ksi					σ_{LYS}	σ_f^*
1043	Fine pearlite	RT	69.2	68.1	103.2	166	23	47.3	1.25	0.6366	63.15	112.3
			70.4	78.8	107.0	166	21	44	1.375	0.578	73.95	113.2
			73.5	65.8	104	159	23	41.3	1.15	0.534	60.95	105.3
		-100	96	82.6	122.5	194	30.5	49	1.625	0.673	77.75	138.5
		-320		162.4 †		162.4	-	-	-	0	157.55	118.7
				167.5 †		167.5	-	-	-	0	162.65	123.8
	Coarse pearlite	RT	72.5	65.4	101	159	23.4	42.9	1.1	0.56	59.45	115.4
			70.4	69.6	108	155	22	37	0.75	0.456	63.95	111.7
		-100	89.2	79.5	119.5	178.5	26.3	42.8	1.625	0.56	73.55	133.9
		-320	157.2	150	165	196	17	16.3	2.25	0.178	144.05	154.5
	Martensite	RT				67.1 ††				0		
		-320				126 ††				0		
	Spheroidized carbide	RT	75	74.3	90.4	204	30.2	71.5	1.7	1.25		
		-320	152.7	147	153.1	225	24.5	36.8	6.85	0.457		

† yield synonomous with cleavage

†† failed prematurely

Table VI. Tensile-properties for 1019 carbon steel for varying structures and temperatures

Steel	Structure	Test temp. °F	Measured tensile properties σ_{UYS} ksi	σ_{LYS} ksi	σ_{ULT} ksi	σ_f^* ksi	ϵ^* % elong.	% reduct. of area	ϵ_L Luders band strain	ϵ_f True fracture strain	Corrected tensile props. for grain size effect (ksi) σ_{LYS}	σ_f^*
1019	Fine pearlite	RT		38.15†	69.5	152	39	70.5	< 1	1.153	47.35	204.3
		RT	38.3	38.3	68	135	40	68	1.7	1.12	47.5	187.6
		-100	56.5	56.5	79.6	178	45.6	67.4	3.56	1.12	65.7	232.9
		-320	125.	122.4	128.7	146.5	13	12.3	5.5	0.131	131.6	188.5
	Coarse pearlite	RT	46.	41.3	64.	127	42	60.1	2.75	0.92	49.8	171.4
		RT	43.6	39.8	62.5	126	43	61.6	3	0.96	48.3	170.4
		-100	72	58.2	78	123.4	35.2	42.8	3.1	0.56	66.7	165.7
		-320	133.5	120.5	125.6	140	13.4	10.2	7.5	0.109	129.	175.5
		-320	135	128	129	136	7	5	4.2	0.05	136.5	169.5
	Martensite	RT		167.4†	203	316	11	47	-	0.634		
		-320		202†	216	221	0.4	2.08	-	0.0198		
	Spheroidized Carbide	RT	47	47	65.4	200	42.2	81.6	1.9	1.695		
		-320	140	127.7	128.6	163.3	20	22.5	6.9	0.278		

† 0.2% offset was used for yield stress

Table VII. Tensile properties for 1000 decarburized steel for varying structures and temperatures.

Steel	Structure	Test Temp. °F	Measured tensile properties				ϵ^* % elong.	% reduct. of area	ϵ_L Luders band strain	ε_f True fracture strain	Corrected tensile props. for grain size effect (ksi)	
			σ_{UYS} ksi	σ_{LYS} ksi	σ_{ULT} ksi	σ_f^* ksi					σ_{LYS}	σ_f^*
10002	Heat treated as for fine pearlite	RT	22.4	22.4	43.8	141	54.4	84.3	1.3	1.84	51.6	305
		-100	40.7	34.7	52.0	173	90.0	72.5	4.02	1.33	63.9	374.5
		-320	77.5	75.6	80.6	82.3	0.25	2.02	-	0.0198	104.8	188.8
	Heat treated as for coarse pearlite	RT	30	24	44	316	32	86.6	-	2.02	53	426
		-100	35.7	34.7	52.0	138	94.3	71.5	3.75	1.25	58.7	300
		-320	79.6	75.6	90	92	0.75	2.02	-	0.0198	102.6	176

Table VIII. Charpy V-notch impact data and $\left(\frac{K_{IC}^2}{E}\right)_{meas.}$ data for varying structures and temperatures.

Steel	Structure	CVN (ft-lbs)			$(K_{IC}^2/E)_{meas.}$ psi-in		
		-320°F	-100°F	+70°F	-320°F	-100°F	+70°F
1000	Treated for fine pearlite	—	—	—	28	—	—
	Treated for coarse pearlite	—	—	—	27.4	—	537.6
1019	Fine pearlite	1.75	2.5	> 119	48 64.5	168 140.8	202.8 252.3
	Coarse pearlite	1.75	2.0	> 120	70.5	158.7	208.0 353.6
	Martensite	2.5	—	24.5	—	—	—
	Spheroidized carbide	2.0	—	> 120	52	—	—
1043	Fine pearlite	2.0	6.5	23	56.2 50.8 45.6	163.3 132.3	580.8 278.0
	Coarse pearlite	1.5	5.55	21	26.1 26.1	136.5 108.3	360.5
	Martensite	0.5	—	2.5	—	—	—
	Spheroidized carbide	1.0	—	93	106.5	—	—
1056	Fine pearlite	1.0	2.5	10	53.3 49	166.3 122	218.7 154.1
	Coarse pearlite	1.0	1.75	10.5	45.6	108.3	224.1
	Martensite	0.5	—	0.75	—	—	—
	Spheroidized carbide	1.5	—	72	213.3	—	430
1078	Fine pearlite	1.5		5	35.2 33.3 33.5	108.3 97.2	143.3 148.0 143.3
	Coarse pearlite	1.0		8.5	40	72.3	151.6 142.3
	Martensite	0.5	—	0.5	—	—	—
	Spheroidized carbide	0.75	—	23.5	60.3	—	770

Table IX. Measured plane-strain fracture toughness values of pearlitic structures at varying temperatures

Steel	Structure	K_{IC}, ksi-(in)$^{1/2}$					
		-320°F	-200°F	-100°F	+70°F	100°F	150°F
1000	Treated for fine pearlite	29	—	—	**	—	—
	Treated for coarse pearlite	287	—	—	127		
1019	Fine pearlite	38 44	51	72 65	78 87	82.5	100
	Coarse pearlite	46	54 57	69	79 103		110
1043	Fine pearlite	41 39 37	59	70 63	132 94.6	130 101.2	94
	Coarse pearlite	28.0 28.0	48.0	64 57	104		150
1056	Fine pearlite	40 38.4	58*	70.6 60.5	81 68	65	95.7
	Coarse pearlite	37	48.5 44	57*	82*		94.5
1078	Fine pearlite	32.5 31.7 31.6	49	57 54	65.6 65.5 66.6	61	94
	Coarse pearlite	35	45	46.6	67.5 65.4		77

* Interpolated values taken from curves.

** Specimen failed by gross tearing

Table X. Measured fracture properties of spheroidized carbide and martensitic structures at -320°F and +70°F

Steel	Structure	K_{IC}, ksi-$in^{1/2}$		(K_{IC}/σ_{LYS}) $in^{1/2}$		Plastic constraint factor p.c.f. $= (\sigma_{f\ meas}^{*}/\sigma_{LYS\ meas.})$
		-320°F	+70°F	-320°F	+70°F	-320°F
1019	Spheroidized carbide	39.5	-	0.310	-	1.28
	Martensite	50.0	112.0	0.248	0.670	-
1043	Spheroidized carbide	56.5	-	0.384	-	1.53
	Martensite	28.5	46.5	-	-	-
1056	Spheroidized carbide	80.0	114.0	0.501	-	1.17
	Martensite	-	-	-	-	-
1078	Spheroidized carbide	42.5	152.0	0.270	1.98	1.02
	Martensite	21.0	28.5	-	-	-

Table XI. $\left(\frac{K_{IC\ meas}}{\sigma_{LYS\ meas}}\right)$ and plastic constraint factor (p.c.f.) values of pearlitic structures at varying temperatures

Steel	Structure	$\left(\frac{K_{IC\ meas}}{\sigma_{LY\ meas}}\right)$, $in^{1/2}$				Plastic Constraint Factor pcf = $(\sigma^*_{f\ meas}/\sigma_{LYS\ meas})$			
		-320°F	-200°F†	-100°F	+70°F	-320°F	-200°F	-100°F	+70°F
1000	Treated for fine pearlite	0.384	-	-	-	1.09	2.3	-	-
	Treated for coarse pearlite	0.380	-	-	5.3	1.16	-	-	-
1019	Fine pearlite	0.31 0.36	.68	1.275 1.15	2.04 2.04 2.26 2.27	1.18	2.04	2.57	
	Coarse pearlite	0.386 0.363	.74 .78	1.18	1.92 1.99 2.5 2.59	1.16 1.16	1.85	2.12	
1043	Fine pearlite	0.252 0.245 0.24 0.232 0.228 0.221	.546	0.846 0.764	1.97 1.70 2.04 1.39 1.20 1.44	1.0 1.0	1.52	2.35	2.44 2.11 2.41
	Coarse pearlite	0.817 0.187	.48	0.805 0.717	1.59 1.50	1.31	1.72	2.24	2.43 2.22

Table XI. (Continued)

Steel	Structure	$\left(\frac{K_{IC\ meas}}{\sigma_{LY\ meas}}\right)$, $in^{1/2}$				Plastic constraint factor pcf = $(\sigma^{*}_{f\ meas}/\sigma_{LYS\ meas})$			
		-320°F	-200°F †	-100°F	+70°F	-320°F	-200°F	-100°F	+70°F
1056	Fine pearlite	0.294	.624	0.96	1.62	1.0	1.61	2.34	
		0.282		0.82	1.59				
					1.36				
					1.34				
	Coarse pearlite	0.304	.54	0.82	1.668	1.0	1.91	2.30	
		0.259	.48		1.775	1.0			
1078	Fine pearlite	0.194	.475	0.665	1.0	1.0	1.65	2.19	2.46
					1.0				
		0.19		0.63					
		0.189		0.94					2.39
				0.95					
	Coarse pearlite	0.232	.48	0.625	1.26	1.0	1.65	1.79	
					1.22				

† values for σ_{LYS} were interpolated from σ_{LYS} vs temperature curves

Table XII. Calculated values of plane strain fracture toughness values using derived semi-empirical equations for σ_{LYS} and σ_f^*, and pcf = 2.8 $(K_{IC}/\sigma_{LY})^{1/2}$-0.4 at varying temperatures.

Steel	Structure	$\sigma_{LY_{calc}}$, ksi			$\sigma_{f^*_{calc}}$, ksi			K_{IC}, ksi-in 1/2		
		-320°F	-100°F	+70°F	-320°F	-100°F	+70°F	-320°F	-100°F	+70°F
1000	treated for FP	105	67	45	274	274	274	121	172	243
	treated for CP	100	62	40	214	214	214	82	117	169
1019	fine pearlite	113	84.1	58.3	231.6	231.6	231.6	86	103	140
	coarse pearlite	117.4	75.1	50.5	215.6	215.6	215.6	74	102	136
1043	fine pearlite	140	94.8	65	185.5	185.5	185.5	53	67	88
	coarse pearlite	131	82.7	54.4	172	172	172	48	64.5	88
1056	fine pearlite	154.5	100.4	67.4	173	173	173	45	58	75.5
	coarse pearlite	129	79.3	58	152.2	152.2	152.2	41	54.5	70
1078	fine pearlite	163.7	104.7	69.2	165	165	165	39	54	68.5
	coarse pearlite	154.7	95.2	60.5	140	140	140	33	43	60

Table XIII. Calculated values of plane strain fracture toughness using derived semi-empirical equations for σ_{LYS} and σ_f^*, and pcf = 2.8 $(K_{IC}/\sigma_{LYS})^{1/2}$-0.4

Ferrite grain diameter $d^{1/2}$, $in^{1/2}$	Percentage pearlite structure	$\sigma_{LY_{calc}}$, ksi	$\sigma_{f(calc)}^*$, ksi	$\frac{\sigma_f^*}{\sigma_{LY}}$ Calc	$K_{IC_{calc}}$ ksi-$in^{1/2}$
16 $in^{-1/2}$	0	76.0	78.0	1.025	19.8
	0.25	96.7	99.0	1.02	25.5
36.7 $in^{-1/2}$	0	93.0	139.5	1.5	42.8
	0.25	110.0	146.5	1.32	42.0
50 $in^{1/2}$	0	103.9	179.0	1.725	59.8
	0.25	118.2	177.0	1.5	55.0

Note: The average pearlite spacing of $(S_p)^{-1/2}$ = 213 for 1019 steel was used

Table XIV. Stress wave emission analysis at -320°F

Steel	Structure	Time secs	N_{SWE}	Total resistivity, (g) 0 to max	Amplitude range, (g) 0 to peak	Average amplitude, (g) 0 to peak
1000	Heat treated as fine pearlite	16	228	0.2*	0.0013 to > 0.0065	-
1000	Heat treated as coarse pearlite	21	322	0.2	0.0013 to > 0.0065	-
1019	Fine pearlite	198	191	0.5	0.002 to 0.05	0.016
1019	Coarse pearlite	28	104	0.2	0.0013 to > 0.0065	-
1019	Spheroidized carbide	25	148	0.5	0.008 to 0.056	0.024
1043	Fine pearlite	12.2	152	0.5	0.008 to 0.064	0.020
1043	Coarse pearlite	10.3	50	0.2	0.003 to > 0.013	-
1043	Spheroidized carbide	25.5	134	0.5	0.008 to 0.056	0.014
1043	Martensite	12	147	0.2	0.0013 to 0.0104	-
1056	Fine pearlite	22.5	196	0.5	0.008 to 0.048	0.013
1056	Coarse pearlite	20.5	49	0.2	0.0013 to > 0.01	-
1078	Fine pearlite	20	188	0.5	0.0081 to 0.0645	0.017
1078	Coarse pearlite	21	227	0.2	0.0013 to 0.0078	-
1078	Spheroidized carbide	20	278	0.5	0.0081 to 0.0567	0.016
1078	Martensite	15	119	0.5	0.0081 to 0.0567	0.020

* average amplitude is indeterminate as the stress waves saturated at the sensitivities recorded above 0.4g.

Table XV. Stress wave emission analysis at -200°F

Steel	Structure	Time secs	N_{SWE}	Total sensitivity, (g), 0 to max	Amplitude range, (g) 0 to peak	Average amplitude, (g) 0 to peak
1019	Coarse pearlite	24	272	0.1*	0.00032 to > 0.0016	-
1043	Coarse pearlite	20	120	0.1	0.00032 to > 0.0016	-
1056	Coarse pearlite	23	117	0.1	0.00032 to > 0.001	-
1078	Coarse pearlite	18	101	0.2	0.0013 to > 0.0078	-

* Average amplitudes were indeterminate as the stress waves saturated at the sensitivities recorded above 0.4g.

Table XVI. Stress wave emission analysis at -100°F

Steel	Structure	Time secs	N_{SWE}	Total sensitivity, (g) 0 to max	Amplitude range, (g) 0 to peak	Average amplitude, (g) 0 to peak
1019	Fine pearlite	28	143	0.4	0.0026 to 0.005	0.0028
1043	Fine pearlite	22.5	182	0.4	0.005 to 0.03	0.007
1043	Coarse pearlite	14	151	0.05*	0.00081 to > 0.0032	-
1078	Fine pearlite	32	261	0.4	0.005 to 0.031	0.007

* Average amplitude is indeterminate as the stress waves saturated at the sensitivities recorded above 0.4g.

Table XVII. Summary of calculated values of microcrack densities, m.d., and the effective lengths of the microcrack density zones, nd at -320°F.

Steel	Structure	N_{SWE}	$\left(\frac{K_{IC}}{\sigma_{LYS}}\right)$, $in^{1/2}$	Plastic constraint factor (p.c.f.)	Microcrack density (m.d.) $\times 10^{-5}$	Effective length of microcrack density zone (nd) in	Ferrite grain size d, in
1000	Treated for fine pearlite	228	0.384	1.09	1.38	0.046	0.00410
1000	Treated for coarse pearlite	322	0.38	1.16	1.94	0.046	0.00337
1019	Fine pearlite	191	0.33	1.18	2.02	0.035	0.00067
	Coarse pearlite	104	0.38	1.16	0.63	0.046	0.00083
1043	Fine pearlite	152	0.24	1.0	6.18	0.0183	0.00023
	Coarse pearlite	50	0.19	1.31	4.85	0.0115	0.00031
1056	Fine pearlite	168	0.28	1.0	4.0	0.0252	0.00025
	Coarse pearlite	49	0.27	1.0	-	0.0232	0.00033
1078	Fine pearlite	188	0.19	1.0	18.2	0.0115	-
	Coarse pearlite	227	0.23	1.0	10.2	0.0169	-

Table XVIII. Summary of calculated values of microcrack densities, m.d., and the effective lengths of the microcrack density zones, nd, at -200°F.

Steel	Structure	N_{SWE}	$\left(\frac{K_{IC}}{\sigma_{LYS}}\right)$, $in^{1/2}$	Plastic constraint factor (p.c.f.)	Microcrack density (m.d.)$\times 10^5$	Effective length of microcrack density zone (nd) in	Ferrite grain size d, in
1019	Treated for coarse pearlite	272	0.76	1.85	5.35	0.0255	0.00083
1043	Treated for coarse pearlite	120	0.48	1.72	6.8	0.0148	0.00031
1056	Treated for coarse pearlite	228	0.50	1.91	17.0 30.0	0.0095	0.00033
1078	Treated for coarse pearlite	101	0.48	1.65	-	-	

Table XIX. Summary of calculated values of microcrack densities, m.d., and the effective lengths of the microcrack density zones, nd, at -100°F.

Steel	Structure	N_{SWE}	$\left(\frac{K_{IC}}{\sigma_{LYS}}\right)$, $in^{1/2}$	Plastic constraint factor (p.c.f.)	Microcrack density (m.d.)$\times 10^{-5}$	Effective length of microcrack density zone (nd) in.	Ferrite grain size d, in.
1019	Treated for fine pearlite	143	1.22	2.57	12.2	0.0121	0.00067
	Treated for coarse pearlite	-	-	2.12	-	0.0305	0.00083
1043	Fine pearlite	182	0.80	2.35	34.4	0.0083	0.00023
	Coarse pearlite	151	0.75	2.24	22.6	0.0089	0.00031
1078	Fine pearlite	261	-	2.19	-	0.0074	-
	Coarse pearlite	-	-	1.79	48.7	0.0205	-

FIGURE CAPTIONS

Fig. 1 Tensile specimen used in the determination of tensile properties.

Fig. 2 Fracture specimen design of the two pin-wedge opening load type.

Fig. 3 Fine pearlite structure of (a) 0.19% C, (b) 0.43% C, (c) 0.56% C and (d) 0.78% C steels as revealed by the optical microscope at room temperature.

Fig. 4 Coarse pearlite structure of (a) 0.19% C, (b) 0.43% C, (c) 0.56% C, and (d) 0.78% C steels at room temperature.

Fig. 5 Martensite structure of (a) 0.19% C and (b) 0.78% C steels at room temperature.

Fig. 6 Spheroidized carbide structure of (a) 0.19% C, (b) 0.43% C, (c) 0.56% C, and (d) 0.78% C steels at -320°F.

Fig. 7 Experimental arrangement illustrating the positioning of the crack opening displacement gauge and accelerometer.

Fig. 8 Calibration curve derived from boundary collocation procedures used in the determination of K_{IC}.

Fig. 9 High temperature experimental arrangement.

Fig. 10 Low temperature experimental arrangement.

Fig. 11 Fracture specimen showing the correct method of mounting the crack opening displacement gauge.

Fig. 12 Schematic of stress wave emission circuitry.

Fig. 13 Equipment arrangement of stress wave emission circuitry and universal testing machine including complete instrumentation.

Fig. 14 Fine pearlite structure of (a) 0.19% C and (b) 0.78% C steel as revealed by the optical microscope at -320°F.

Fig. 15 Coarse pearlite structure of (a) 0.19% C, (b) 0.43% C, (c) 0.56% C and (d) 0.78% C at -320°F.

Fig. 16 Decarburized carbon steel, 1000, treated for (a) coarse pearlite structure at 70°F, (b) fine pearlite structure at 70°F, (c) coarse pearlite structure at -320°F and (d) fine pearlite structure at -100°F.

Fig. 17 Measured lower yield strength shown as a function of volume fraction of pearlite for fine and coarse pearlite structures at varying temperatures.

Fig. 18 Measured true fracture stress shown as a function of volume fraction of pearlite for fine and coarse pearlite structures at -320°F.

Fig. 19 Measured lower yield stress shown as a function of the carbon content for the spheroidized carbide structures at -320°F.

Fig. 20 Measured plane-strain fracture toughness shown plotted as a function of the volume fraction of pearlite for fine and coarse pearlite structures at varying temperatures.

Fig. 21 Measured plane-strain fracture toughness shown plotted as a function of temperature for fine and coarse pearlite and martensitic structures of 1019 carbon steel.

Fig. 22 Measured plane-strain fracture toughness shown plotted as a function of temperature for fine and coarse pearlite and martensitic structures of 1043 carbon steel.

Fig. 23 Measured plane-strain fracture toughness shown plotted as a function of temperature for fine and coarse pearlite and spheroidized carbide structures of 1056 carbon steel.

Fig. 24 Measured plane-strain fracture toughness shown plotted as a function of temperature for fine and coarse pearlite, martensite and spheroidized carbide structures of 1078 carbon steel.

Fig. 25 Fracture surfaces of fine pearlite structures for (a) shown from the left: 0.19% C, 0.43% C, 0.56% C and 0.78% C steels fractured at 100°F; (b) 0.19% C, 0.43% C, 0.56% C and 0.78% C steels fractured at 70°F; and (c) 0.19% C, 0.43% C, 0.56% C and 0.78% C steels fractured at -320°F.

Fig. 26 Fracture surfaces of coarse pearlite structure for (a) shown from the left: 0.19% C, 0.43% C, 0.56% C, and 0.78% C steels fractured at 150°F; (b) 0.19% C, 0.43% C, 0.56% C, and 0.78% C steels fractured at 70°F; (c) 0.19% C, 0.43% C, 0.56% C and 0.78% C steels fractured at -320°F.

Fig. 27 Load-displacement curves for the coarse pearlite structures of (a) 0.19% C and (b) 0.78% C steels at 70°F.

Fig. 28 Load-displacement curves for the coarse pearlite structures of (a) 0.19% C and (b) 0.78% C steels at -100°F.

Fig. 29 Load-displacement curves for the coarse pearlite structures of (a) 0.19% C and (b) 0.78% C steels at -320°F.

Fig. 30 Load-displacement curves (a) for the martensitic structure of 0.78% C steel fractured at 70°F and (b) the spheroidized carbide structure fractured at 70°F.

Fig. 31 Ratio of measured plane strain fracture toughness to lower yield strength shown as a function of volume fraction of pearlite at varying temperatures.

Fig. 32 Fracture surfaces of martensite structures for (a) shown from the left: 0.19% C, 0.43% C, and 0.78% C steels fractured at 70°F; (b) 0.19% C, 0.43% C and 0.78% C steels fractured at -320°F.

Fig. 33 Fracture surfaces of spheroidized carbide structures for (a) shown from the left: 0.19% C, 0.43% C, 0.56% C and 0.78% C steels fractured at 70°F; (b) 0.19% C, 0.43% C, 0.56% C and 0.78% C steels fractured at -320°F.

Fig. 34 Measured plane strain fracture toughness and true fracture stress for the spheroidized carbide structure shown plotted as a function of carbon content at -320°F.

Fig. 35 Oscillogram of stress waves recorded for the 1000 C steel heat treated for coarse pearlite structure and fracture tested at -320°F. The time lines are 1 sec apart. Measured data for this emission record are given in Table XIV.

Fig. 36 Oscillogram of stress waves recorded for the 1019 C steel heat treated for coarse pearlite structure and fracture tested at -320°F. The time lines are 1 sec apart. Measured data for this emission record are given in Table XIV. This corresponds to the load-displacement curve of Fig. 29.

Fig. 37 Oscillogram of stress waves recorded for the 1043 C steel heat treated for coarse pearlite structure and fracture tested at -320°F. The time lines are 1 sec apart. Measured data for this emission record are given in Table XIV.

Fig. 38 Oscillogram of stress waves recorded for the 1078 C steel heat treated for coarse pearlite structure and fracture tested at -320°F. The time lines are 1 sec apart. Measured data for this emission record are given in Table XIV. This corresponds to the load-displacement curve of Fig. 29.

Fig. 39 Oscillogram of stress waves recorded for the 1043 C steel, heat treated for martensitic structure and fracture tested at -320°F. The time lines are 1 sec apart. Measured data for this emission record is given in Table XIV.

Fig. 40 Oscillogram of stress waves recorded for the 1078 C steel, heat treated for martensitic structure and fracture tested at -320°F. The time lines are 1 sec apart. Measured data for this emission record is given in Table XIV.

Fig. 41 Oscillogram of stress waves recorded for the 1019 C steel, heat treated for spheroidized carbide structure and fracture tested at -320°F. The time lines are 1 sec apart. Measured data for this emission record is given in Table XIV.

Fig. 42 Oscillogram of stress waves recorded for the 1078 C steel, heat treated for spheroidized carbide structure and fracture tested at -320°F. The time lines are 1 sec apart. Measured data for this emission record are given in Table XIV.

Fig. 43 Scanning electron micrographs showing typical cleavage in the ferrite and pearlite at -320°F for 1019 C fine pearlite (a) and (b), and for 1019 C coarse pearlite (c) and (d). Cleavage tongues are evident in (b) and the cleavage fatigue interface region is shown in (c).

Fig. 44 Fractographs of 1043 C steel, fine pearlite structure tested at -320°F showing typical cleavage in the pearlite colonies.

Fig. 45 Fractographs of 1056C steel, fine pearlite structure tested at -320°F showing secondary cracking and cleavage in pearlite.

Fig. 46 Fractographs of 1078 C steel tested at -320°F, showing for the fine pearlite structure, the linking of the pearlite colonies (a), (b) and (d). The cleavage fatigue interface region for the coarse pearlite structure is shown in (c).

Fig. 47 Fractographs of 1019 C steel, fine pearlite structure, tested at 70°F. Cleavage river patterns are shown in (a) and (b) while cleavage in ferrite is shown in (c). The slow crack region is shown in (d).

Fig. 48 Fractographs of 1043 C steel, fine pearlite structure, fracture tested at -100°F. Coalescence of river patterns in ferrite is shown in (a) and (b). Cleavage in pearlite is shown in (c).

Fig. 49 Fractographs of 1019 C steel, fine pearlite structure tested at -100°F showing microcracking in (a) and (b), and 1043 C steel, fine pearlite structure tested at 70°F, showing dimple rupture of both ferrite and pearlite (c) and (d).

Fig. 50 Fractographs of 1056 C steel, fine pearlite structure, tested at 70°F showing in (a), (b) and (c) cleavage in the pearlite colonies. Part (d) shows the same steel tested at -200°F and the cleavage fatigue interface region.

Fig. 51 Fractograph of 1078 C steel, fine pearlite structures in fracture toughness specimen tested at 70°F shown in (a) and (b) and coarse pearlite structure tested at 70°F shown in (c). Cleavage in pearlite is shown. Part (d) shows cleavage in pearlite in tensile specimen.

Fig. 52 Fractographs of 1056 C steel, fine pearlite structure, tested at 100°F, showing patterns of continually changing cleavage in pearlite.

Fig. 53 Fractographs of 1078 C steel, fine pearlite structure, tested at 100°F showing cleavage steps in (a) and (b) and the many orientations of cleaved pearlite colonies in (c).

Fig. 54 Variation of the square of the step height, h, as a function of the distance, ℓ, along the river.

Fig. 55 Corrected lower yield strength shown plotted as a function of the volume fraction of pearlite for fine and coarse pearlite structures at varying temperatures.

Fig. 56 Corrected true fracture stress shown plotted as a function of volume fraction of pearlite for fine and coarse pearlite structures at -320°F.

Fig. 57 Plastic constraint factor, p.c.f, shown plotted as a function of the stress intensity to lower yield stress ratio.

Fig. 58 Calculated plane-strain fracture toughness derived from the plastic constraint factor shown plotted as a function of the volume fraction of pearlite for fine and coarse pearlite structures at varying temperatures.

Fig. 59 Calculated plane strain fracture toughness shown plotted as a function of the interlamellar pearlite spacing.

Fig. 60 Calculated plane strain fracture toughness shown plotted as a function of the ferrite grain size for 0% and 23% pearlite structures at -320°F. Solid lines from Eq. 20. Points are actual experimental data.

Fig. 61 Variation in $\frac{K_{IC}}{E}^2$ is shown as a function of energy absorbed in Charpy V-notch impact tests.

Fig. 62 Variation in the effective length of the microcrack density zone, nd, shown as a function of the volume fraction of pearlite for fine and coarse pearlite structures at varying temperatures.

Fig. 63 Variation in the microcrack density, m.d., shown as a function of the volume fraction of pearlite at varying temperatures.

Fig. 64 Variation in the number of microstructural units in the effective zone length, n, shown as a function of the ferrite grain size, d. The letter n denotes a microstructural unit which is a multiple of the ferrite grain size, d, in the effective zone length, nd.

Fig. 65 Plastic constraint factor, p.c.f., shown plotted as a function of the stress intensity to lower yield stress ratio indicating the upper and lower bounds for nd = 0.01 and 0.04 respectively.

Fig. 66 A schematic modelling the relative calculated values of microcrack density, m.d., and effective length of the microcrack density zone, for all carbon steels of fine pearlite structures tested at -320°F.

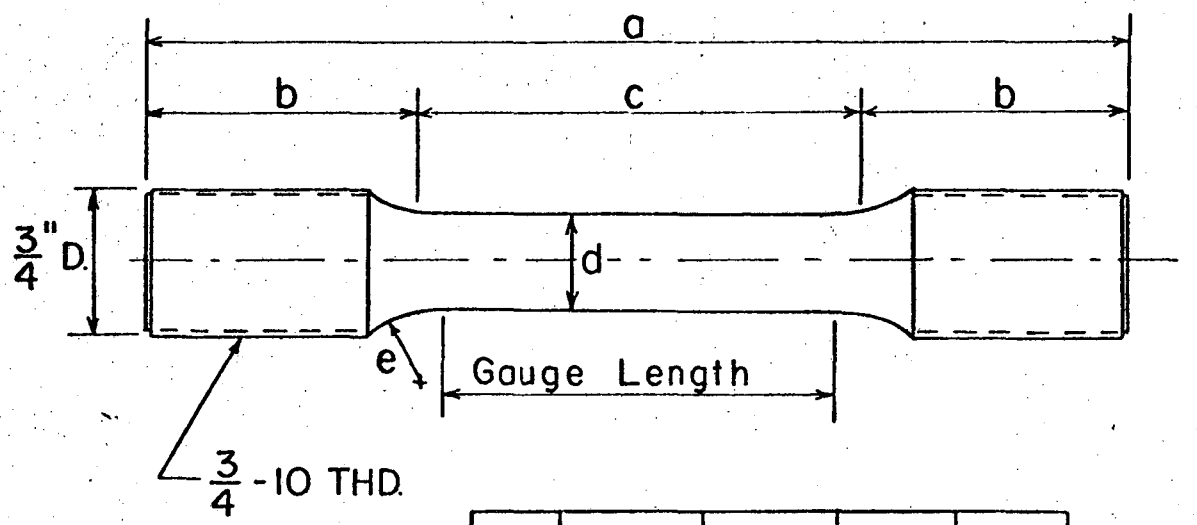

	a	b approx.	c	d	e
2" Gauge Length	5"	1 3/8"	2 1/4"	1/2"	3/8"
1" Gauge Length	2 1/2"	5/8"	1 1/4"	1/4"	3/16"

XBL 697-858

Fig. 1

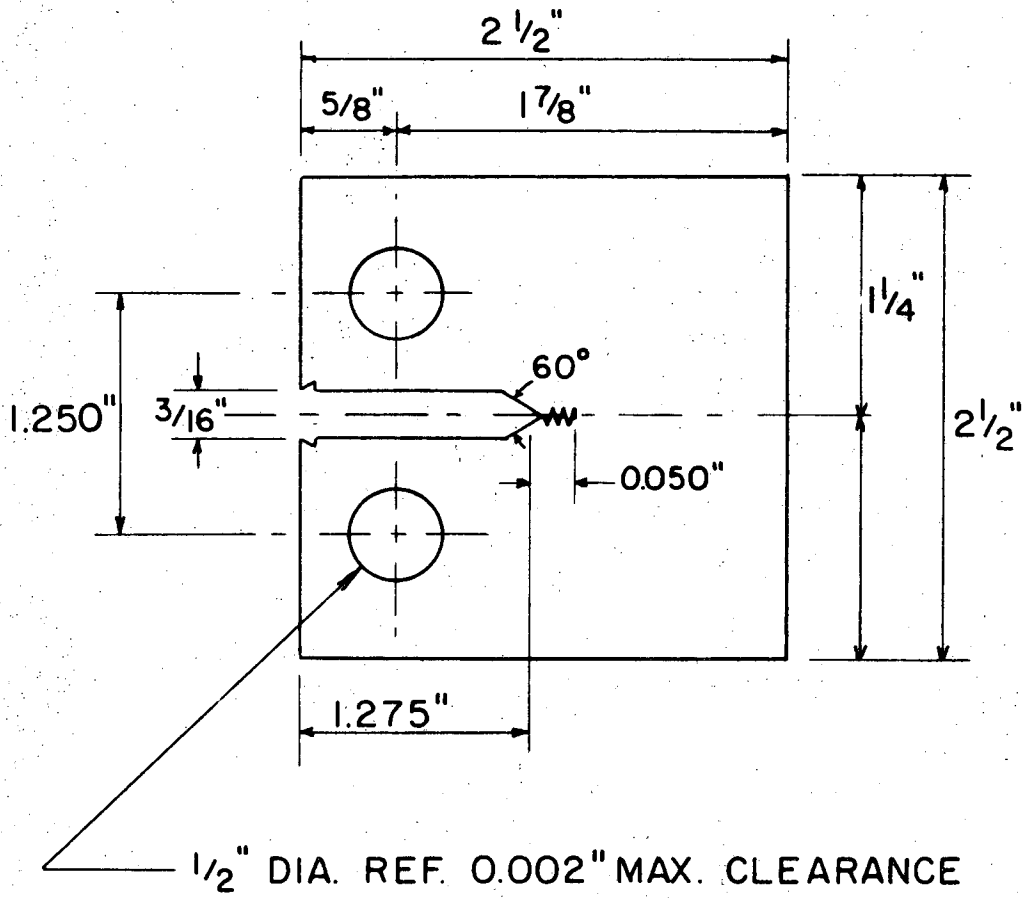

XBL 697-861

Fig. 2

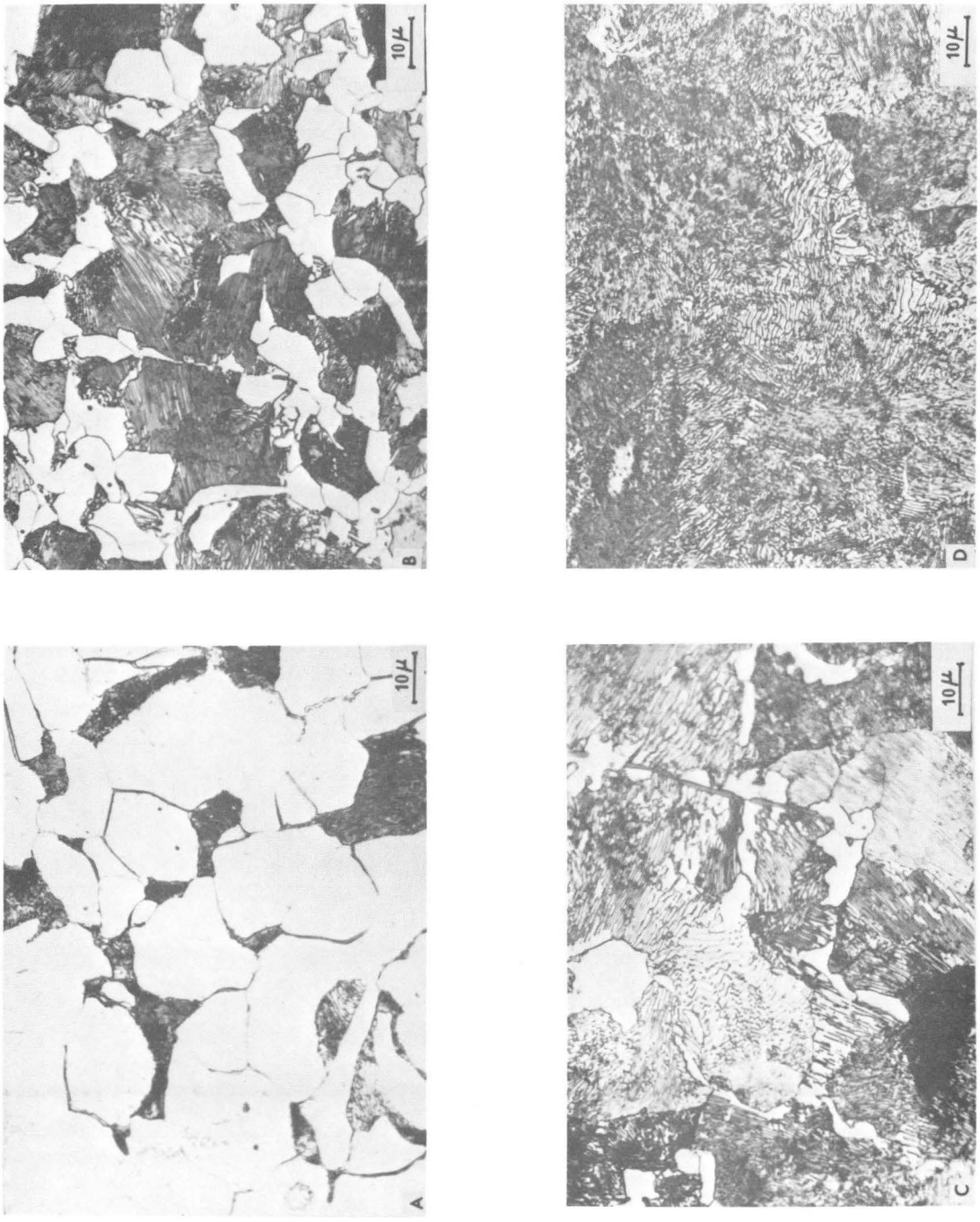

XBB 697-4526

Fig. 3

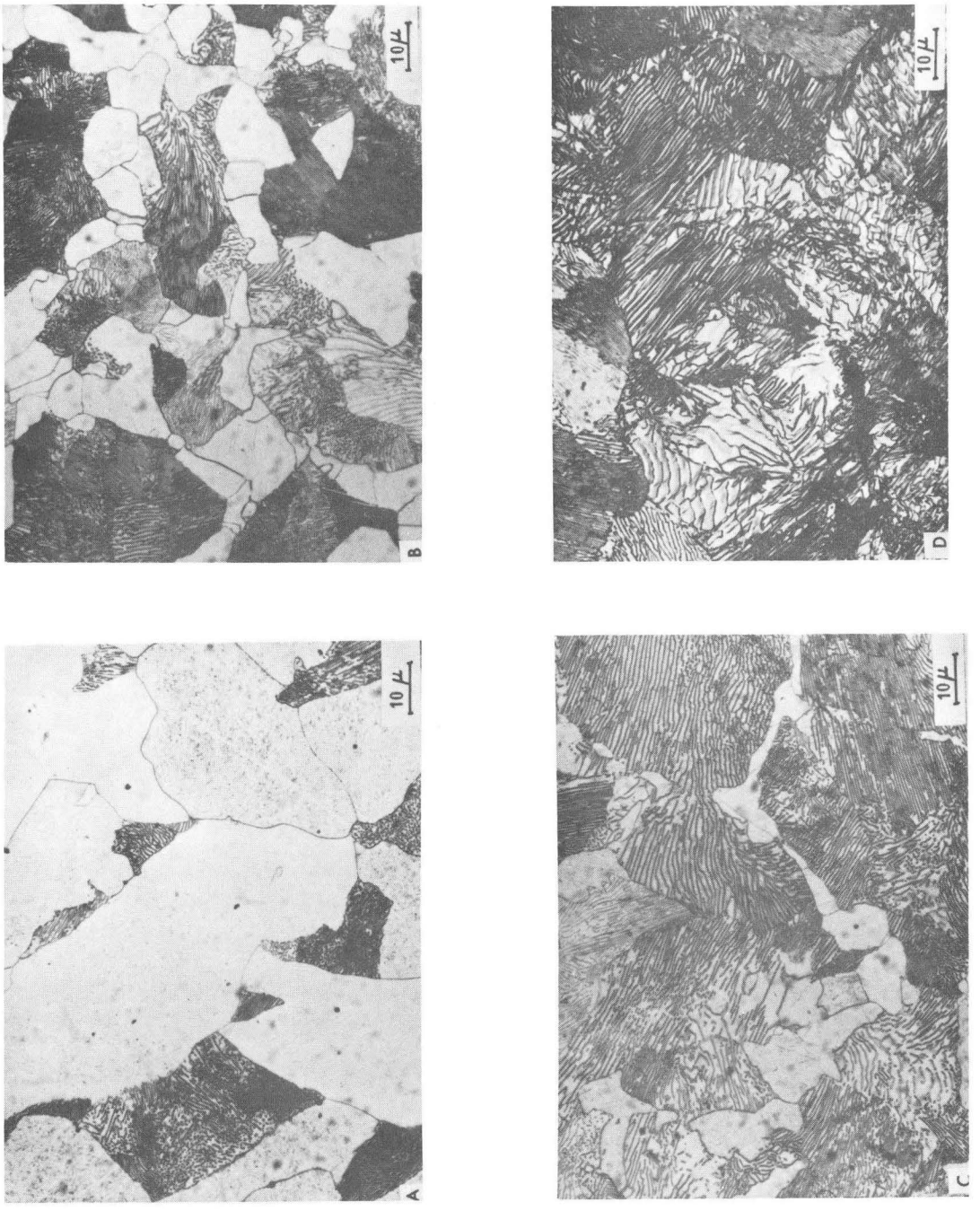

XBB 699-6003

Fig. 4

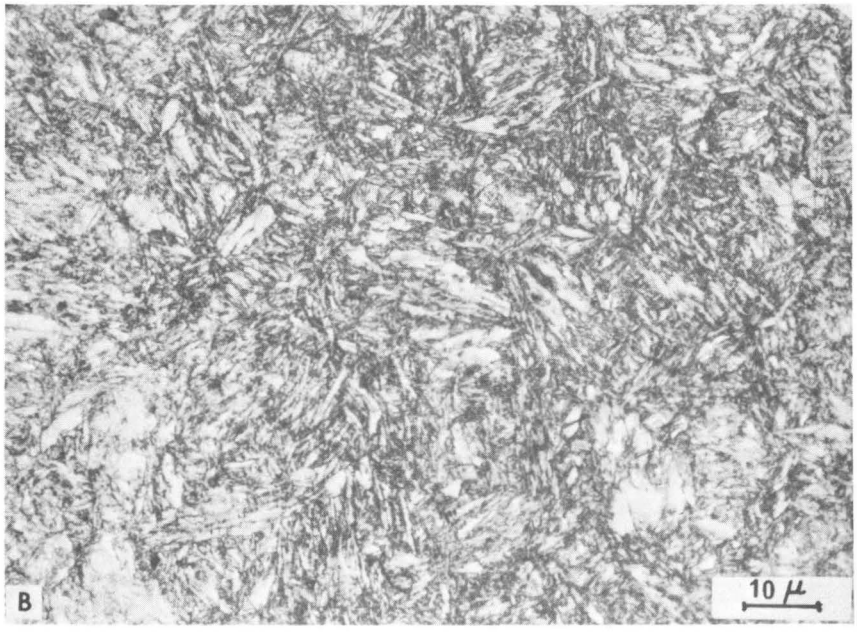

XBB 699-6305

Fig. 5

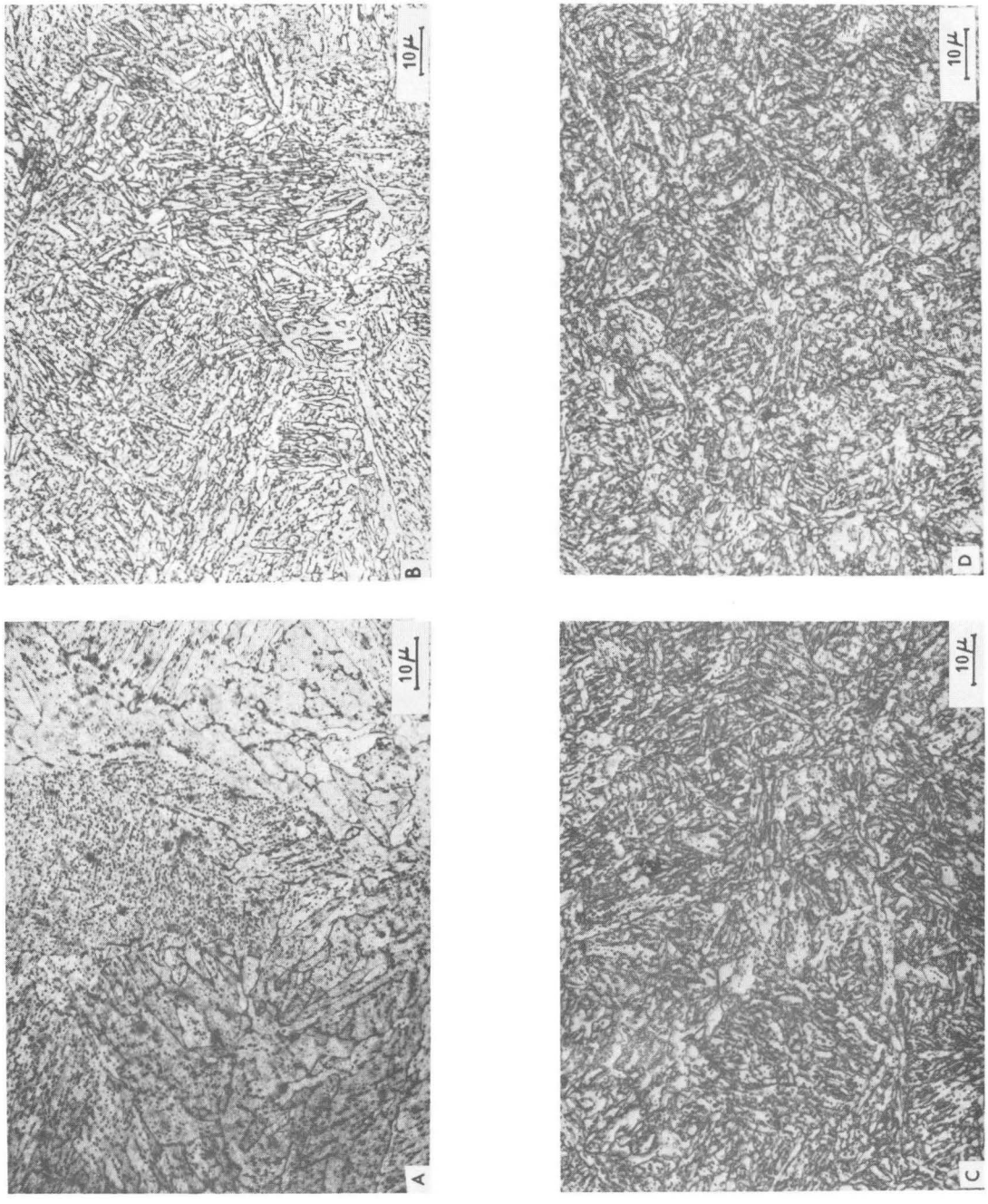

XBB 6910-6357

Fig. 6

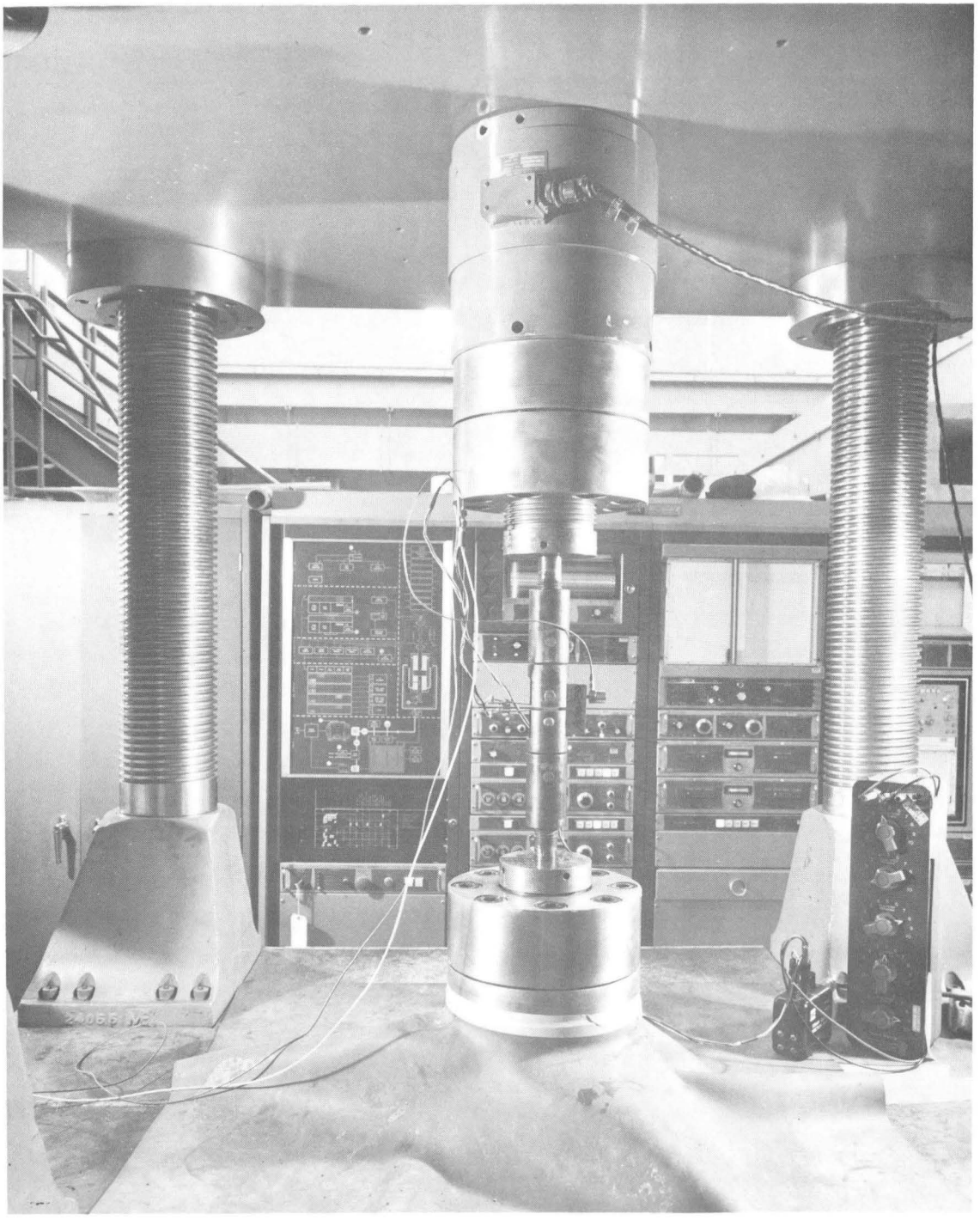

XBB 692-1024

Fig. 7

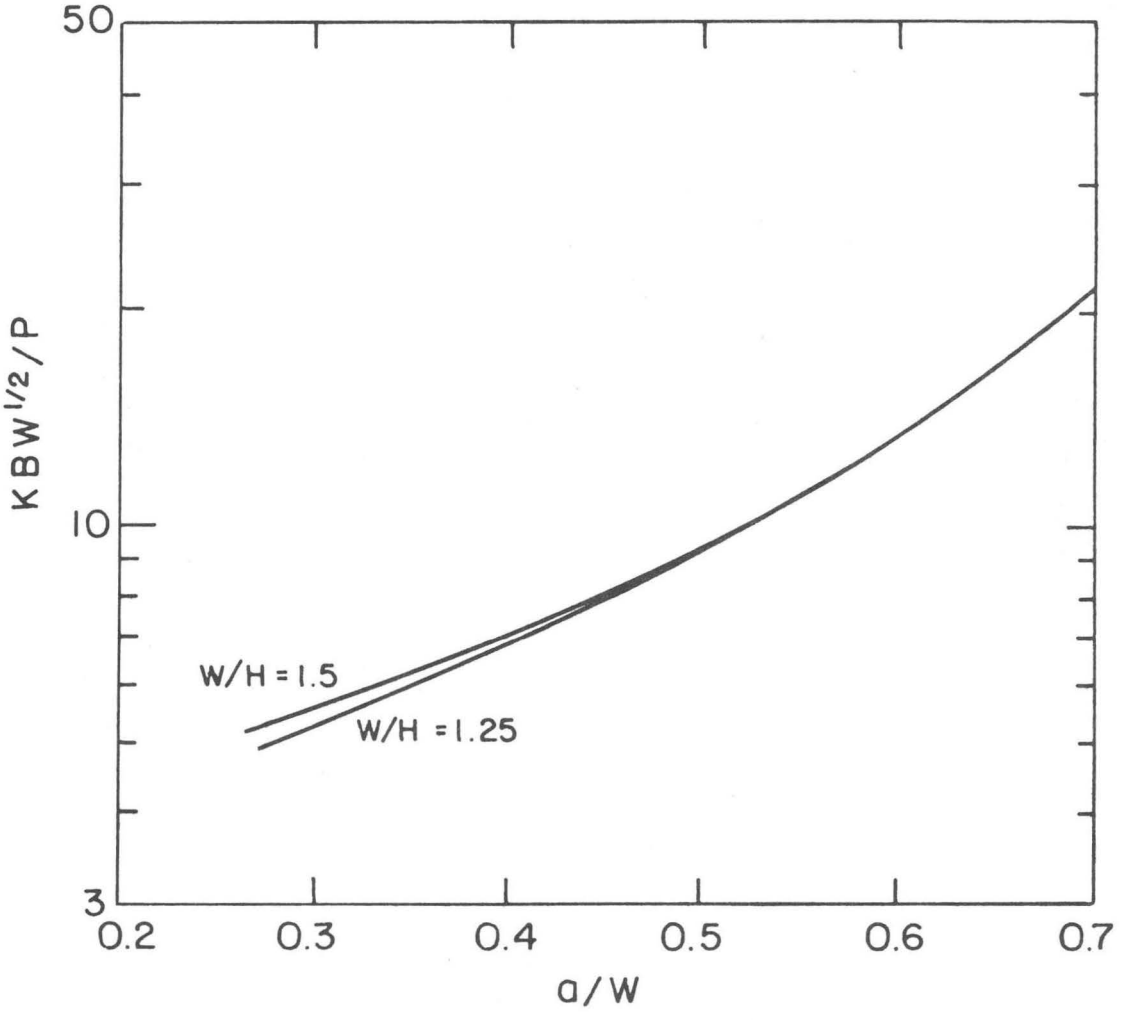

XBL 698-1385

Fig. 8

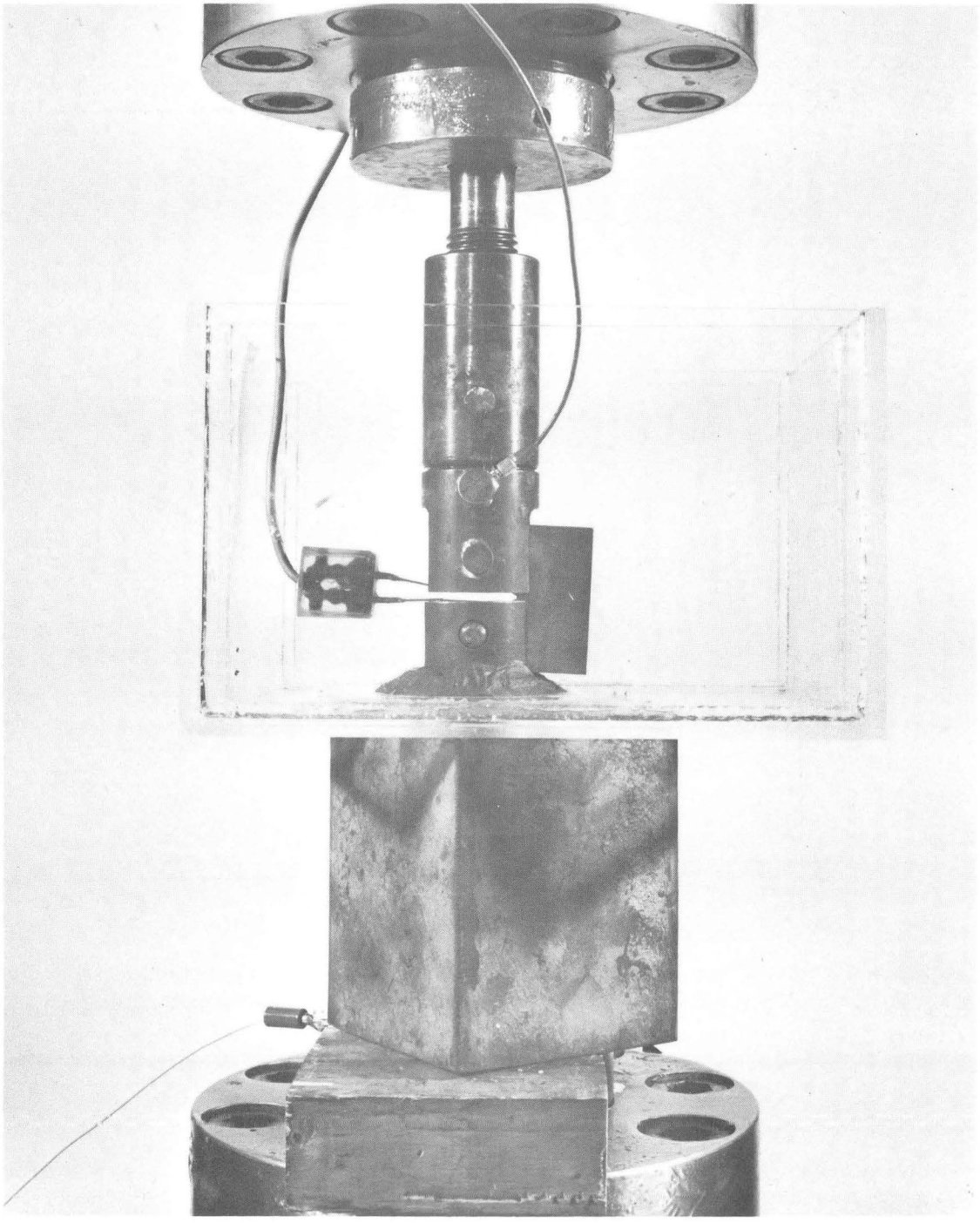

XBB 695-3399

Fig. 9

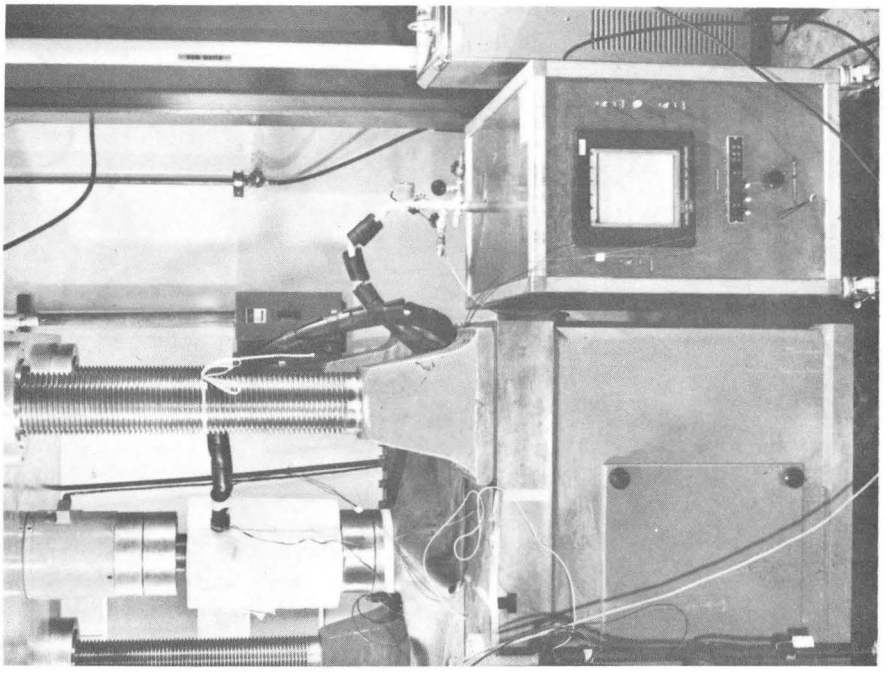

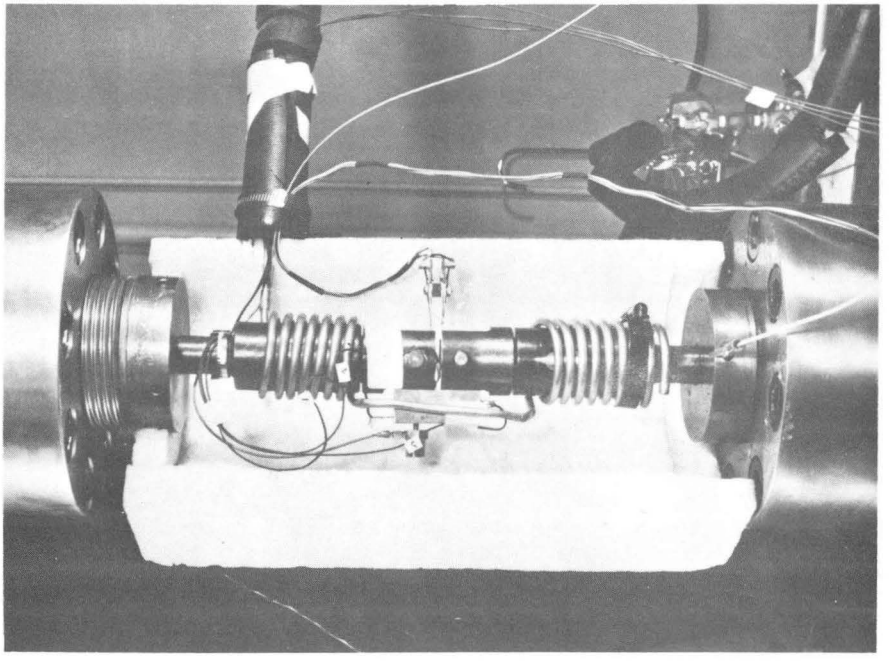

XBB 697-4645

Fig. 10

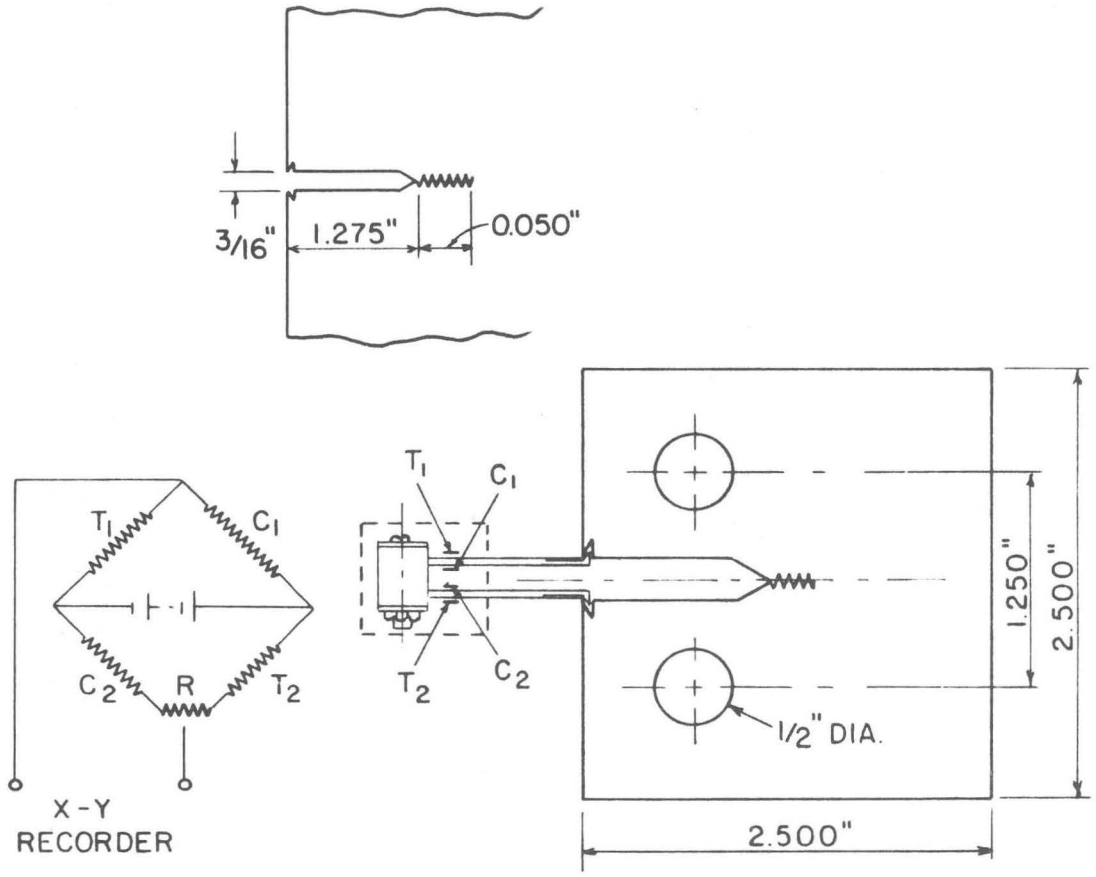

XBL 697-860

Fig. 11

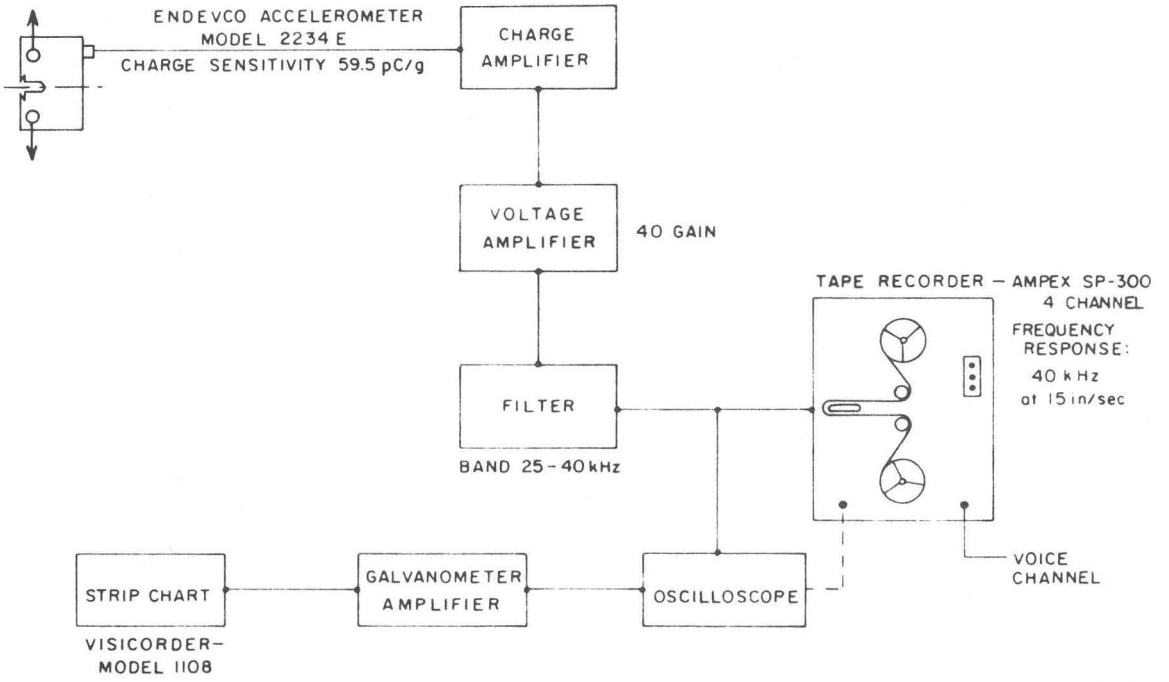
ENDEVCO ACCELEROMETER
MODEL 2234 E
CHARGE SENSITIVITY 59.5 pC/g
CHARGE AMPLIFIER
VOLTAGE AMPLIFIER
40 GAIN
TAPE RECORDER – AMPEX SP-300
4 CHANNEL
FREQUENCY RESPONSE:
40 kHz
at 15 in/sec
FILTER
BAND 25-40 kHz
STRIP CHART
VISICORDER-
MODEL 1108
GALVANOMETER AMPLIFIER
OSCILLOSCOPE
VOICE CHANNEL
XBL 697-859

Fig. 12

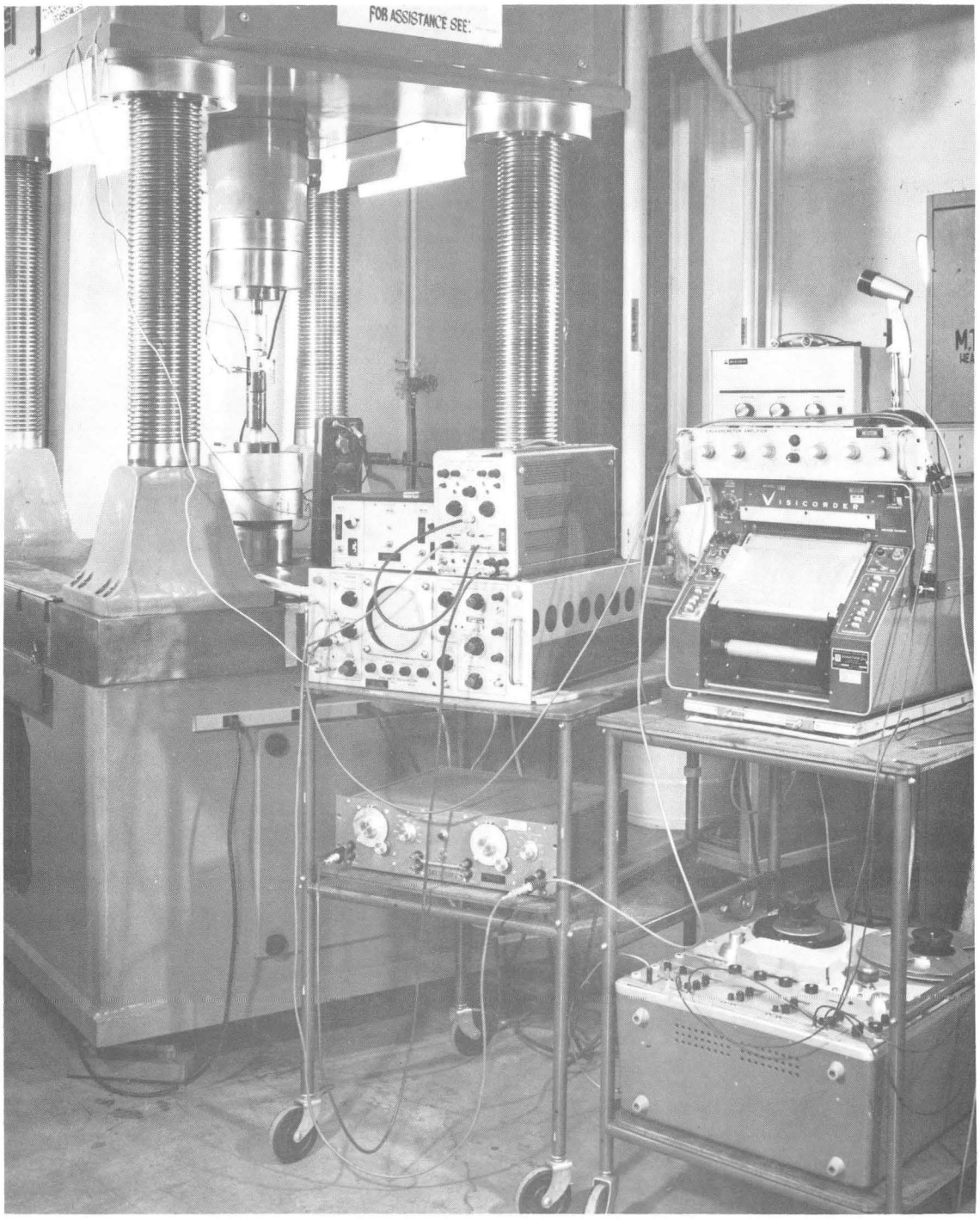

XBB 697-4671

Fig. 13

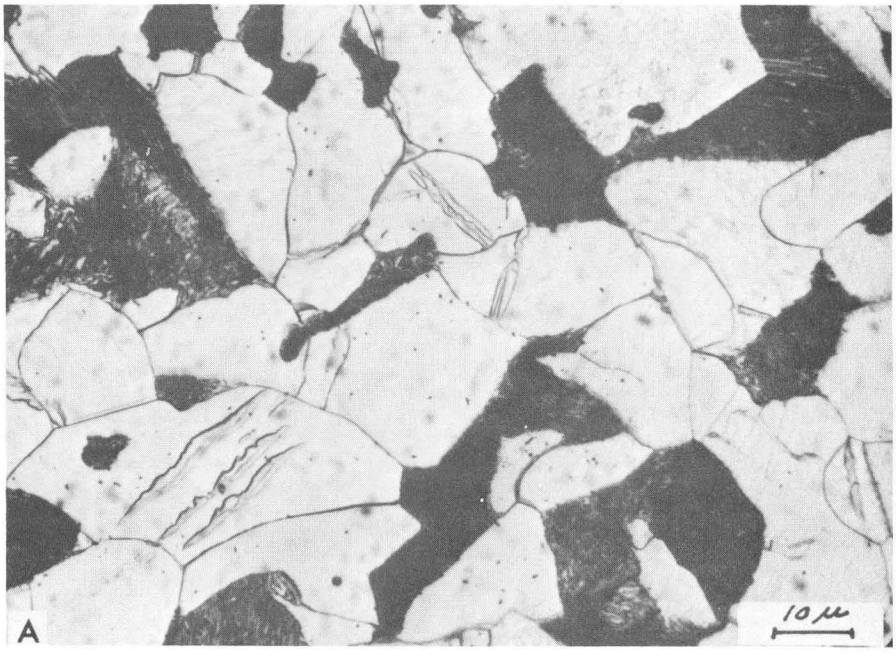

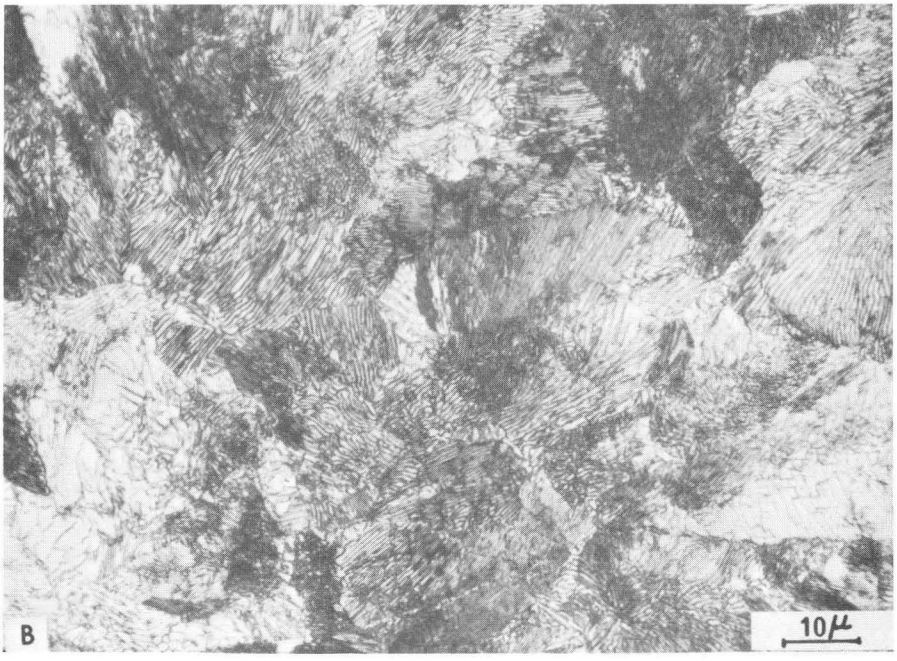

XBB 6910-6406

Fig. 14

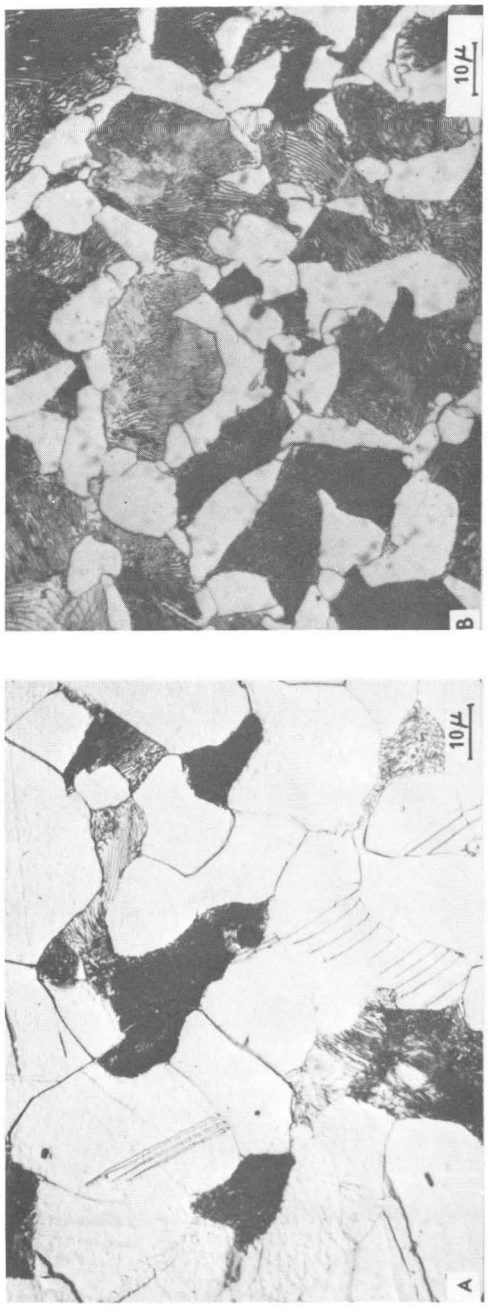

XBB 6910-6358

Fig. 15

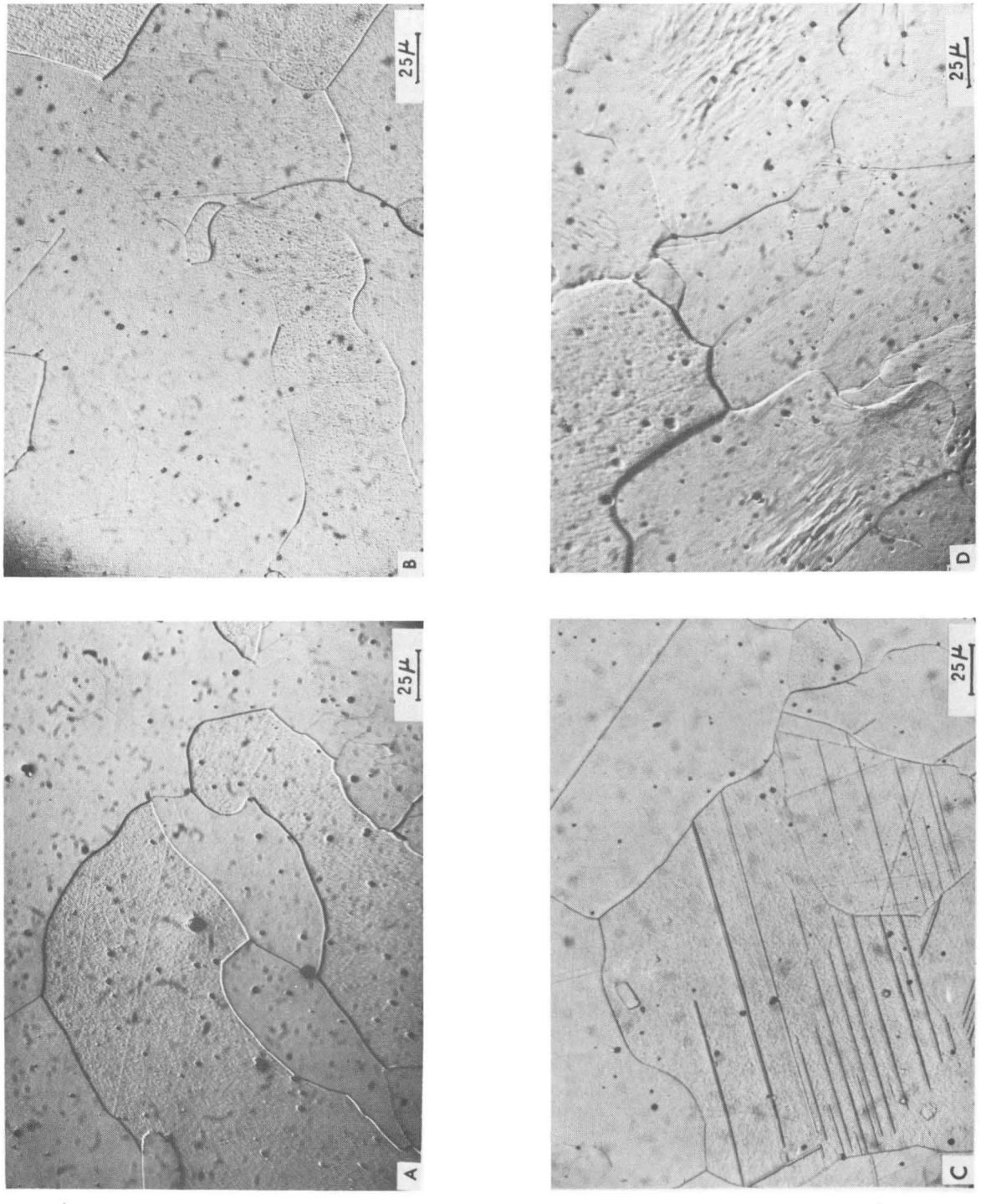

XBB 6910-6405

Fig. 16

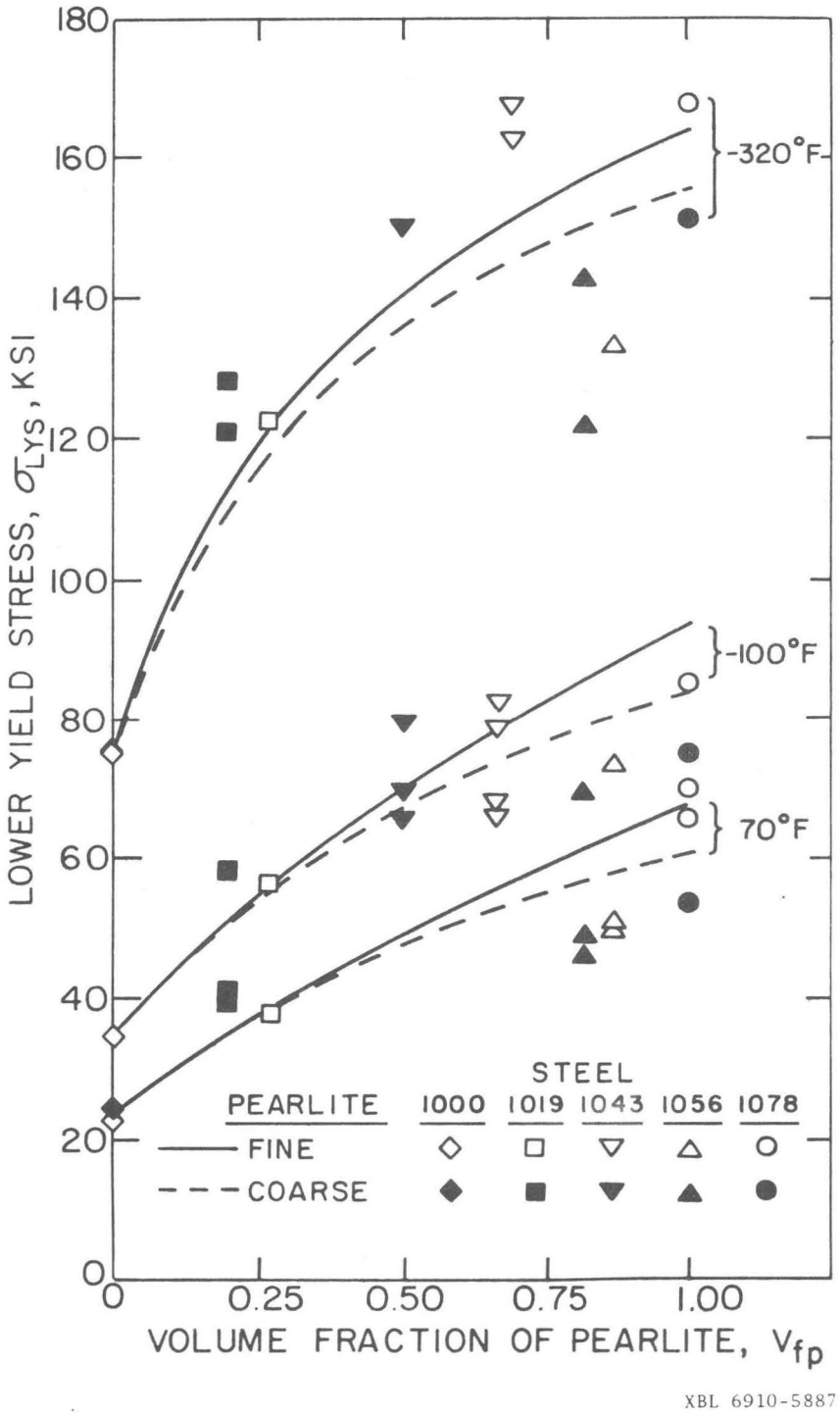
LOWER YIELD STRESS, σ_{LYS}, KSI
VOLUME FRACTION OF PEARLITE, V_{fp}
-320°F
-100°F
70°F
STEEL
PEARLITE
1000
1019
1043
1056
1078
FINE
COARSE
XBL 6910-5887

Fig. 17

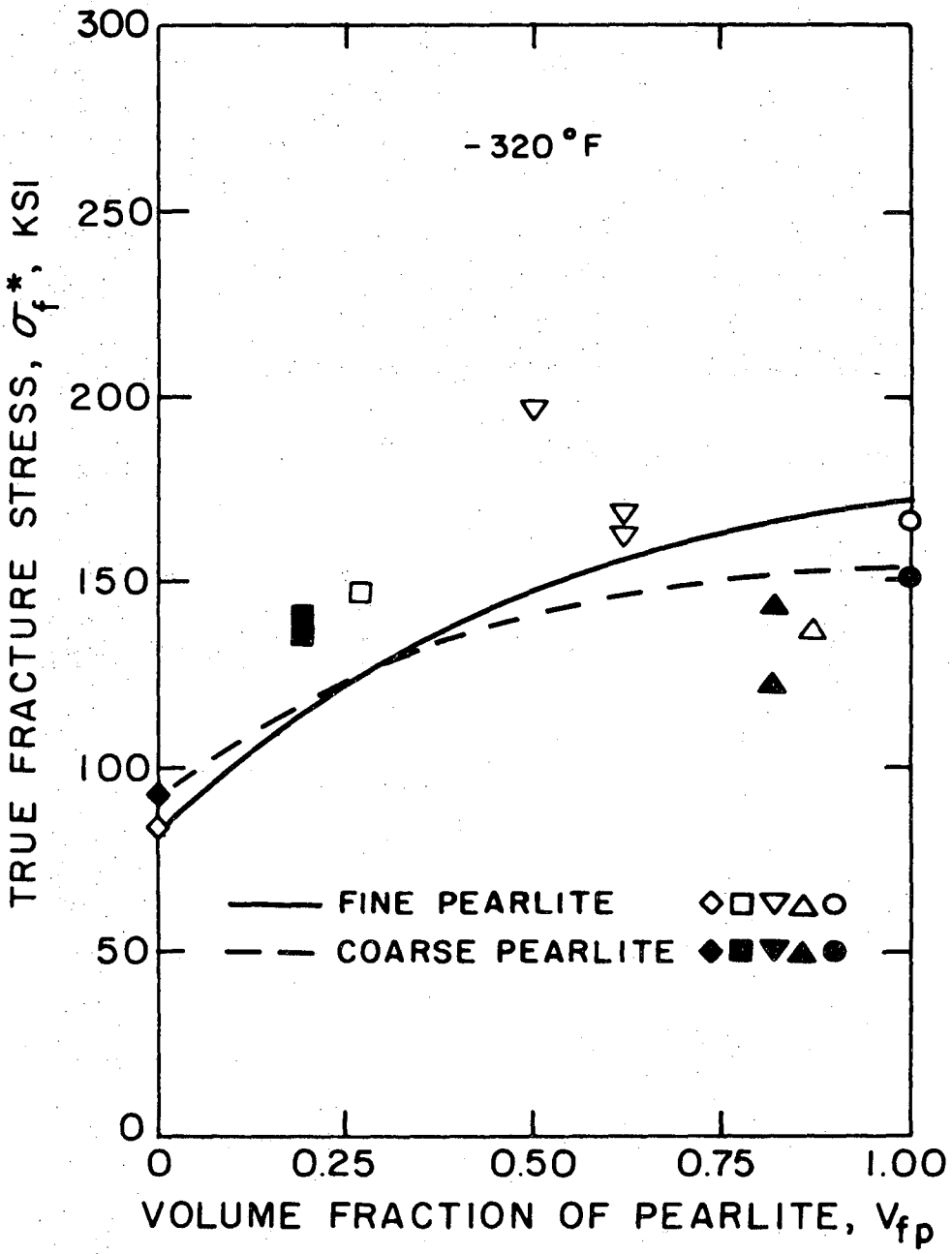

XBL 6910-5882

Fig. 18

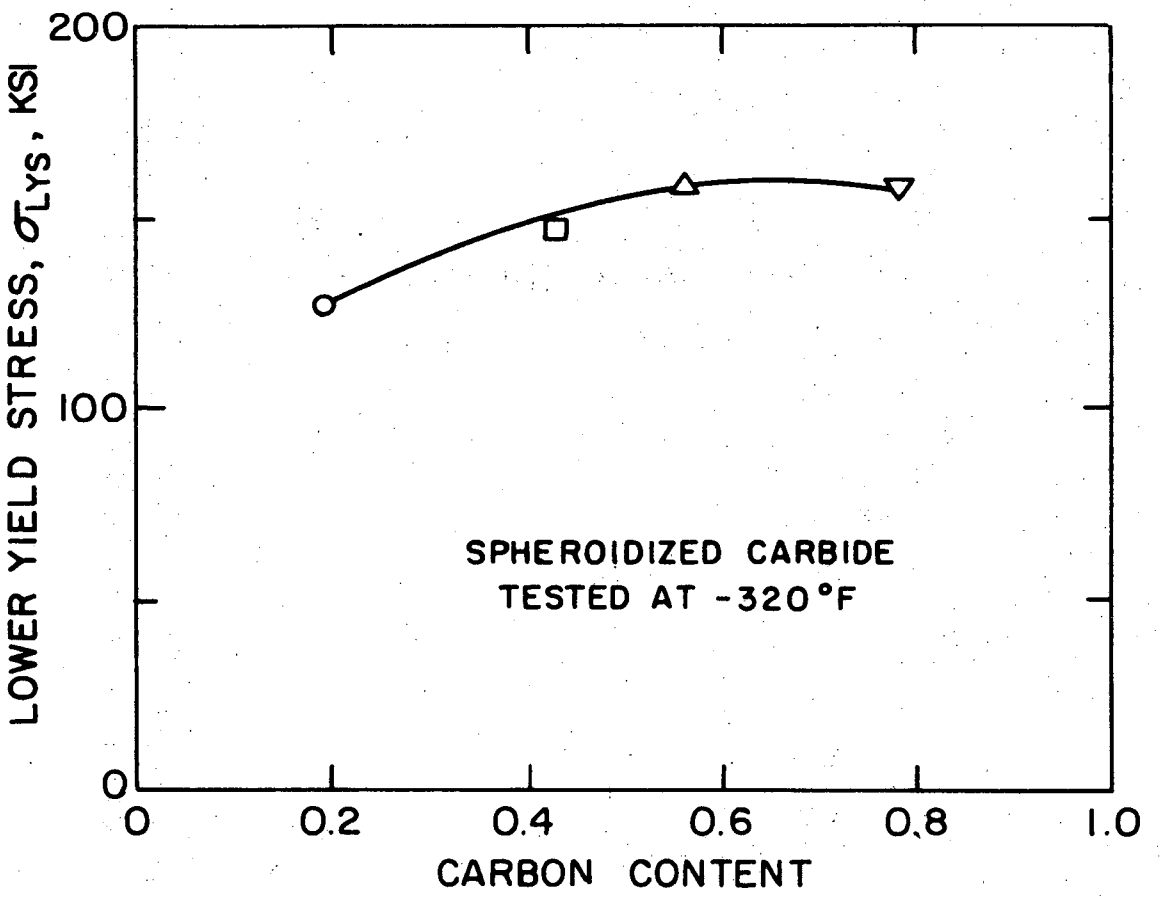

XBL 6910-5890

Fig. 19

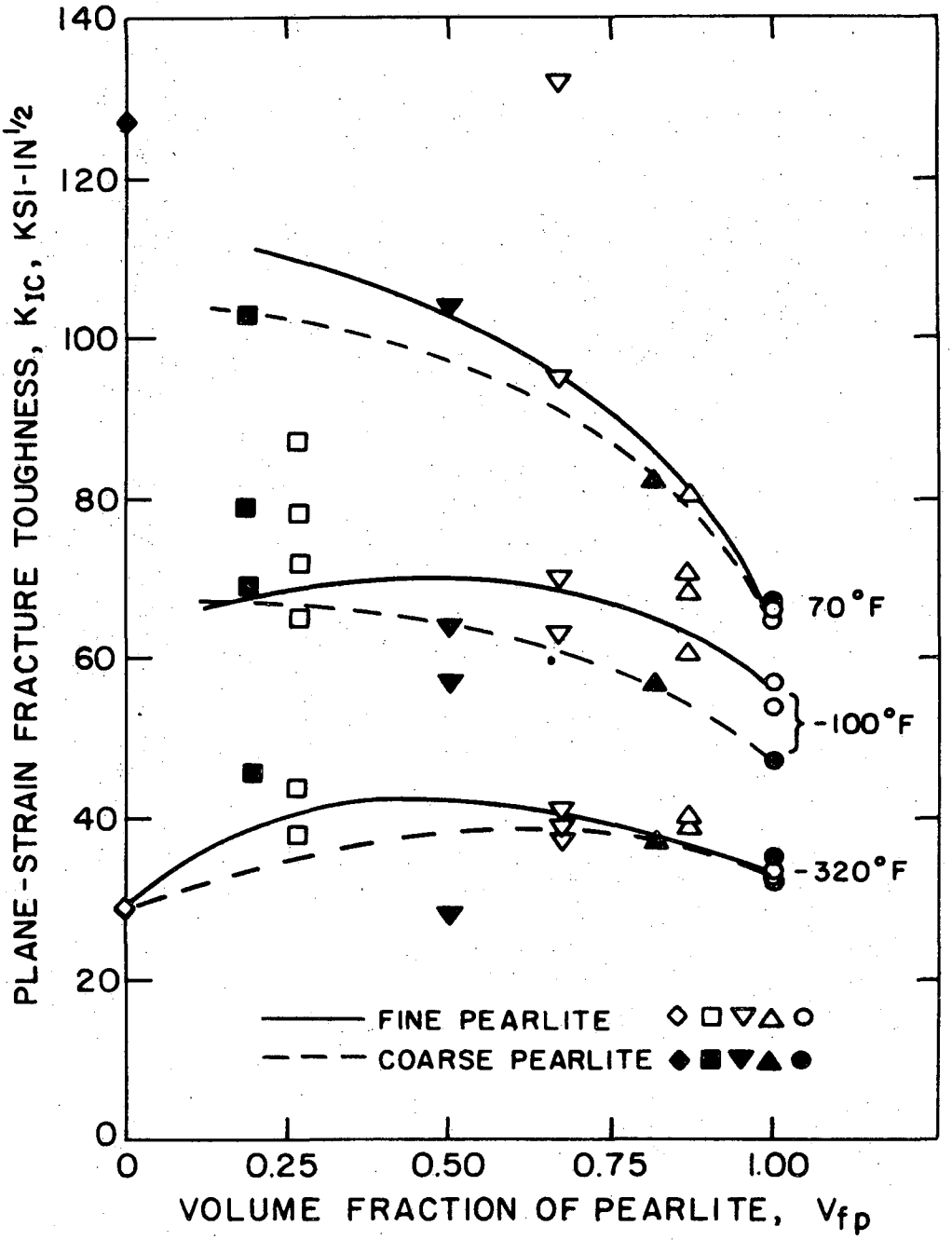

XBL 6910-5883

Fig. 20

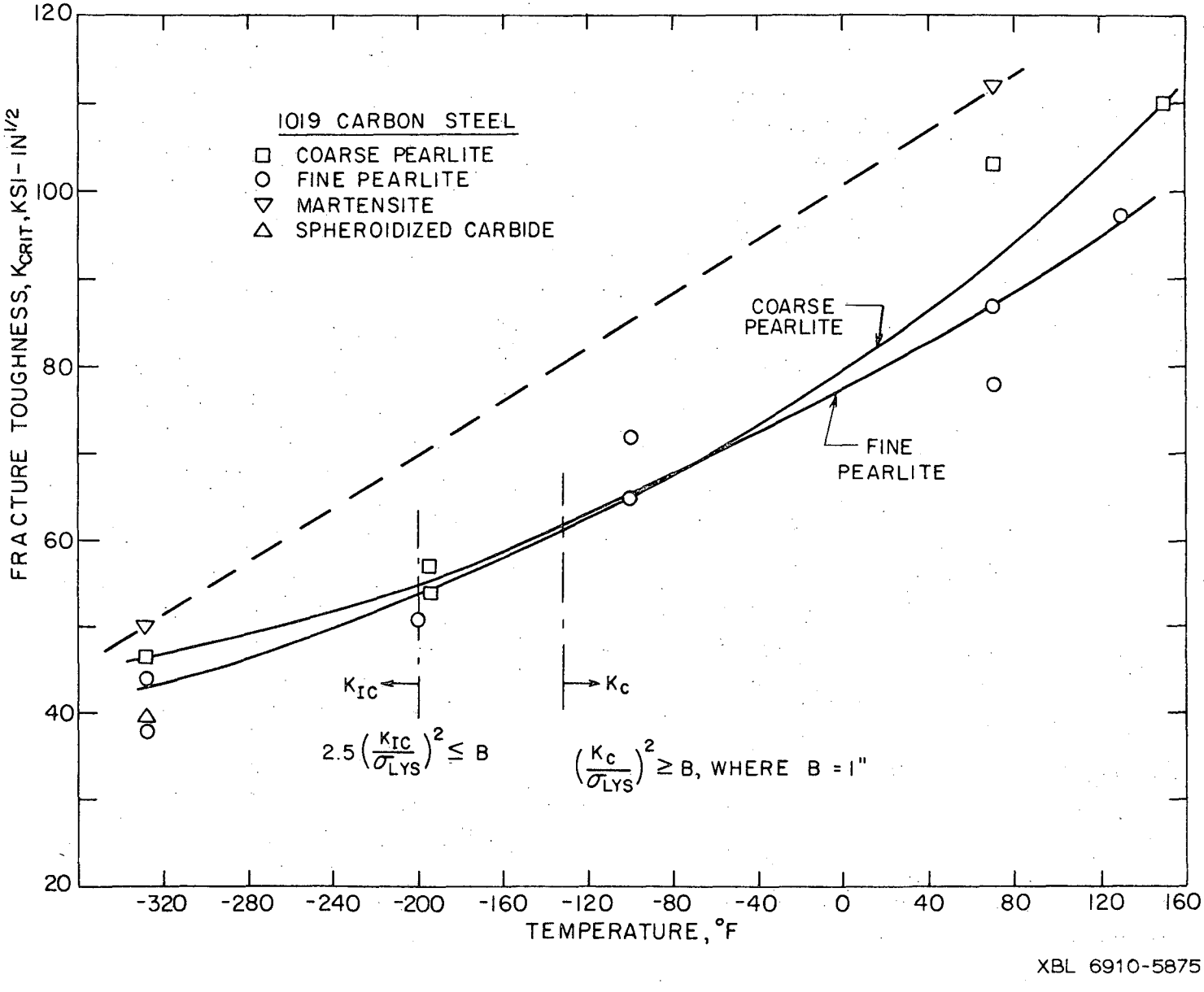
1019 CARBON STEEL
COARSE PEARLITE
FINE PEARLITE
MARTENSITE
SPHEROIDIZED CARBIDE
COARSE PEARLITE
FINE PEARLITE
K_{IC}
K_C
$2.5\left(\frac{K_{IC}}{\sigma_{LYS}}\right)^2 \leq B$
$\left(\frac{K_C}{\sigma_{LYS}}\right)^2 \geq B$, WHERE B = 1"
FRACTURE TOUGHNESS, K_{CRIT}, KSI-$IN^{1/2}$
TEMPERATURE, °F
120
100
80
60
40
20
-320
-280
-240
-200
-160
-120
-80
-40
0
40
80
120
160
XBL 6910-5875

Fig. 21

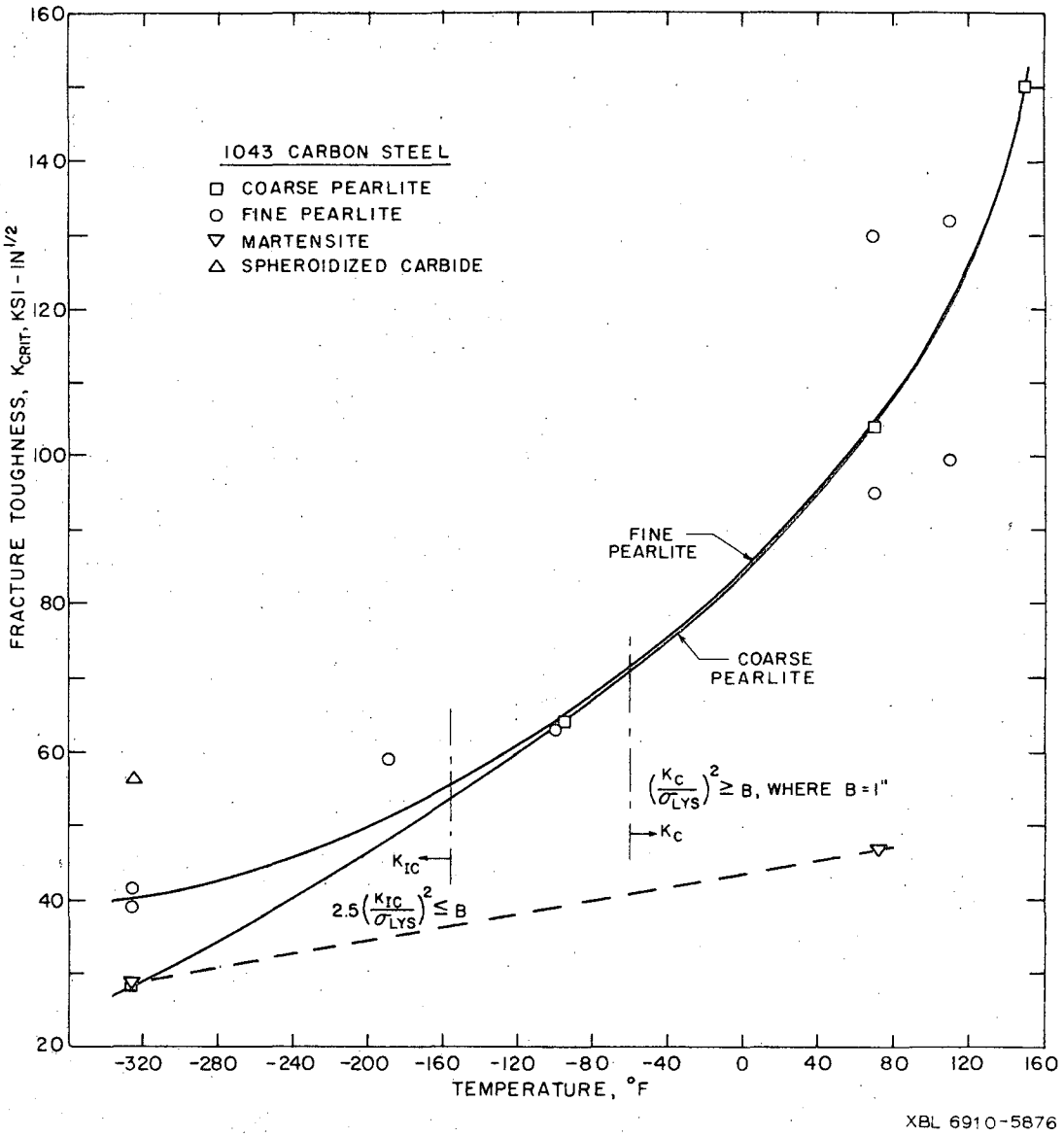
1043 CARBON STEEL
COARSE PEARLITE
FINE PEARLITE
MARTENSITE
SPHEROIDIZED CARBIDE
FRACTURE TOUGHNESS, K_{CRIT}, KSI - IN$^{1/2}$
TEMPERATURE, °F
FINE PEARLITE
COARSE PEARLITE
$\left(\frac{K_C}{\sigma_{LYS}}\right)^2 \geq B$, WHERE B = 1"
K_C
K_{IC}
$2.5\left(\frac{K_{IC}}{\sigma_{LYS}}\right)^2 \leq B$
XBL 6910-5876

Fig. 22

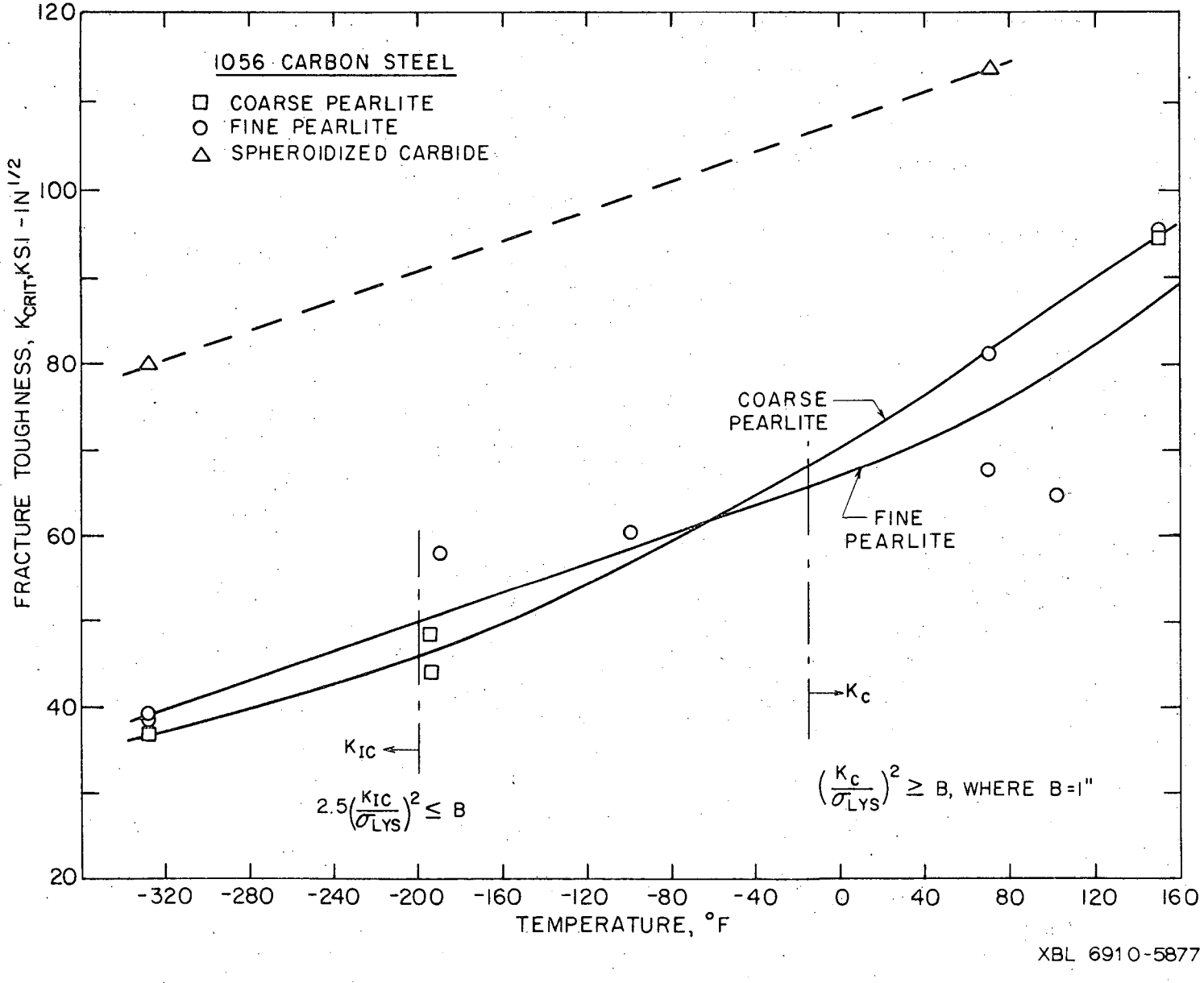
1056 CARBON STEEL
COARSE PEARLITE
FINE PEARLITE
SPHEROIDIZED CARBIDE
FRACTURE TOUGHNESS, K_{CRIT}, KSI - $IN^{1/2}$
120
100
80
60
40
20
COARSE PEARLITE
FINE PEARLITE
K_C
K_{IC}
$2.5\left(\frac{K_{IC}}{\sigma_{LYS}}\right)^2 \leq B$
$\left(\frac{K_C}{\sigma_{LYS}}\right)^2 \geq B$, WHERE B=1"
-320 -280 -240 -200 -160 -120 -80 -40 0 40 80 120 160
TEMPERATURE, °F
XBL 6910-5877

Fig. 23

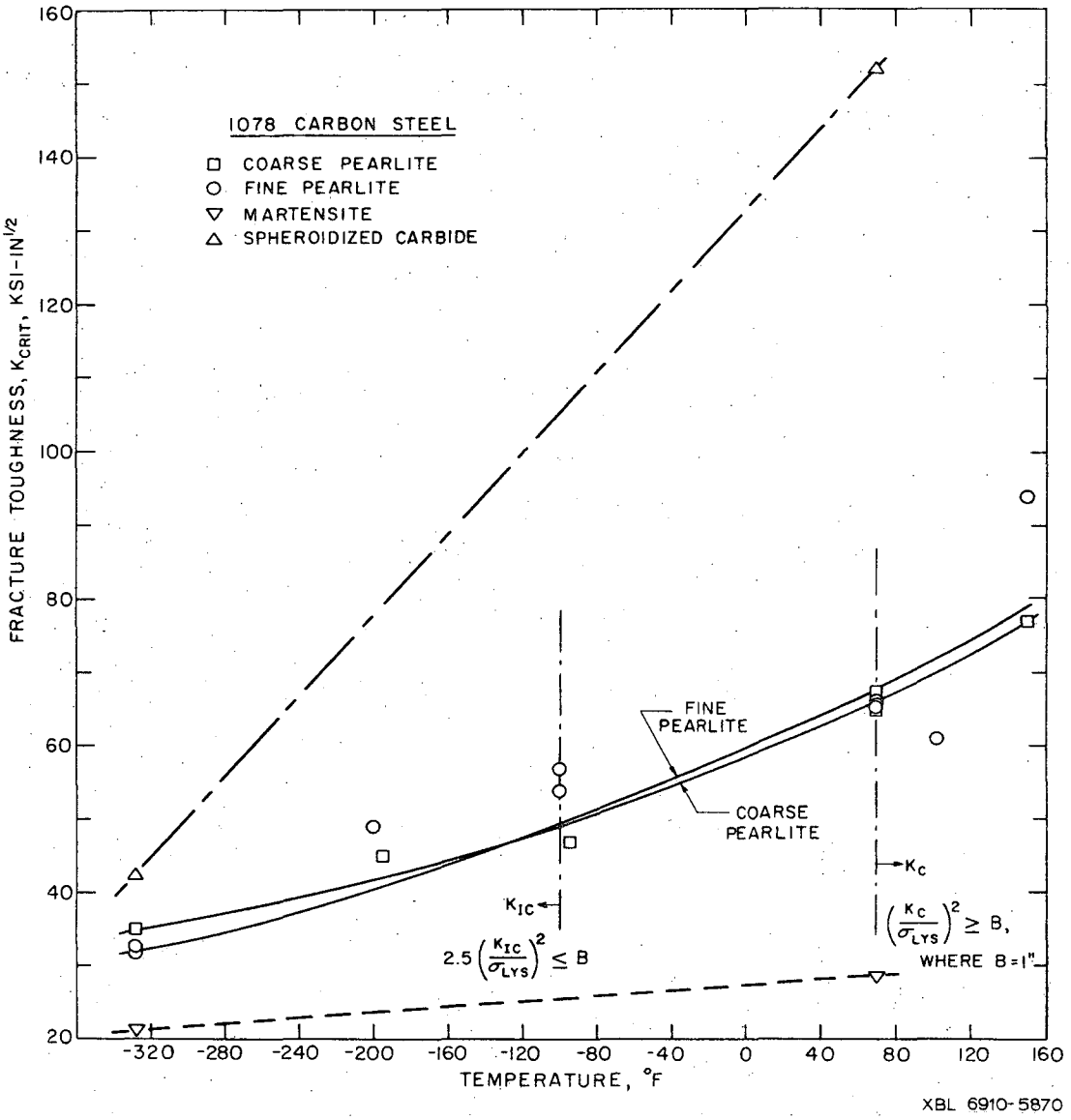
1078 CARBON STEEL
COARSE PEARLITE
FINE PEARLITE
MARTENSITE
SPHEROIDIZED CARBIDE
FRACTURE TOUGHNESS, K_{CRIT}, KSI-IN$^{1/2}$
TEMPERATURE, °F
FINE PEARLITE
COARSE PEARLITE
K_{IC}
K_C
$2.5\left(\frac{K_{IC}}{\sigma_{LYS}}\right)^2 \leq B$
$\left(\frac{K_C}{\sigma_{LYS}}\right)^2 \geq B$,
WHERE B=1"
XBL 6910-5870

Fig. 24

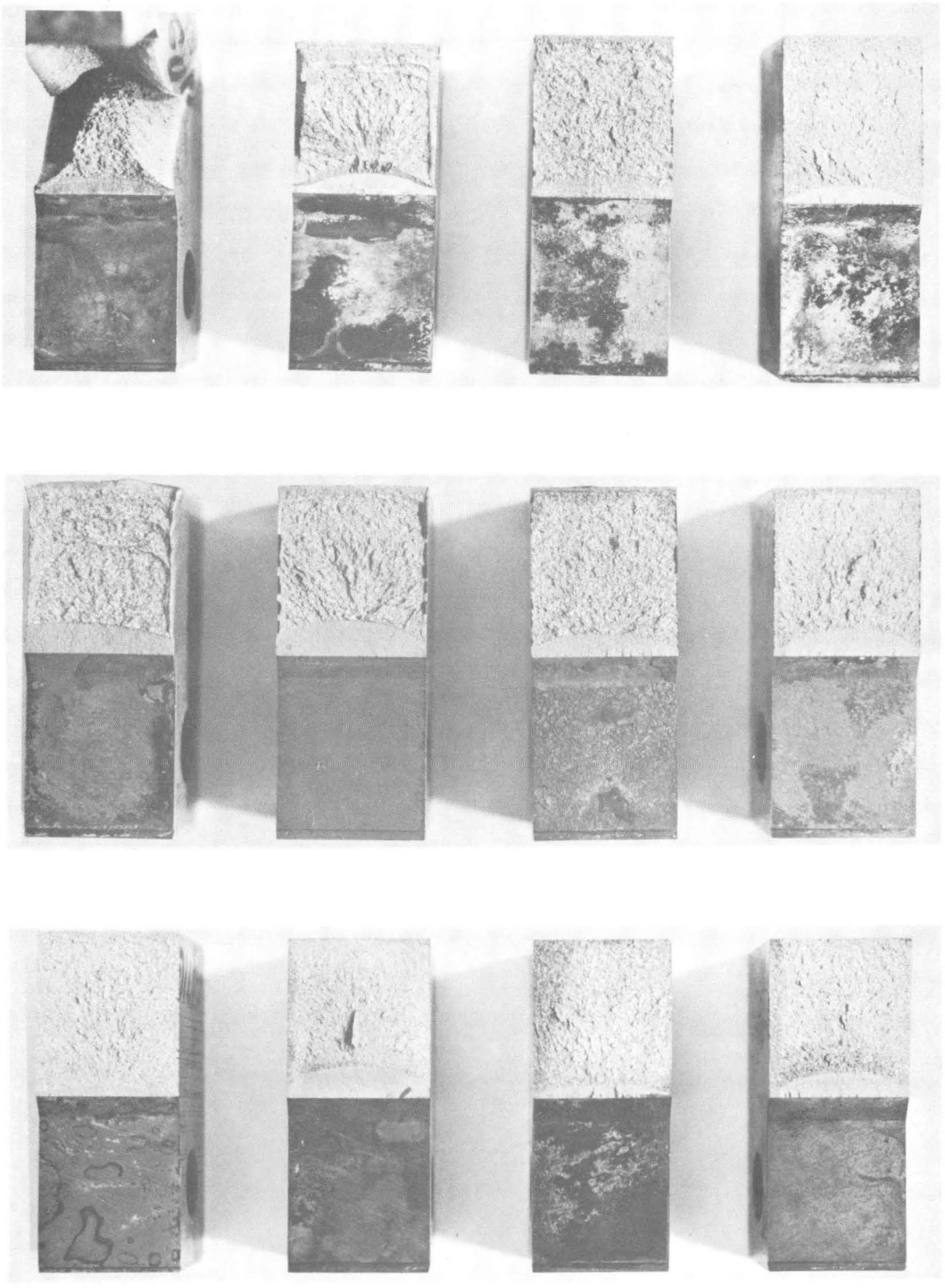

XBB 697-4527

Fig. 25

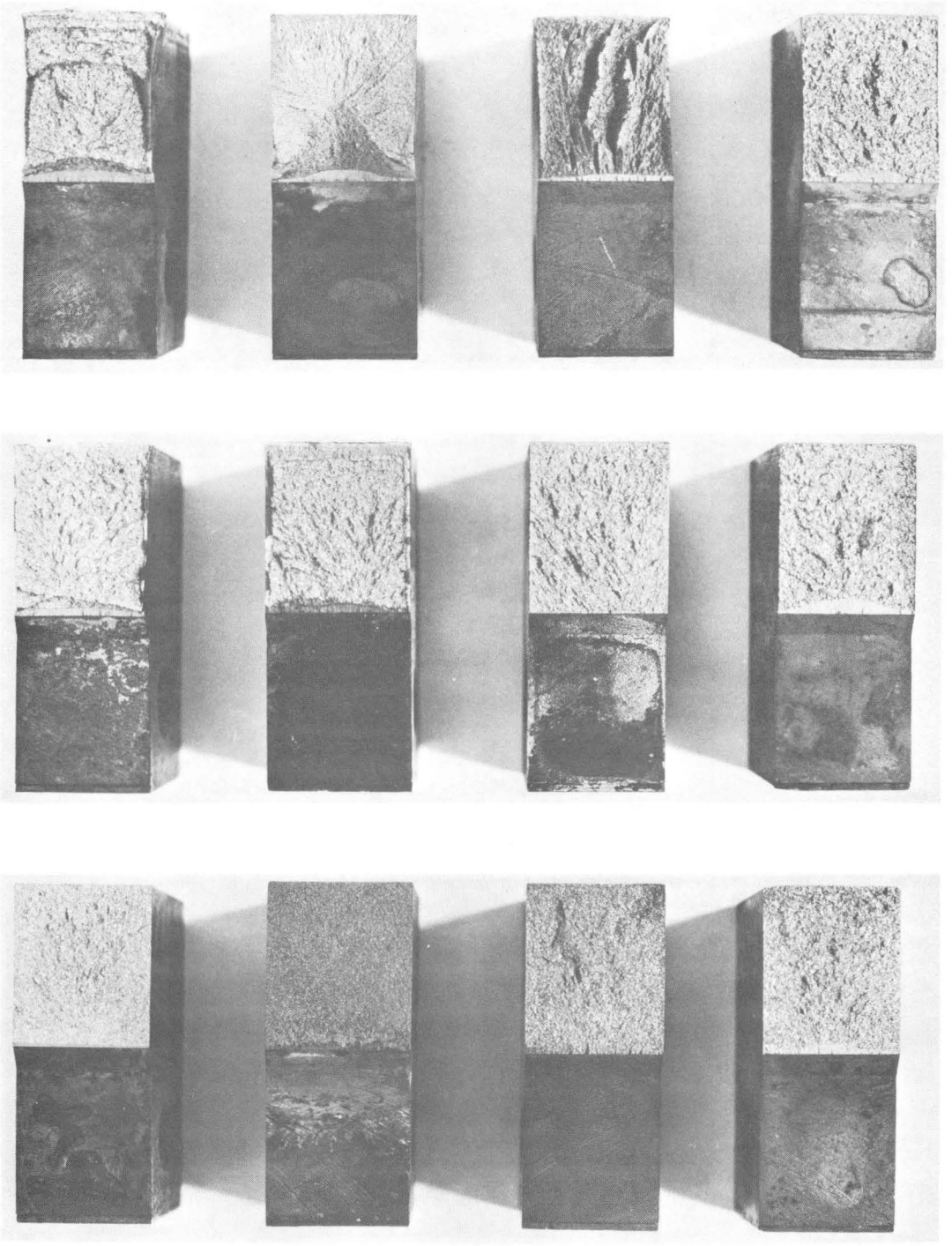

XBB 698-5686

Fig. 26

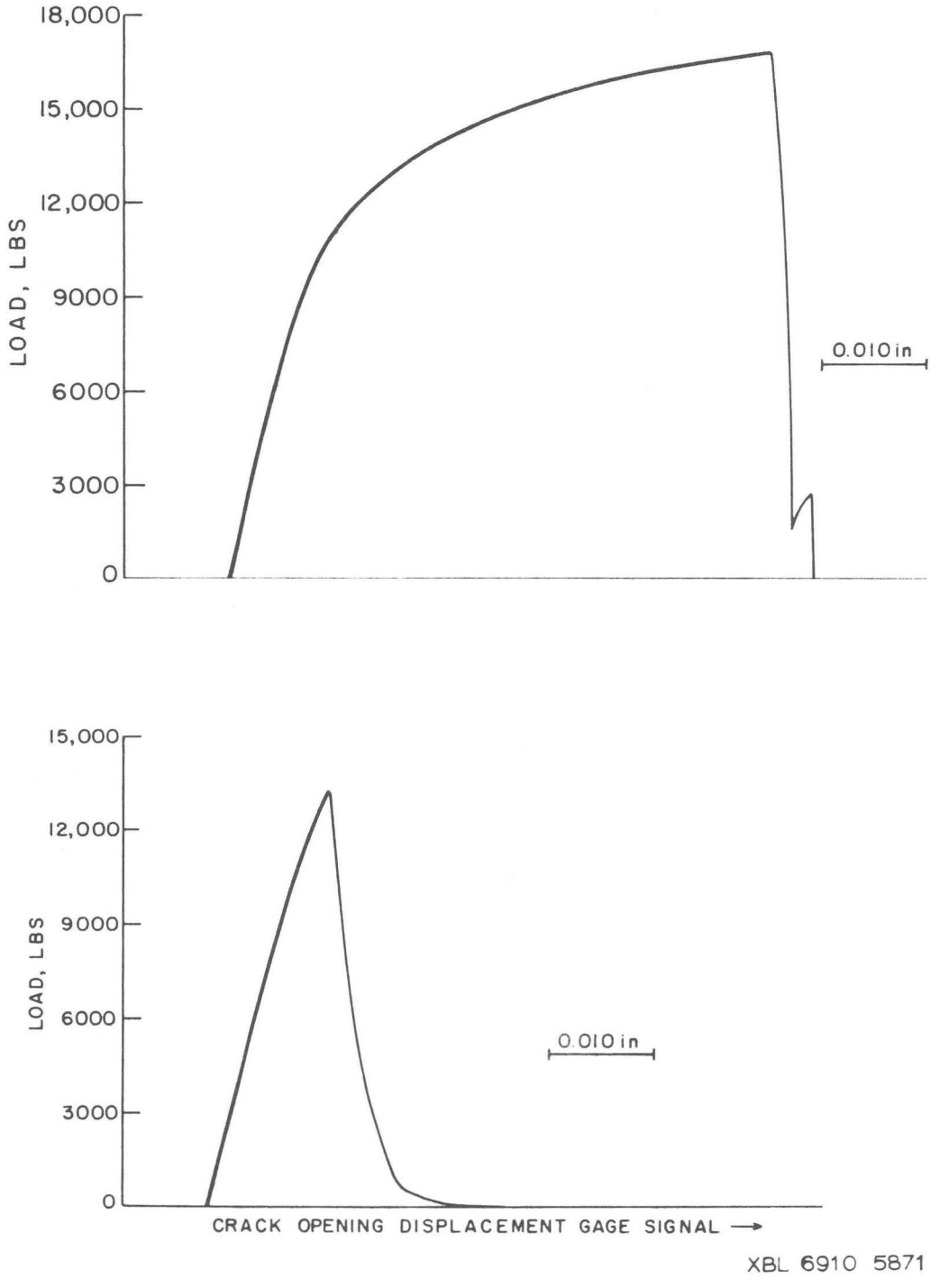
18,000
15,000
12,000
9000
6000
3000
0
LOAD, LBS
0.010 in
15,000
12,000
9000
6000
3000
0
LOAD, LBS
0.010 in
CRACK OPENING DISPLACEMENT GAGE SIGNAL →
XBL 6910 5871

Fig. 27

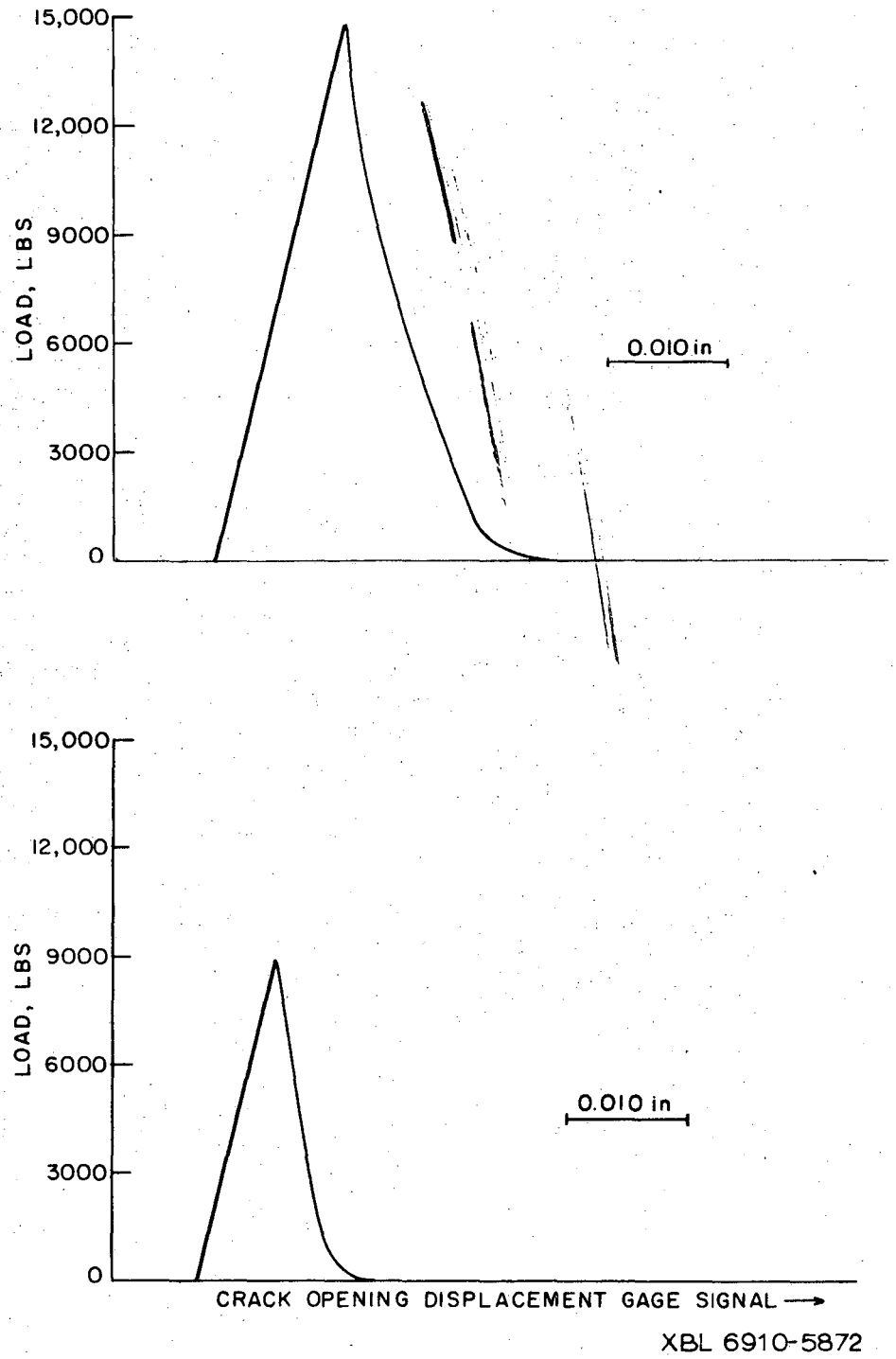
15,000
12,000
9000
6000
3000
0
LOAD, LBS
0.010 in
15,000
12,000
9000
6000
3000
0
LOAD, LBS
0.010 in
CRACK OPENING DISPLACEMENT GAGE SIGNAL →
XBL 6910-5872

Fig. 28

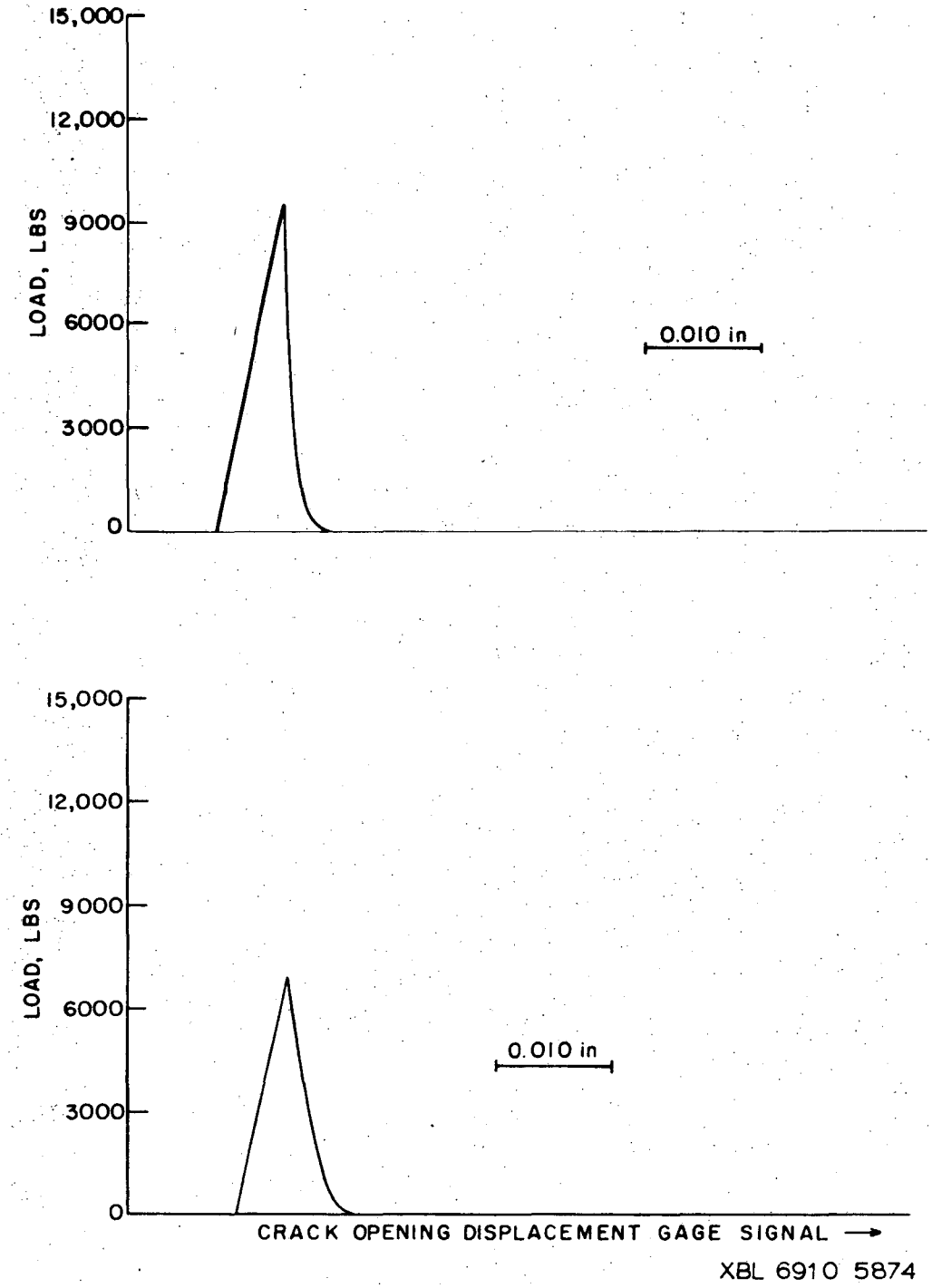
15,000
12,000
9000
6000
3000
0
LOAD, LBS
0.010 in
15,000
12,000
9000
6000
3000
0
LOAD, LBS
0.010 in
CRACK OPENING DISPLACEMENT GAGE SIGNAL →
XBL 6910 5874

Fig. 29

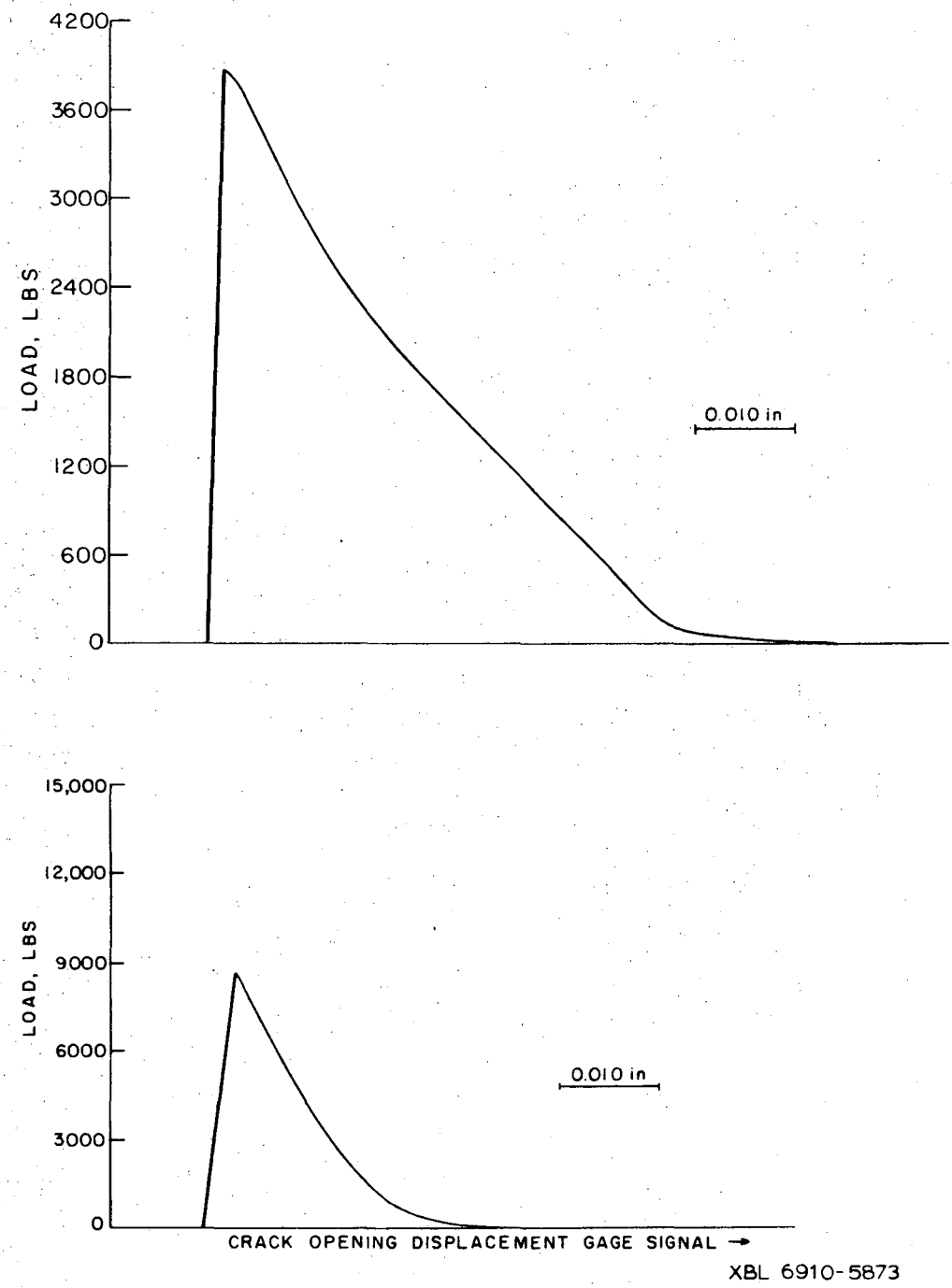
4200
3600
3000
2400
1800
1200
600
0
LOAD, LBS
0.010 in
15,000
12,000
9000
6000
3000
0
LOAD, LBS
0.010 in
CRACK OPENING DISPLACEMENT GAGE SIGNAL →
XBL 6910-5873

Fig. 30

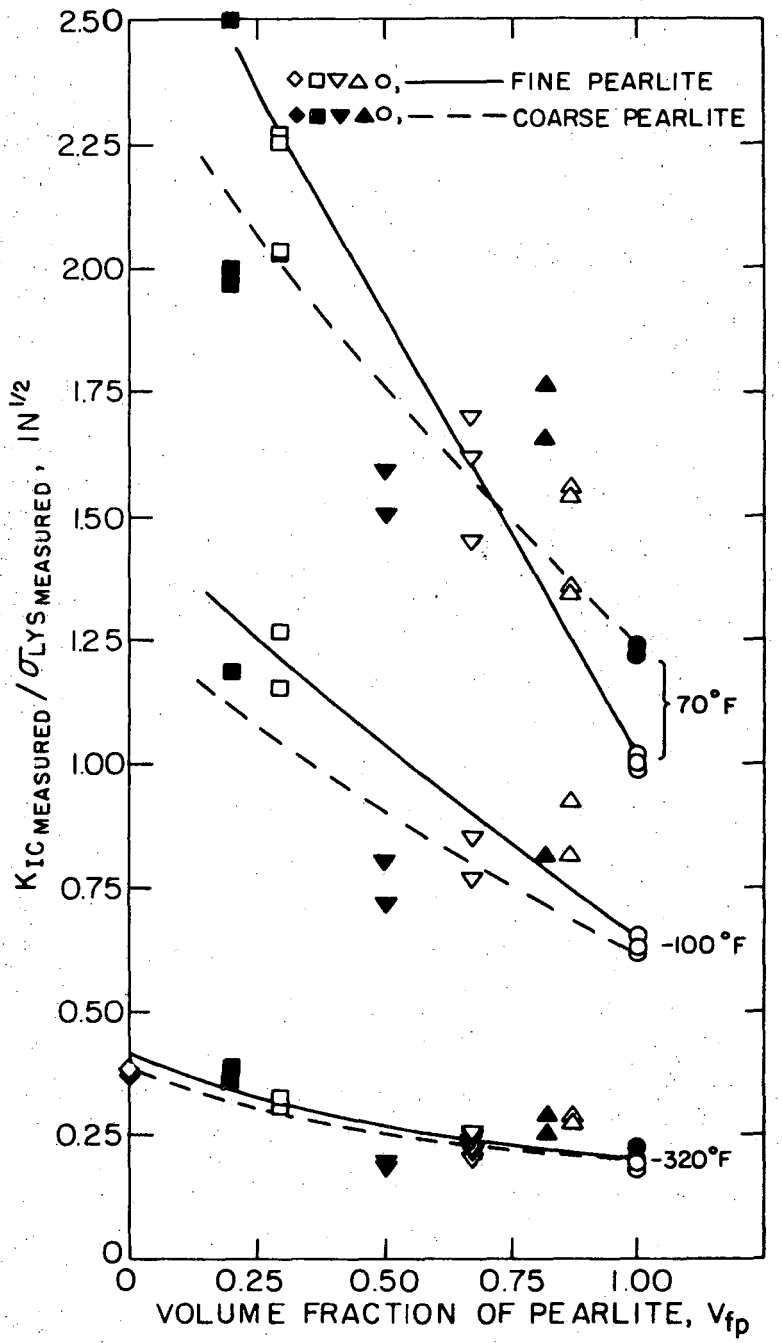
2.50
2.25
2.00
1.75
1.50
1.25
1.00
0.75
0.50
0.25
0
0
0.25
0.50
0.75
1.00
VOLUME FRACTION OF PEARLITE, V_{fp}
$K_{IC\ MEASURED} / \sigma_{LYS\ MEASURED}$, $IN^{1/2}$
FINE PEARLITE
COARSE PEARLITE
70°F
-100°F
-320°F
XBL 6910-5884

Fig. 31

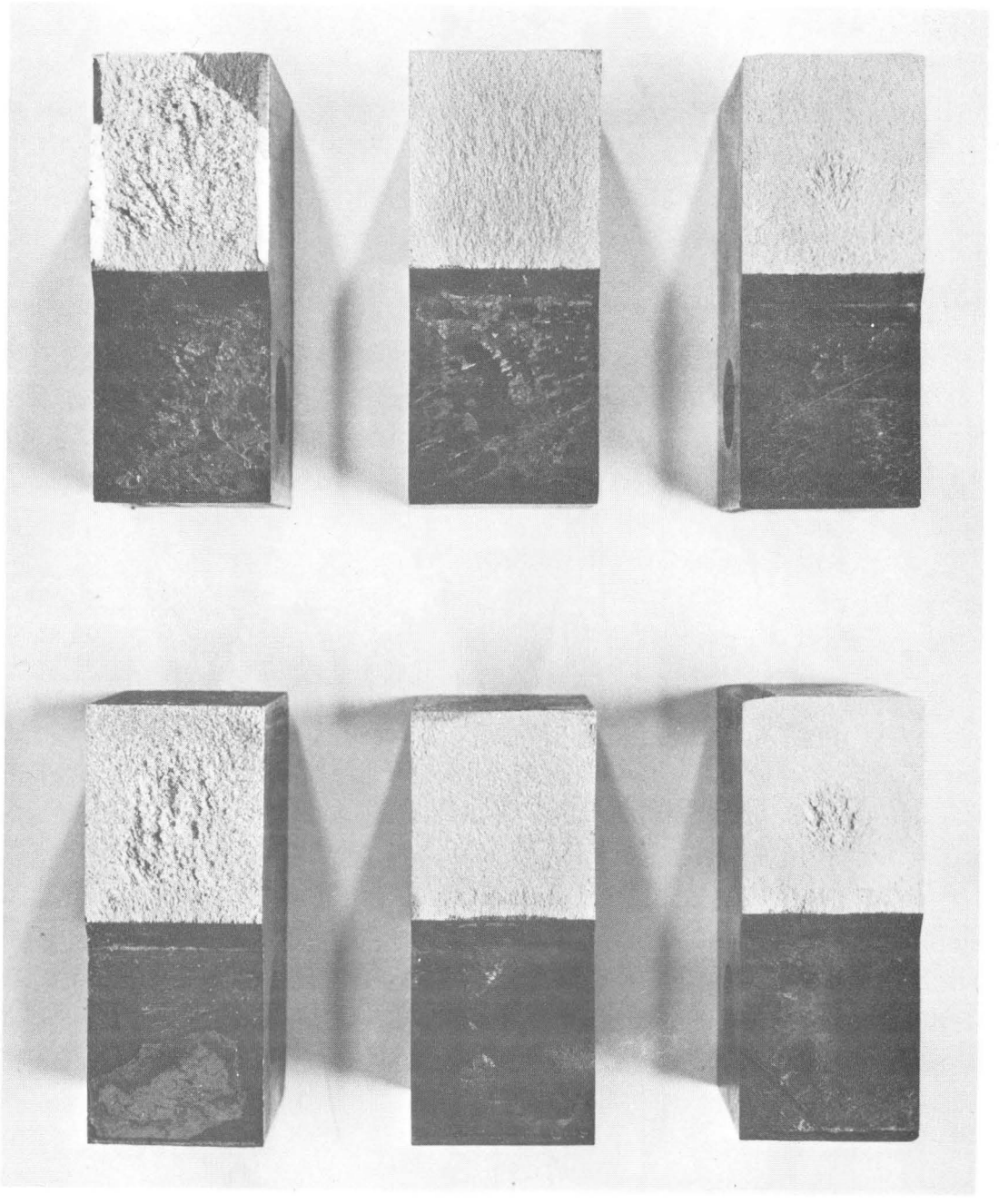

XBB 698-5050

Fig. 32

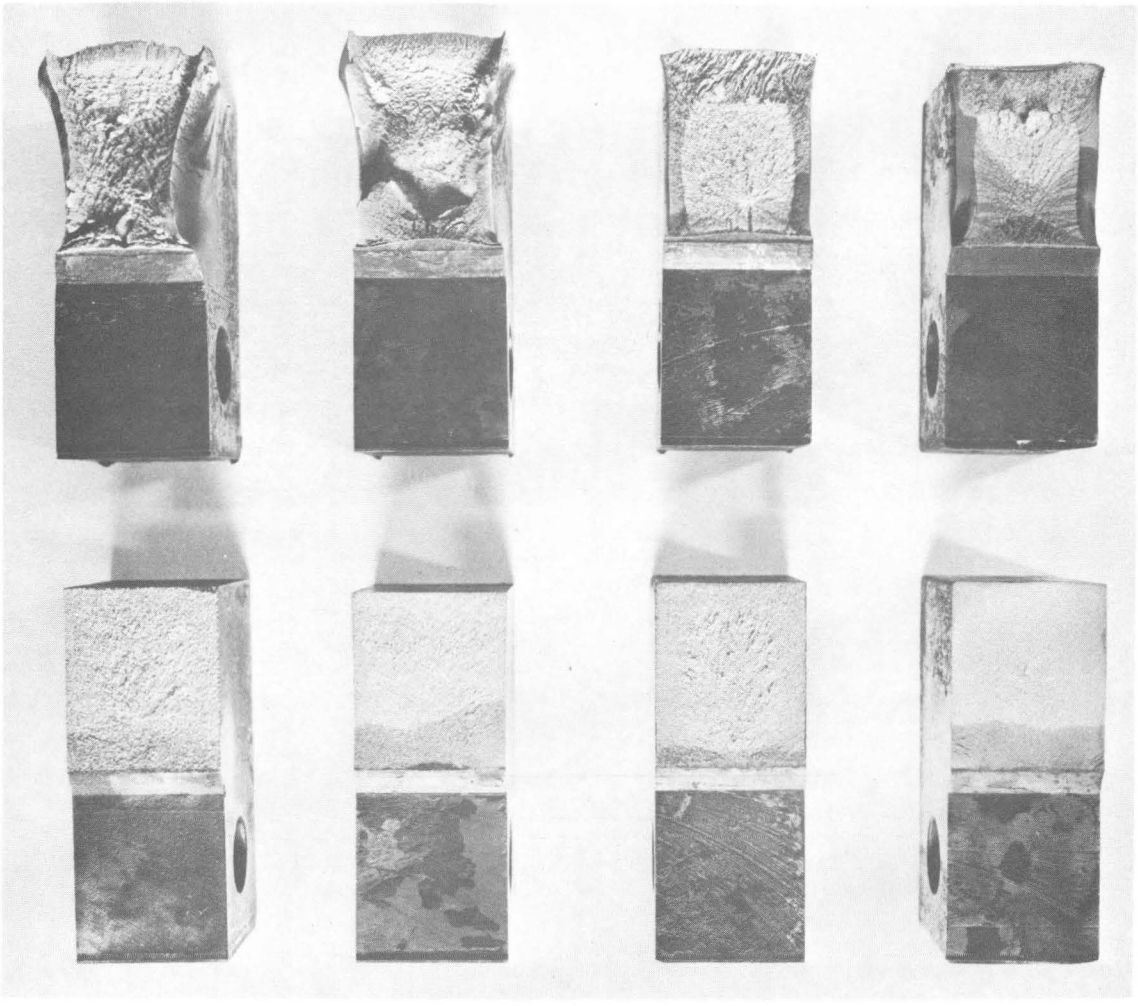

XBB 698-5051

Fig. 33

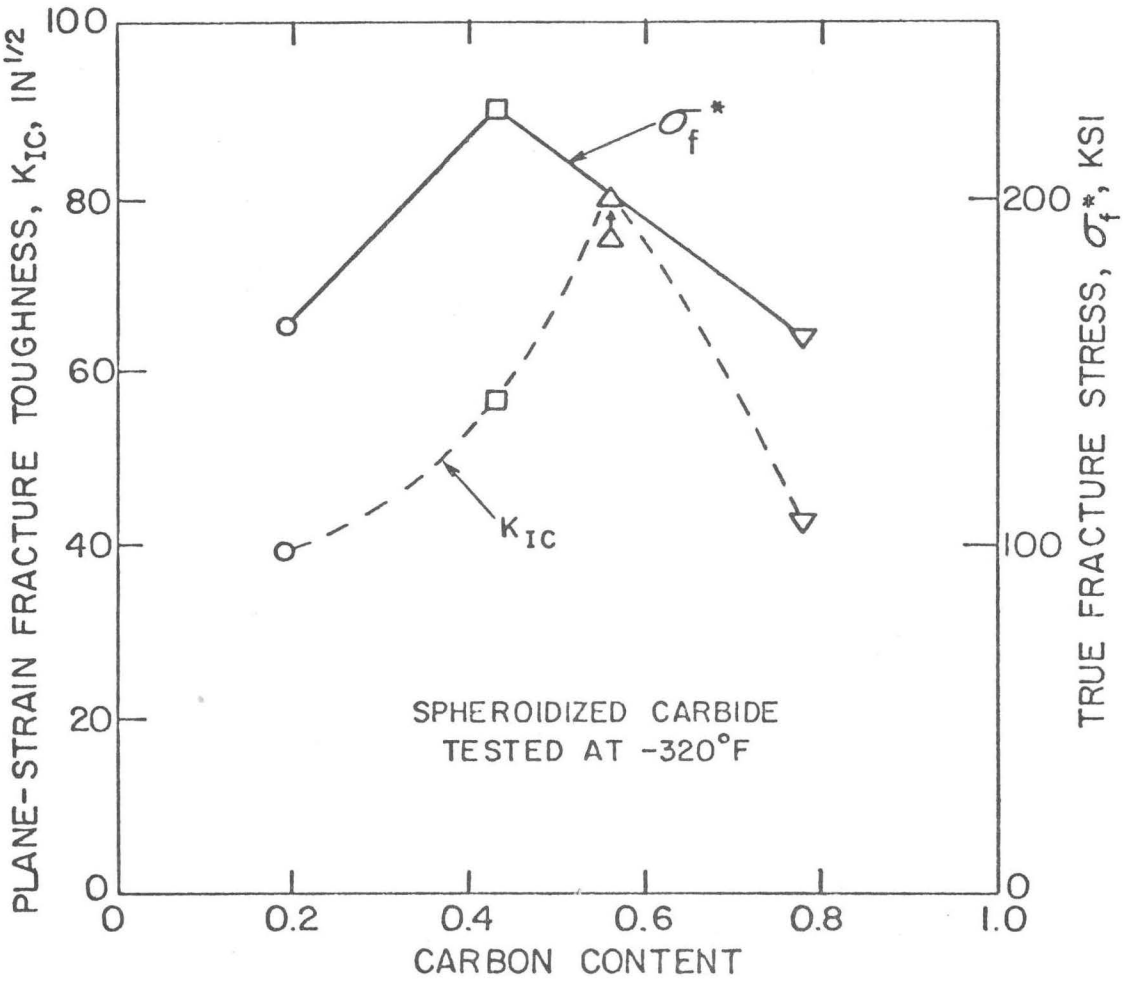

XBL 6910-5892

Fig. 34

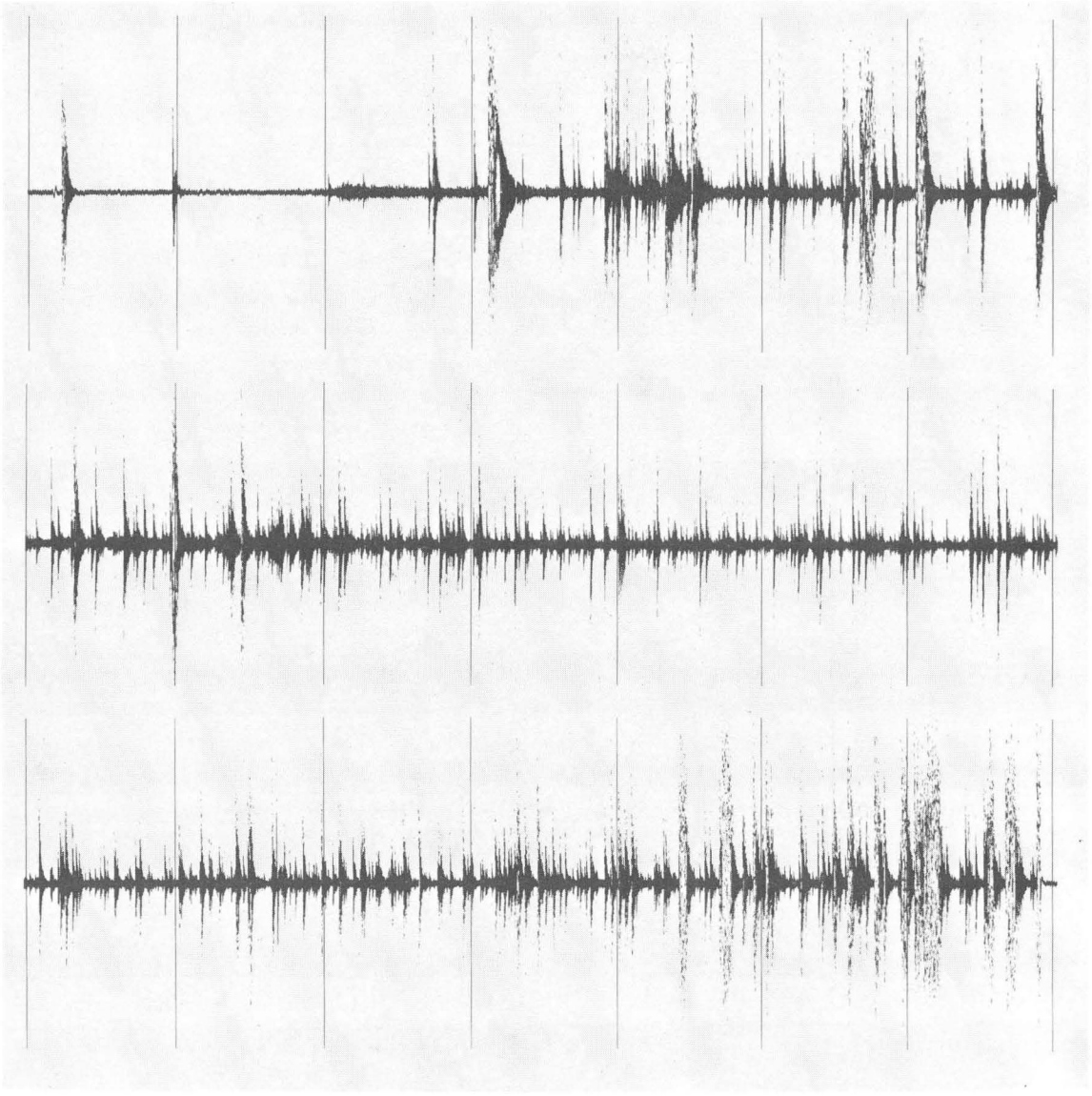

XBB 6910-6782

Fig. 35

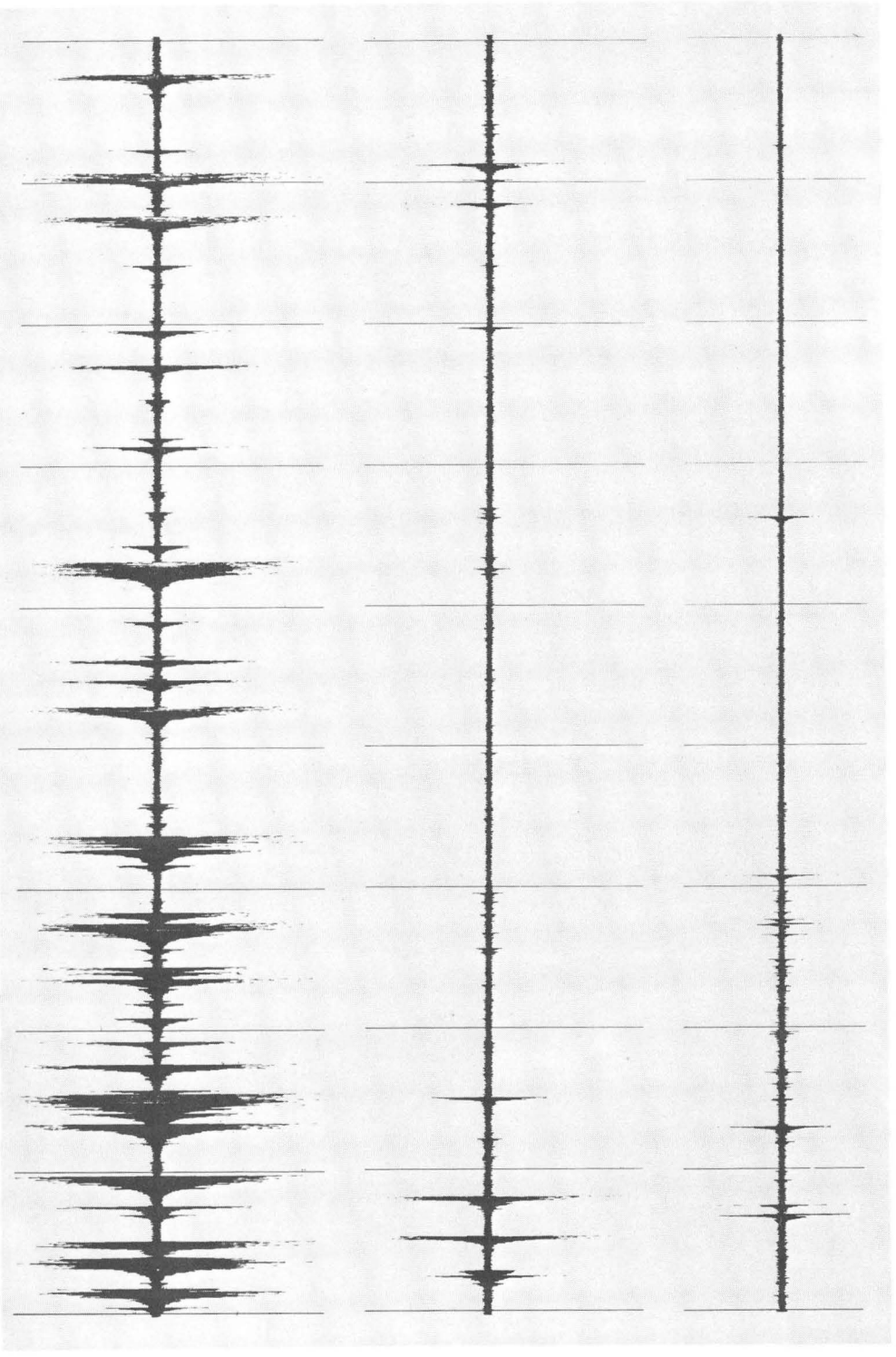

XBB 6910-6786

Fig. 36

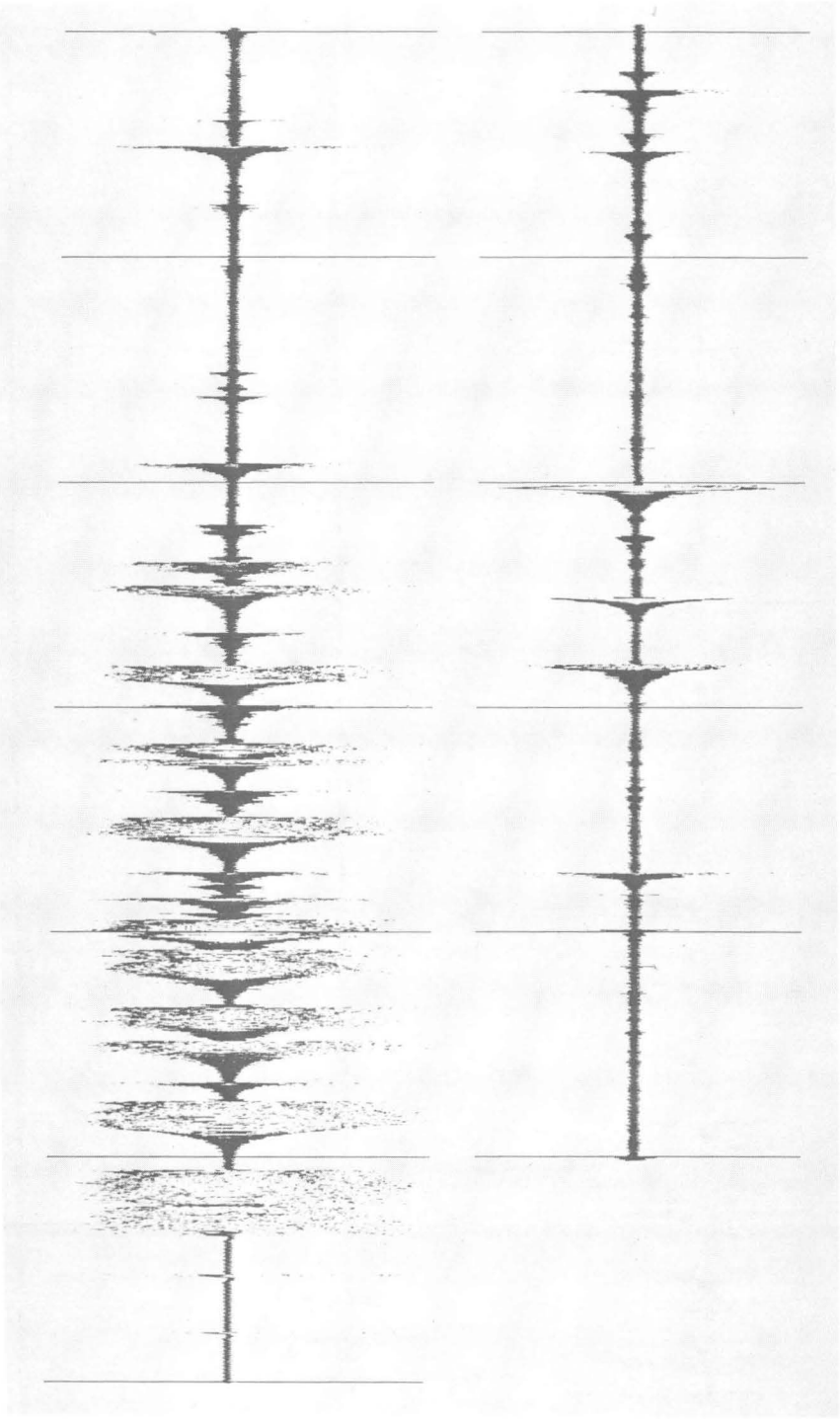

XBB 6910-6788

Fig. 37

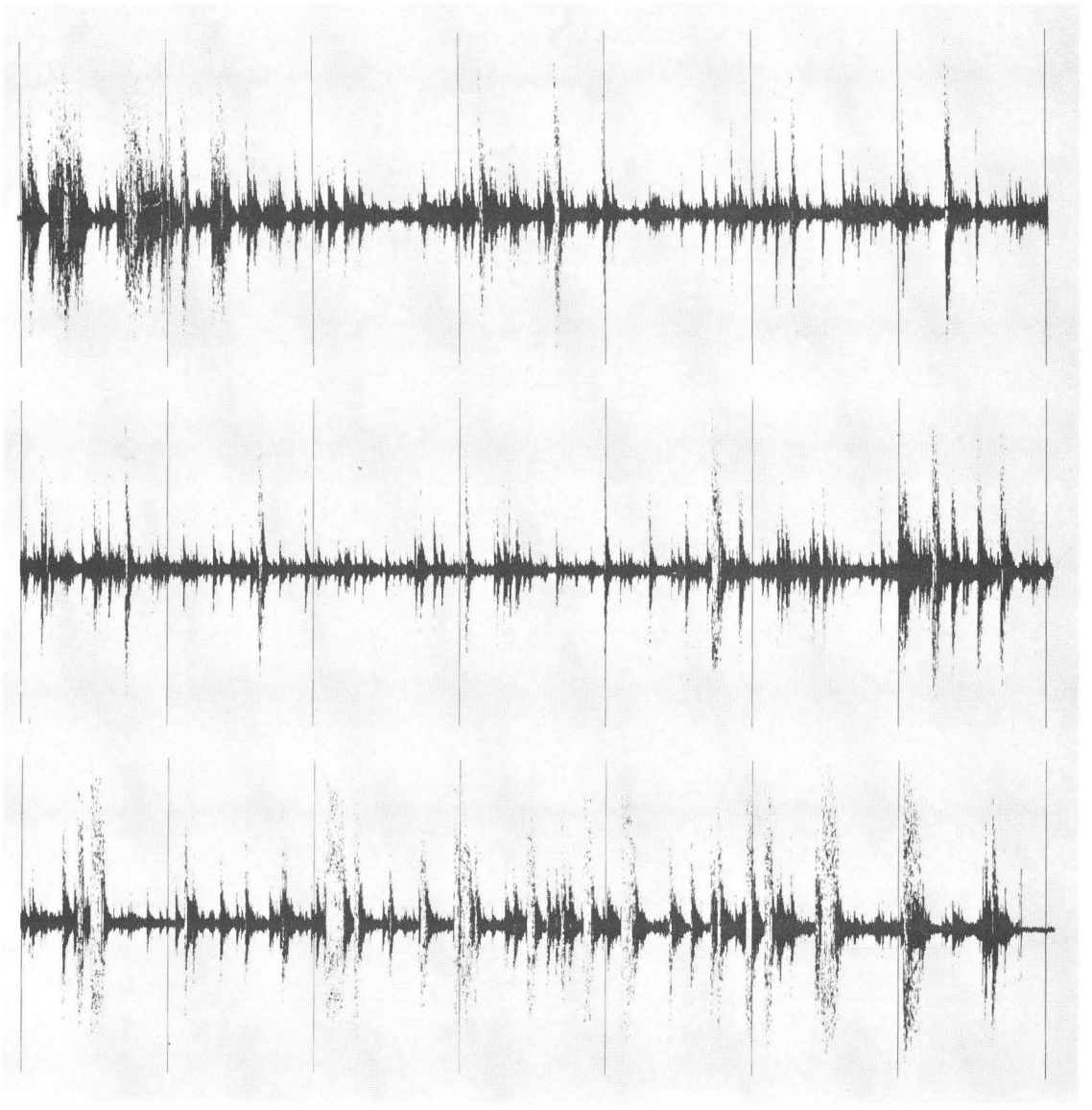

XBB 6910-6781

Fig. 38

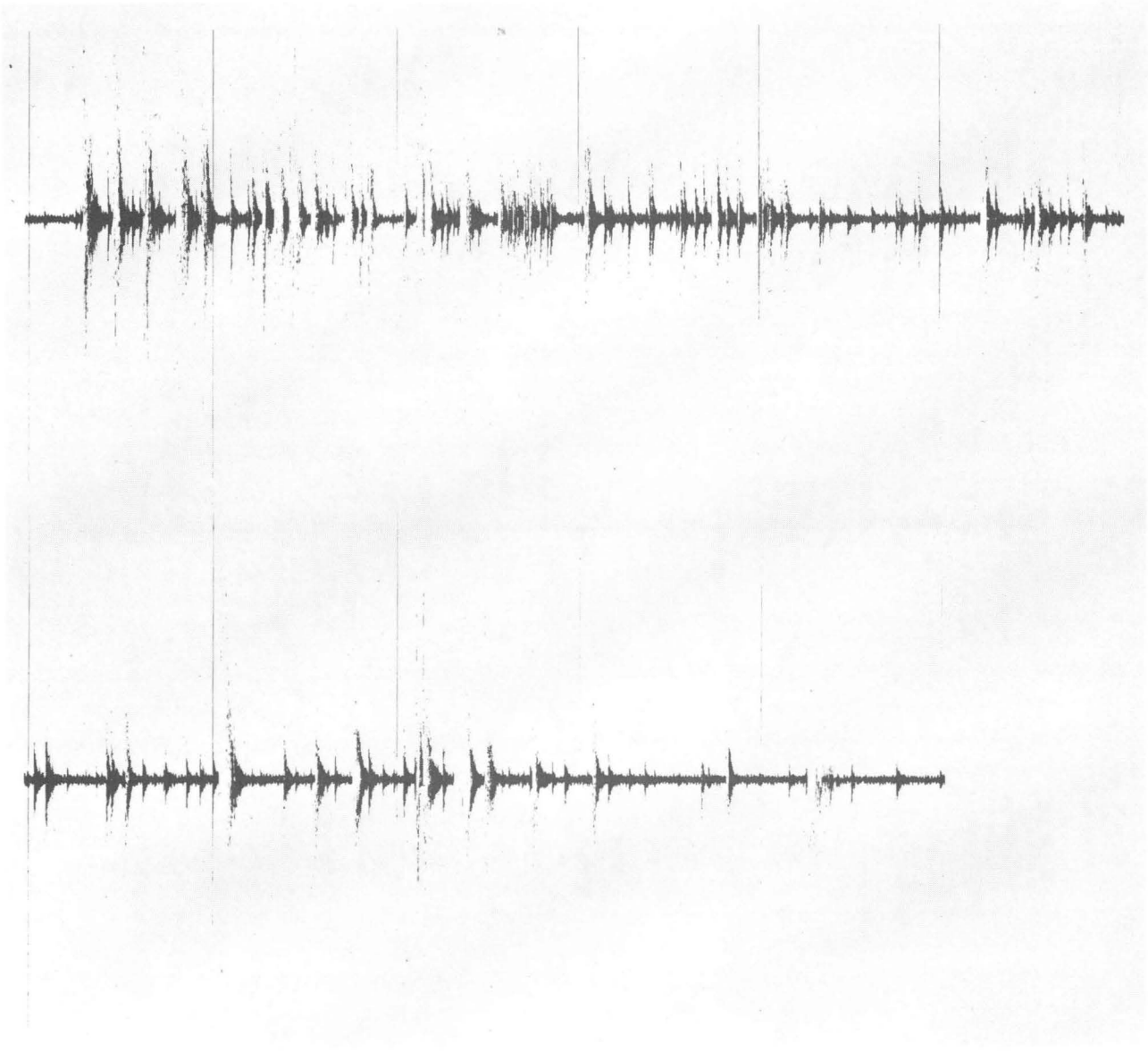

XBB 6910-6783

Fig. 39

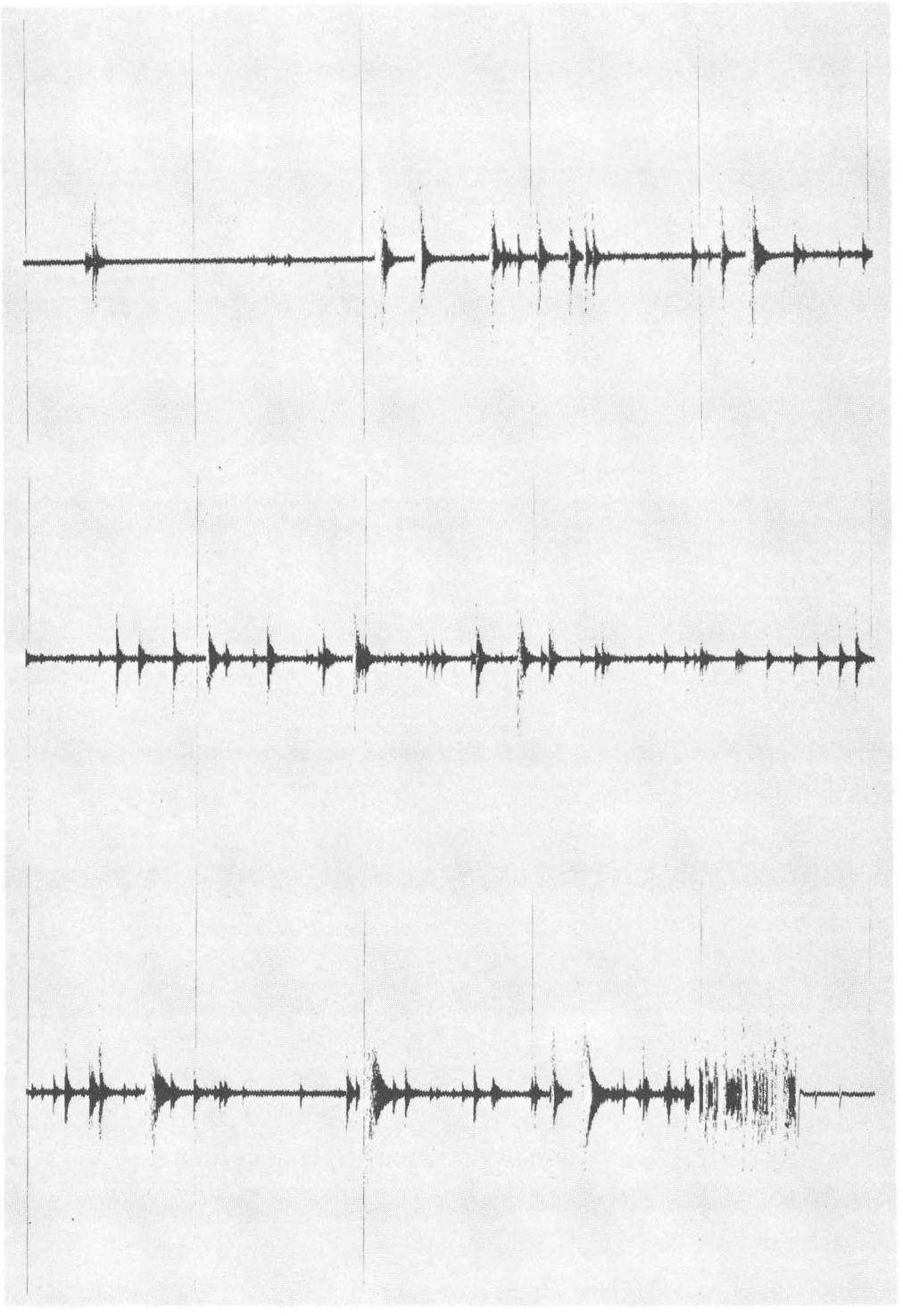

XBB 6910-6785

Fig. 40

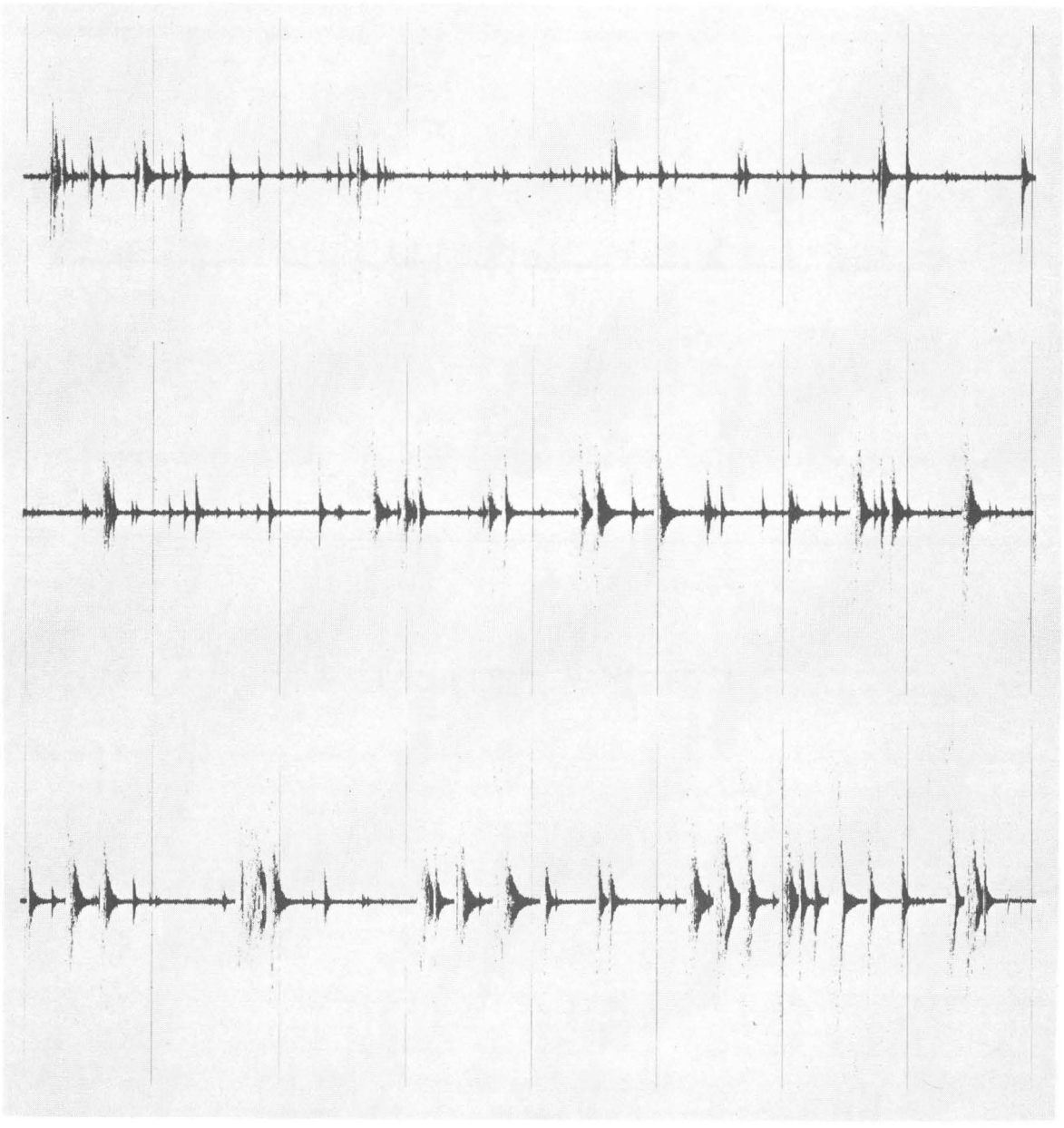

XBB 6910-6784

Fig. 41

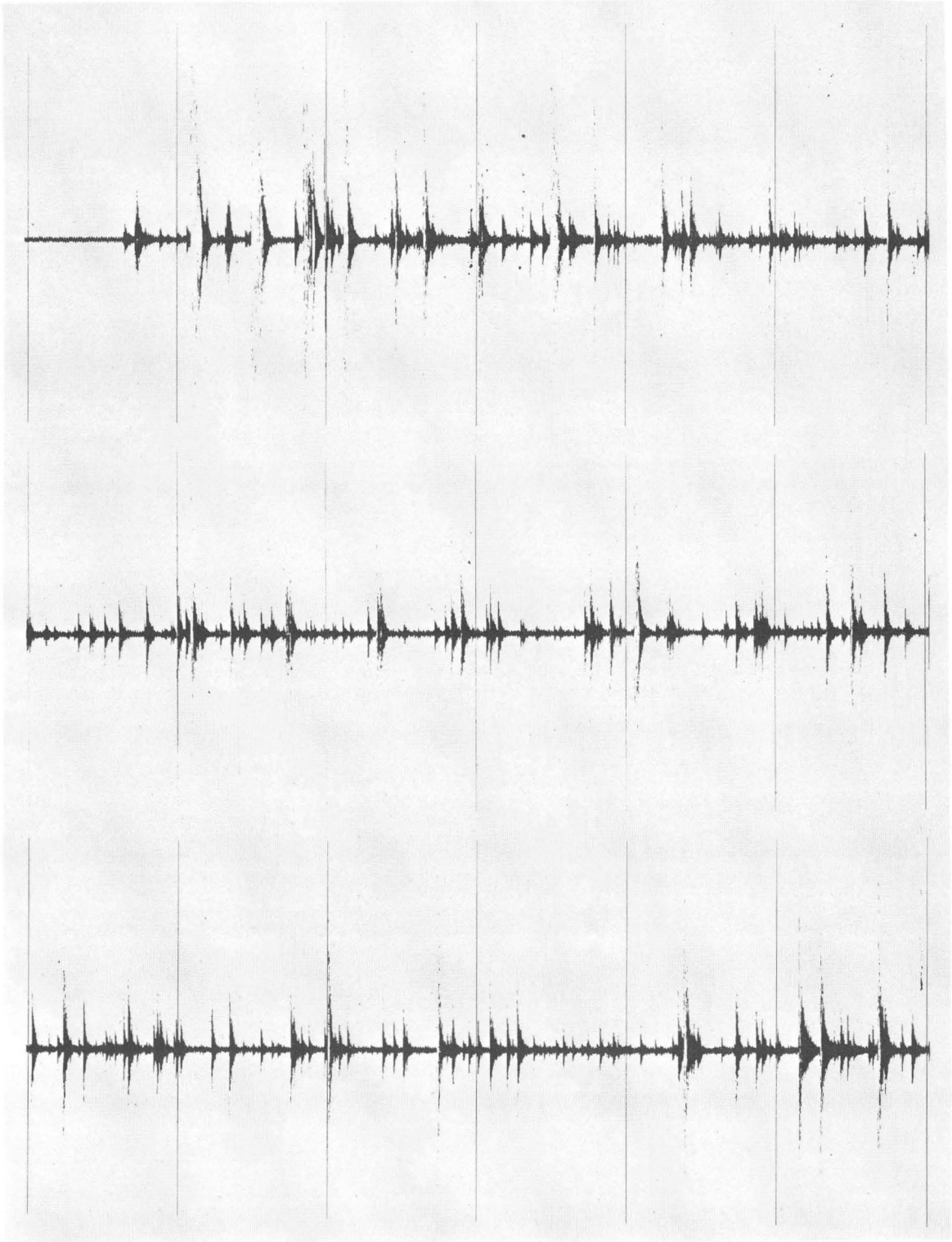

XBB 6910-6787

Fig. 42

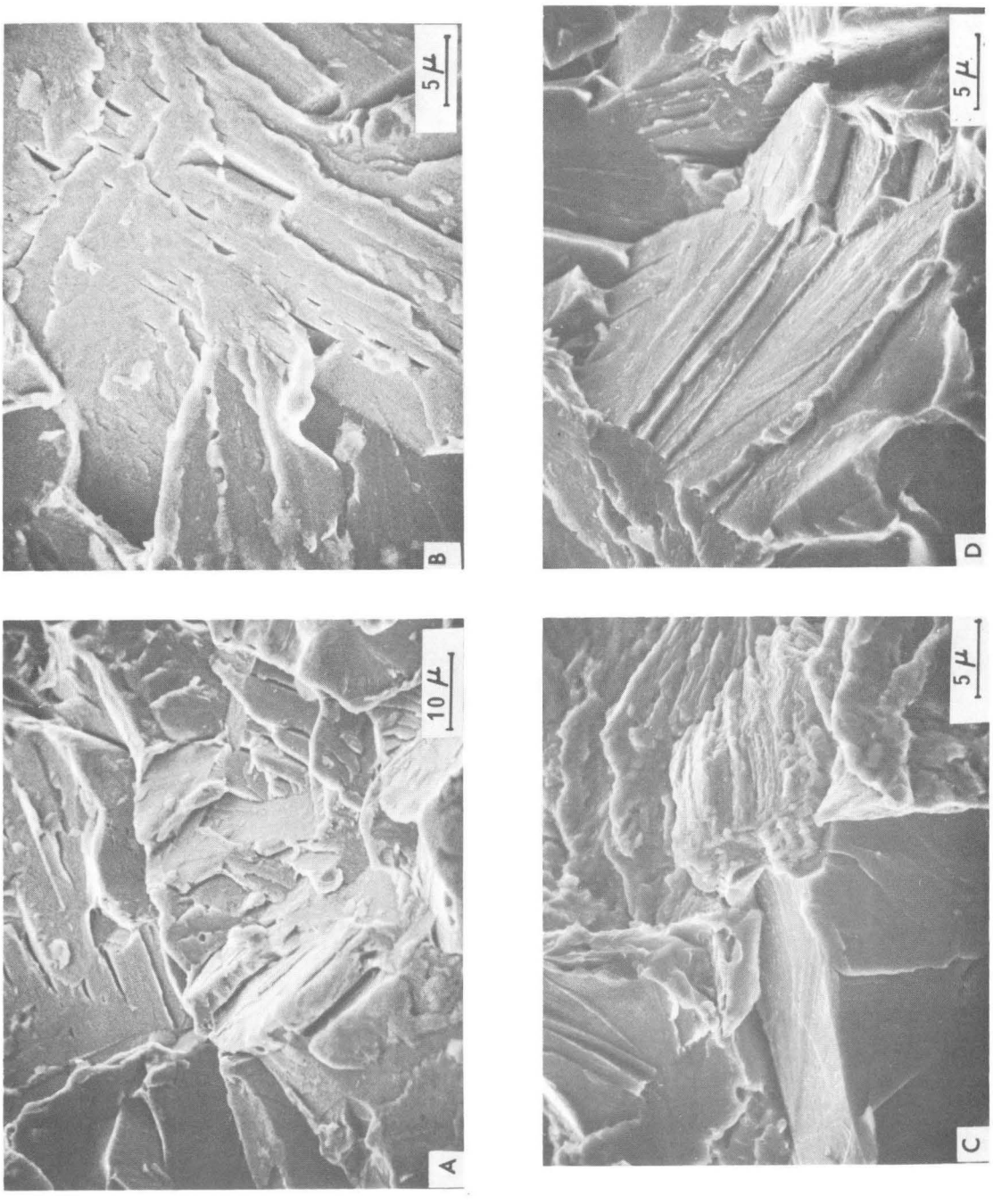

XBB 699-6312

Fig. 43

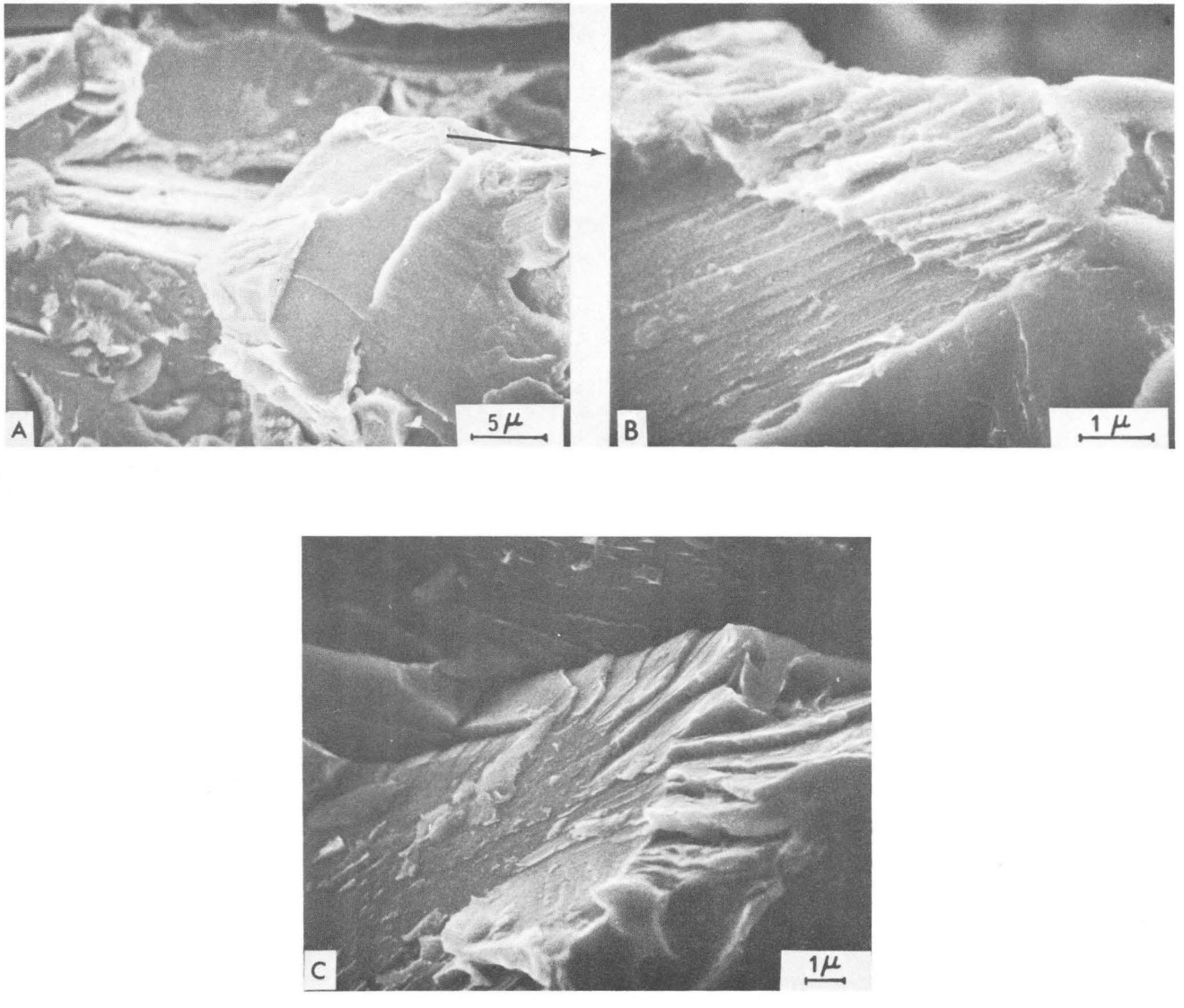

Fig. 44

XBB 699-6313

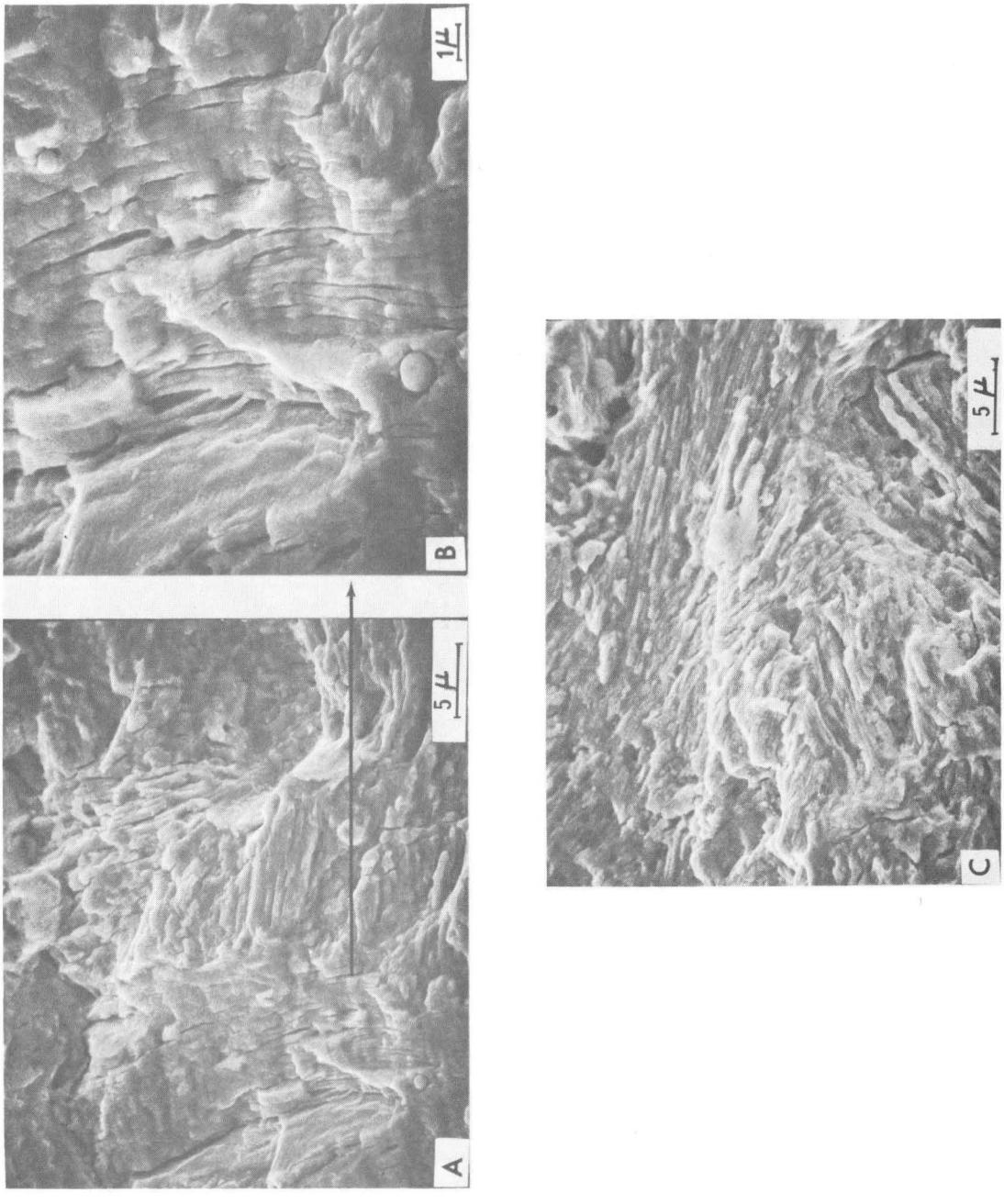

XBB 699-6314

Fig. 45

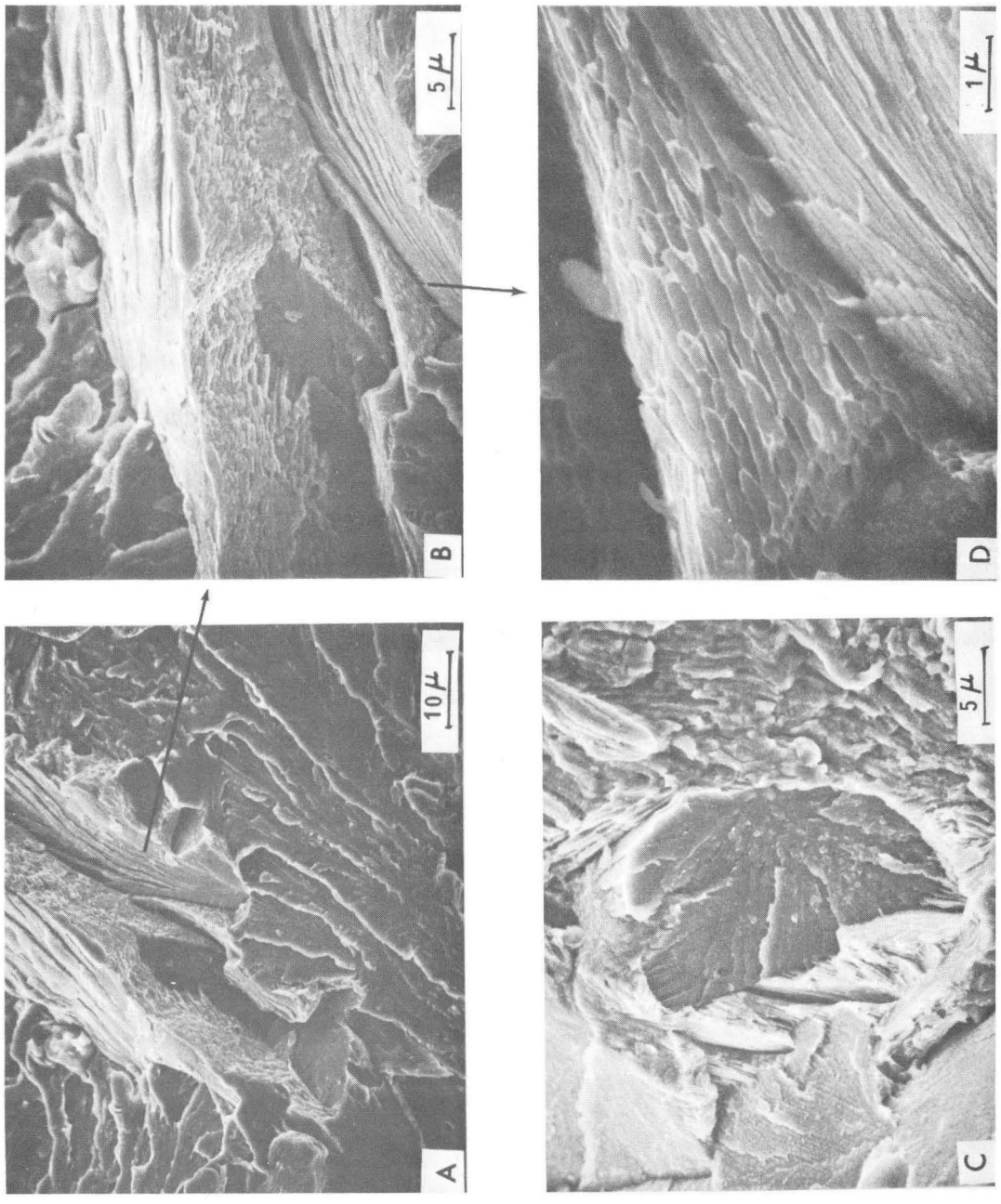

XBB 699-6308

Fig. 46

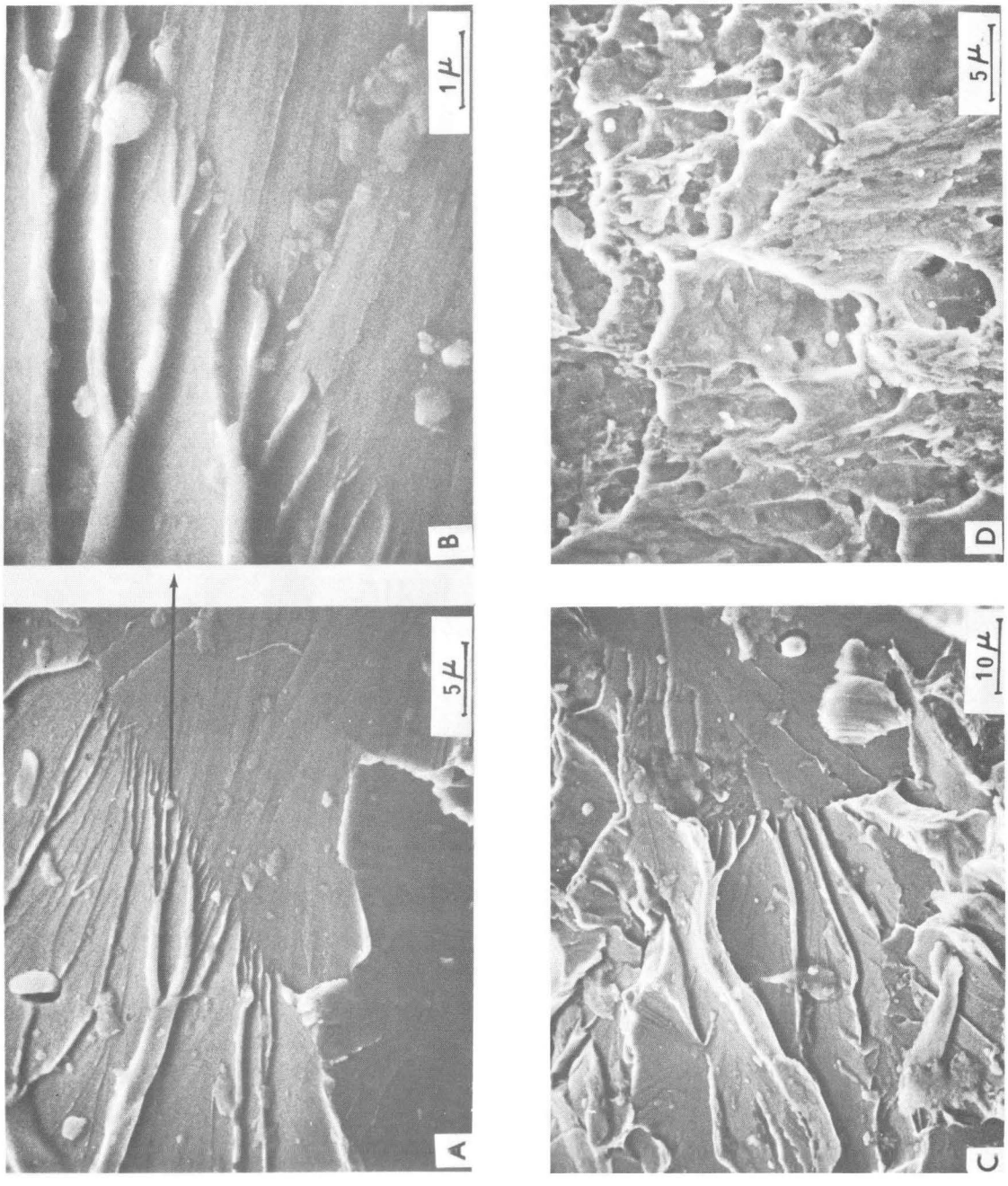

XBB 699-6309

Fig. 47

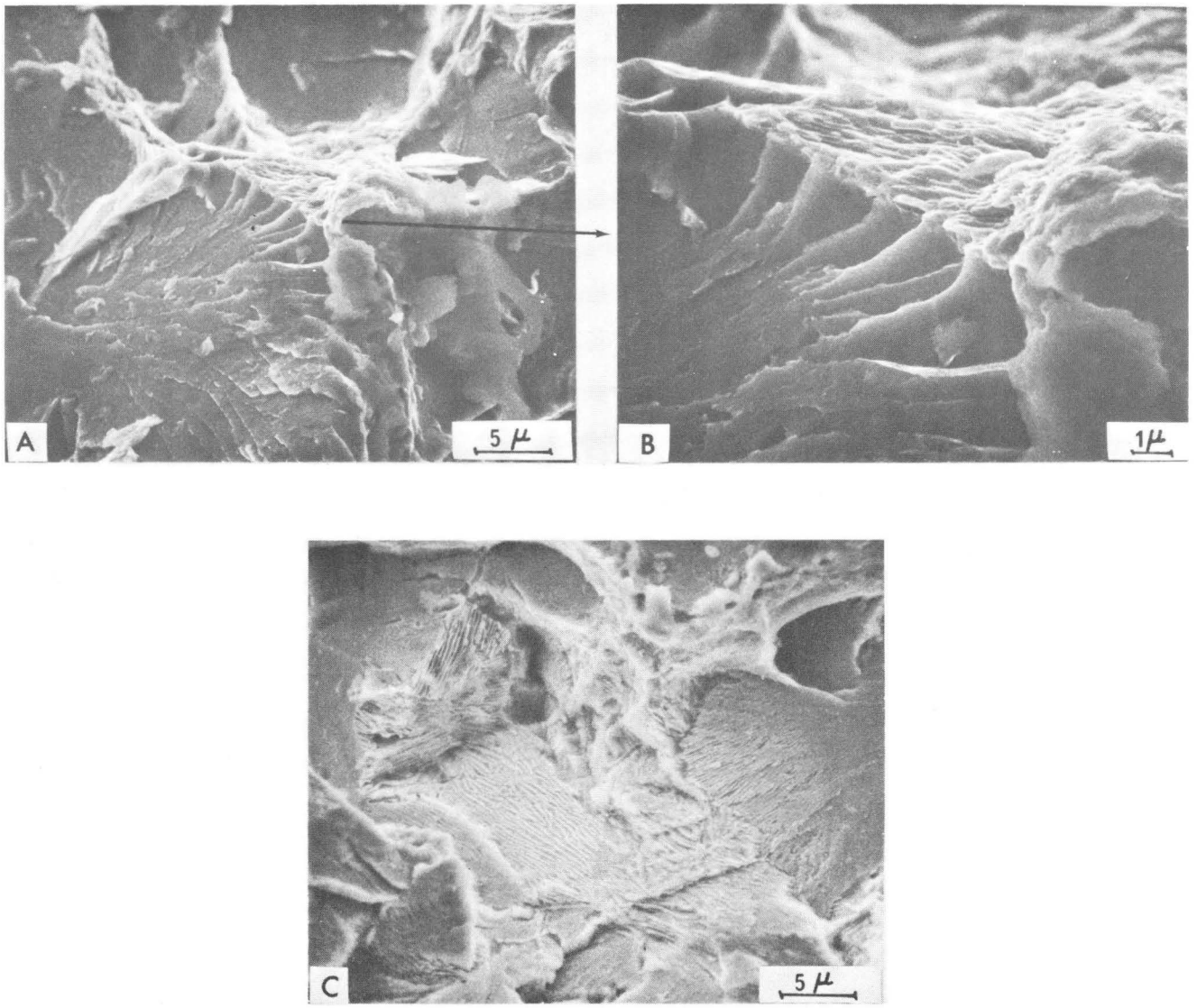

XBB 699-6310

Fig. 48

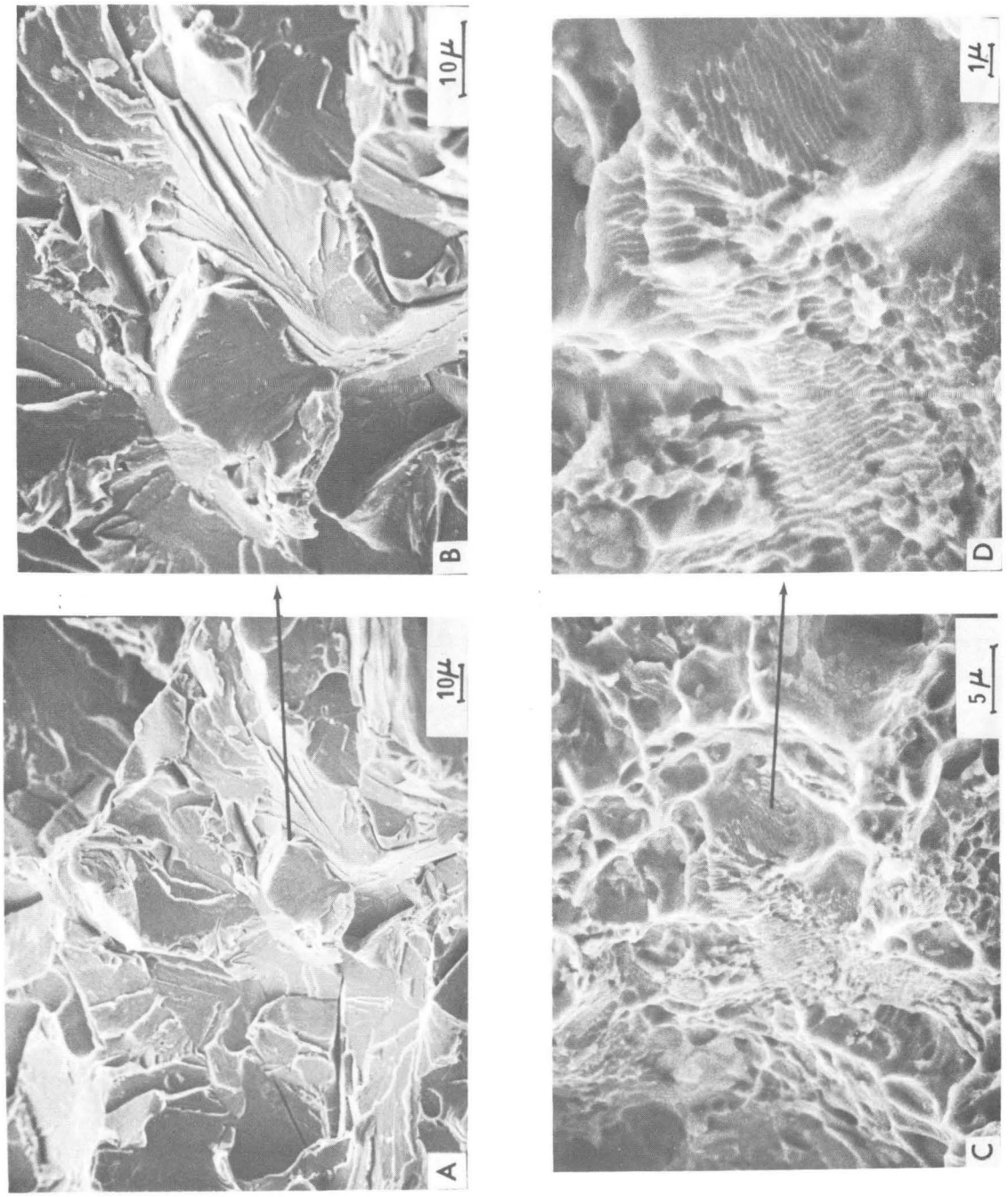

XBB 699-6311

Fig. 49

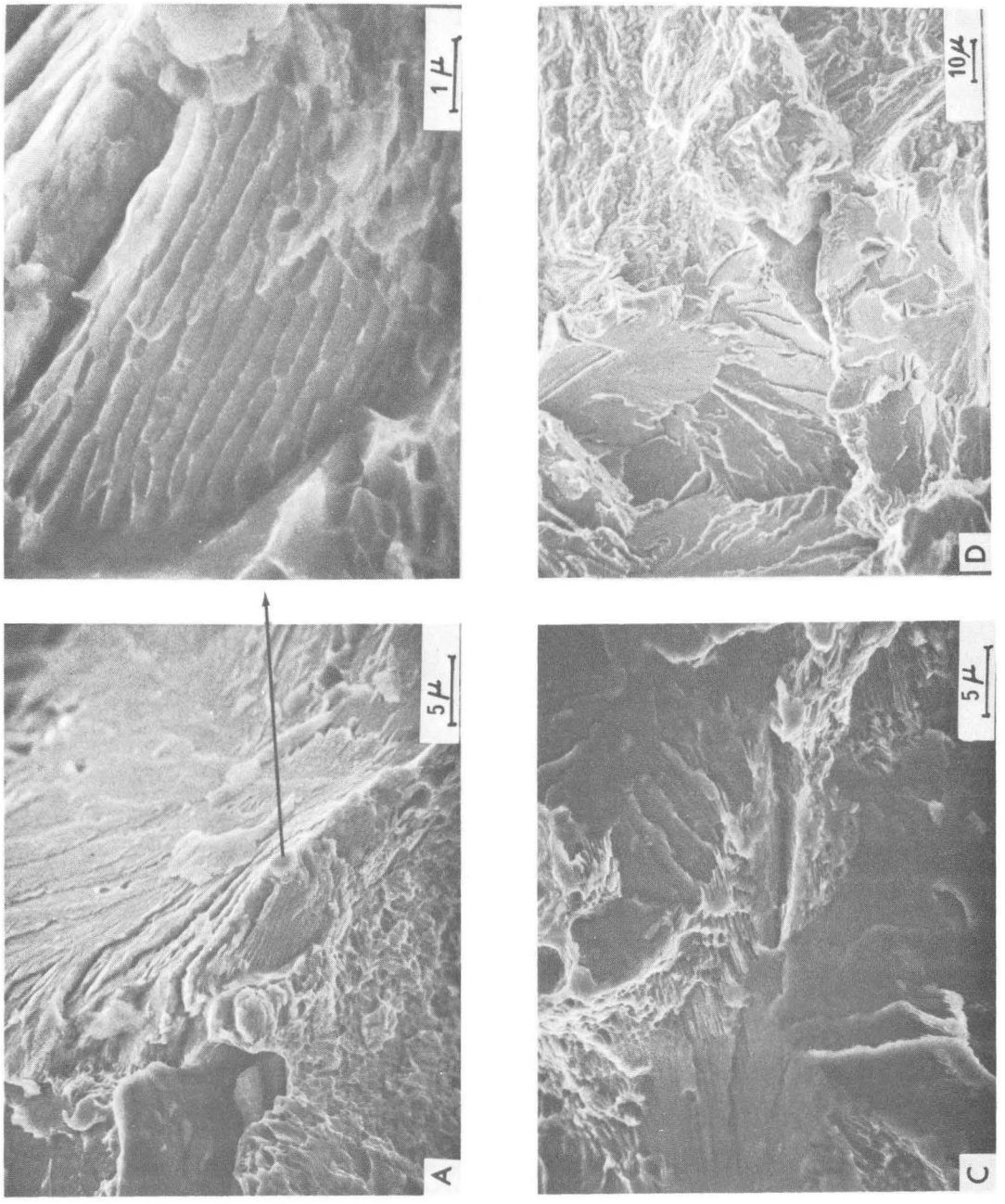

XBB 699-6304

Fig. 50

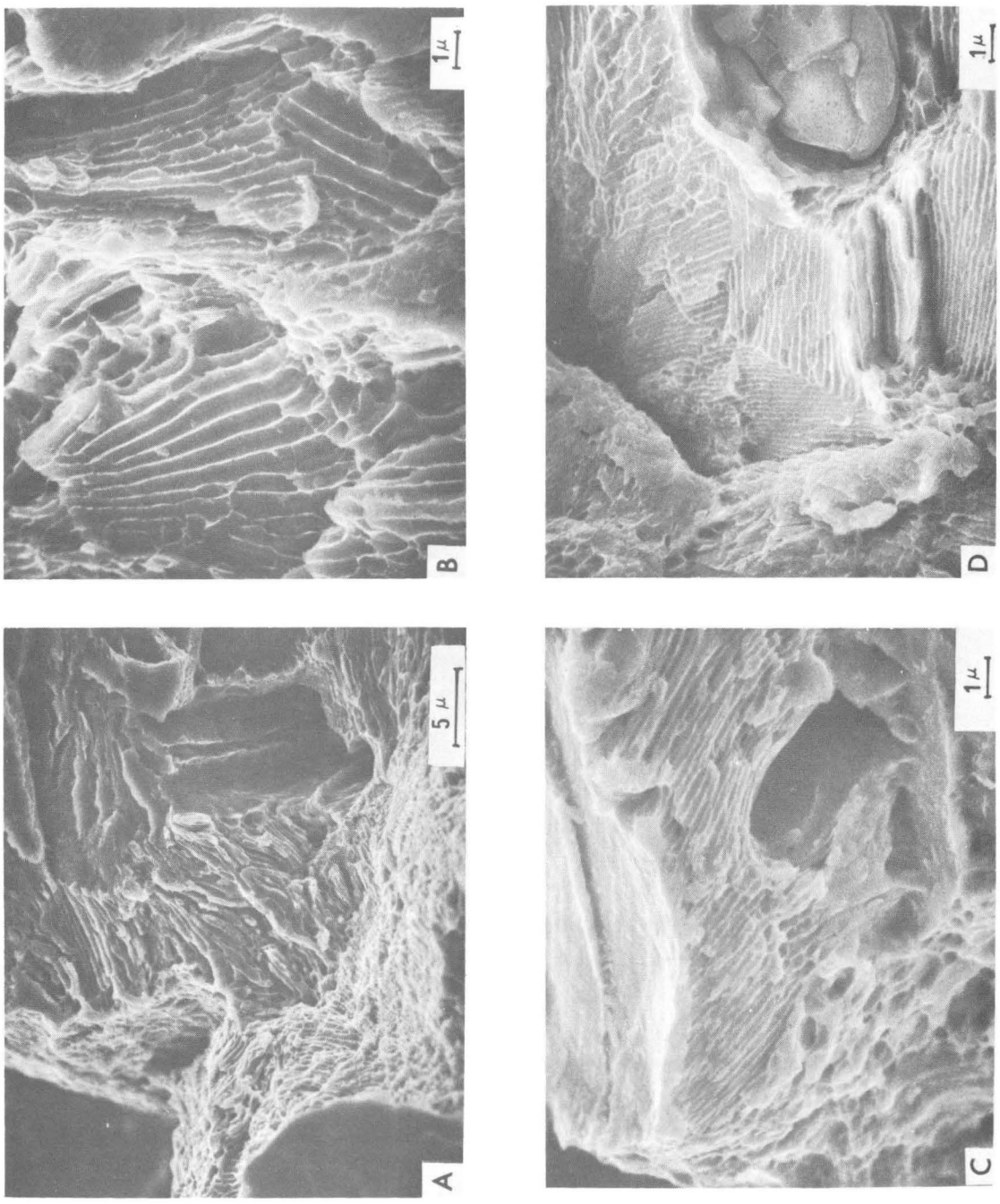

XBB 699-6306

Fig. 51

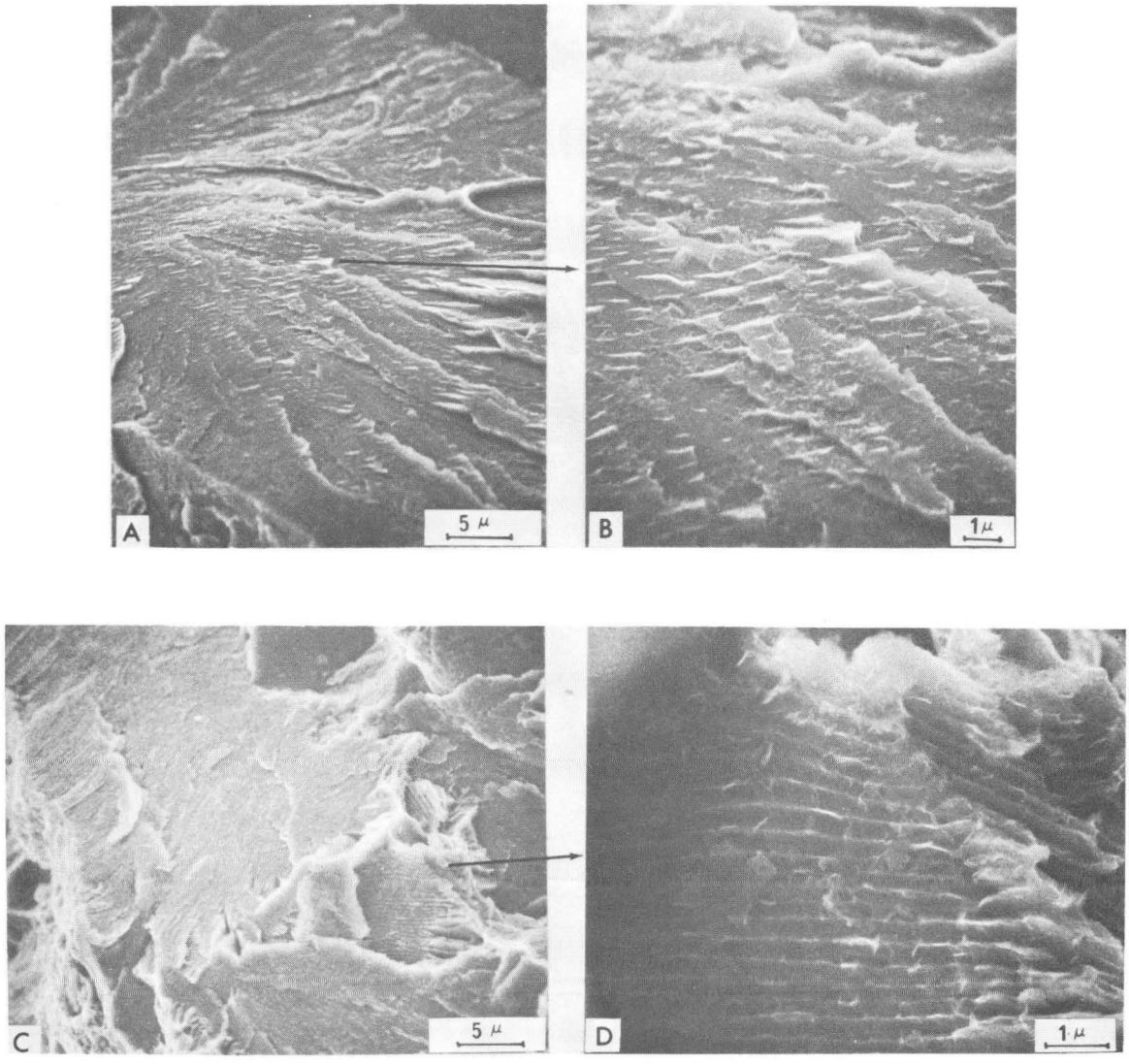

XBB 699-6315

Fig. 52

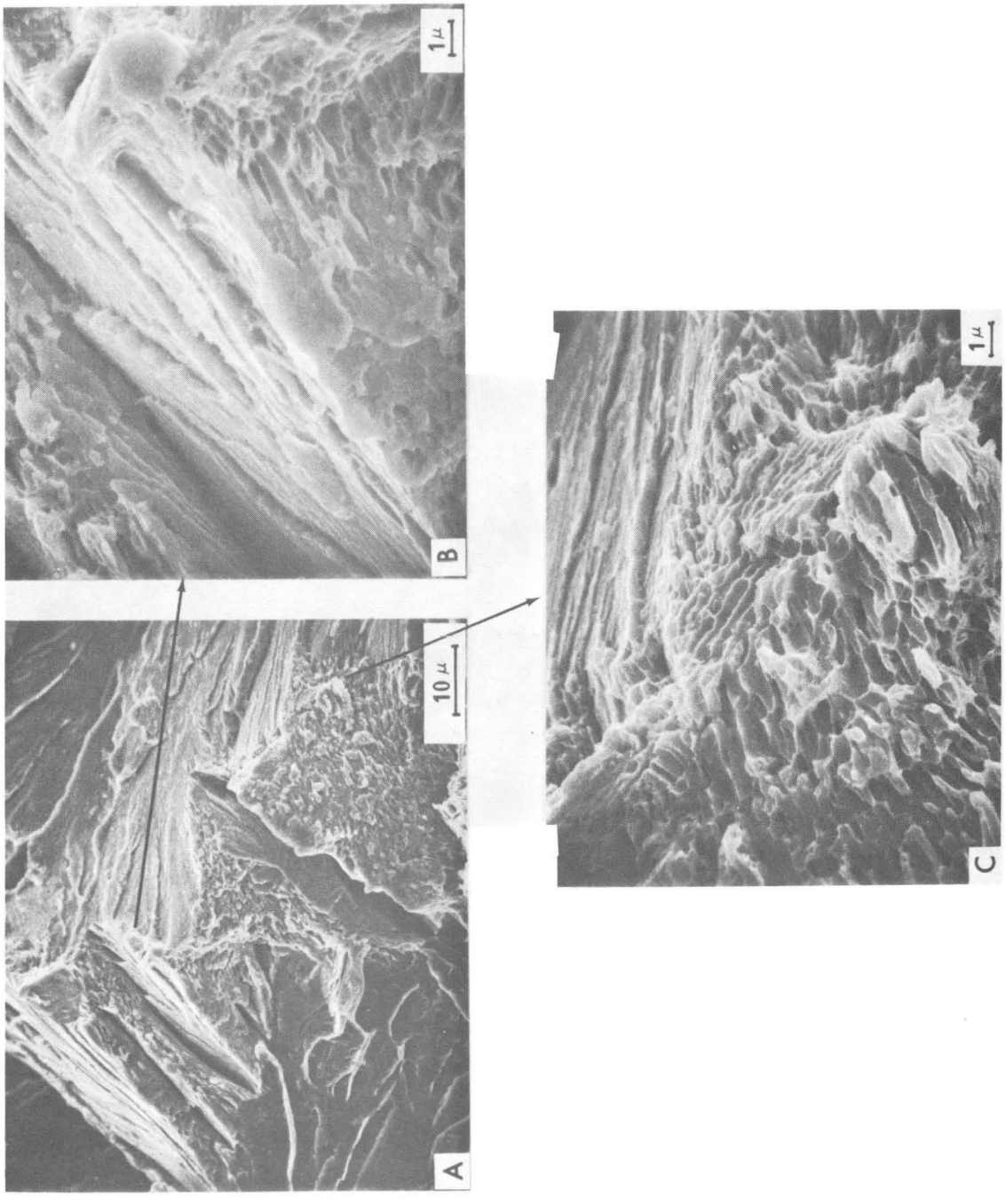

XBB 699-6307

Fig. 53

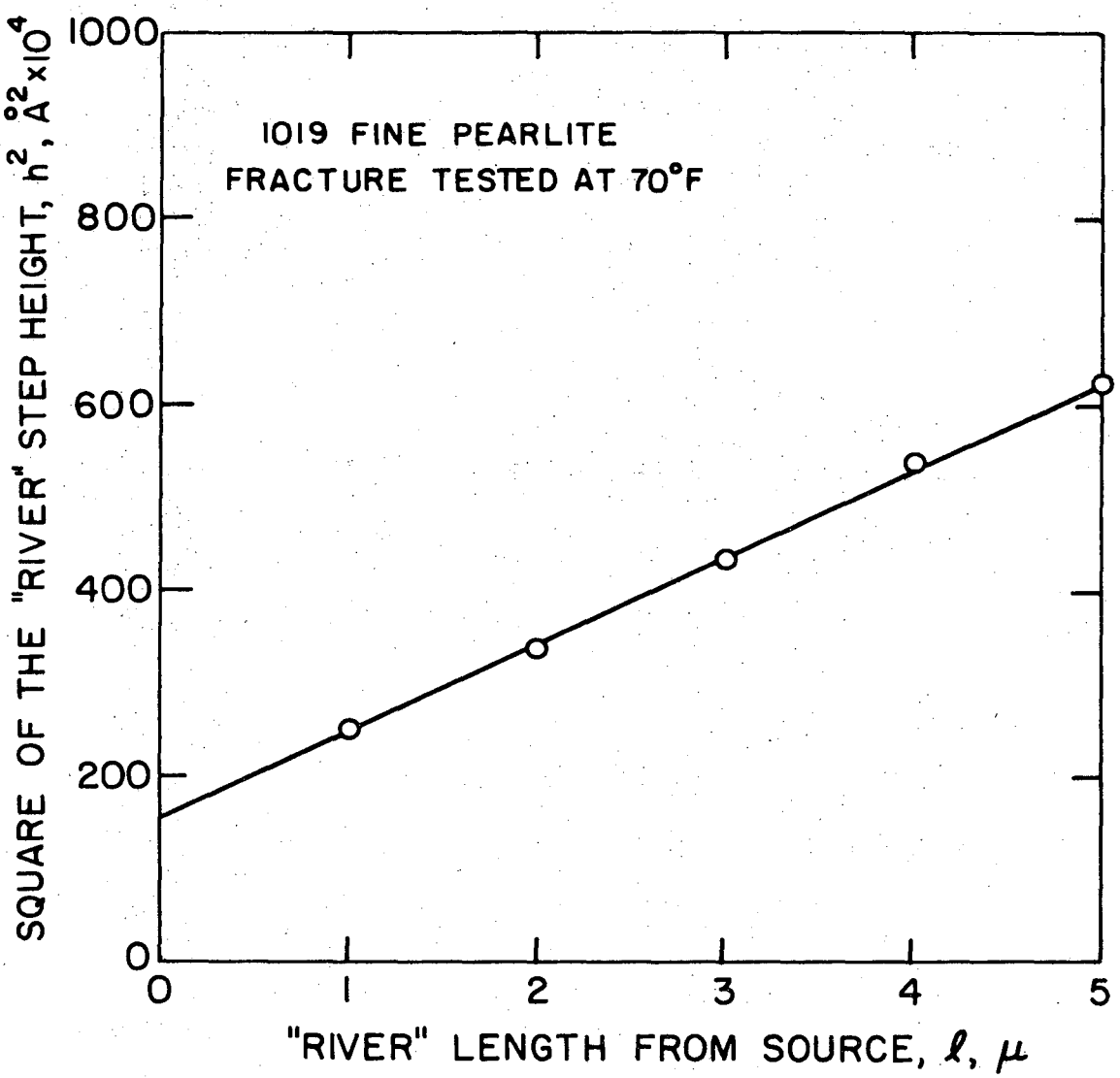

XBL 6910-5893

Fig. 54

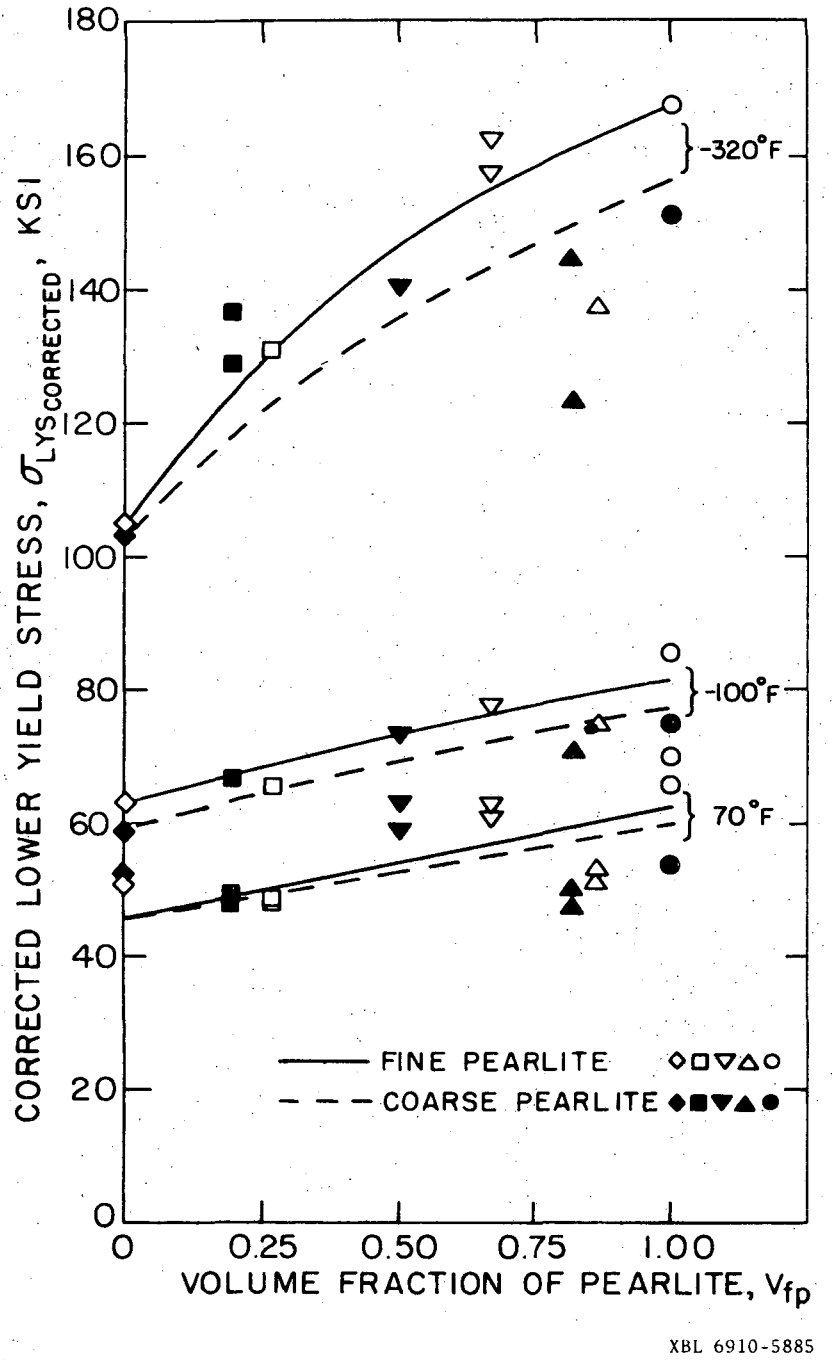
180
160
140
120
100
80
60
40
20
0
0
0.25
0.50
0.75
1.00
CORRECTED LOWER YIELD STRESS, $\sigma_{LYS_{CORRECTED}}$, KSI
VOLUME FRACTION OF PEARLITE, V_{fp}
-320°F
-100°F
70°F
FINE PEARLITE
COARSE PEARLITE
XBL 6910-5885

Fig. 55

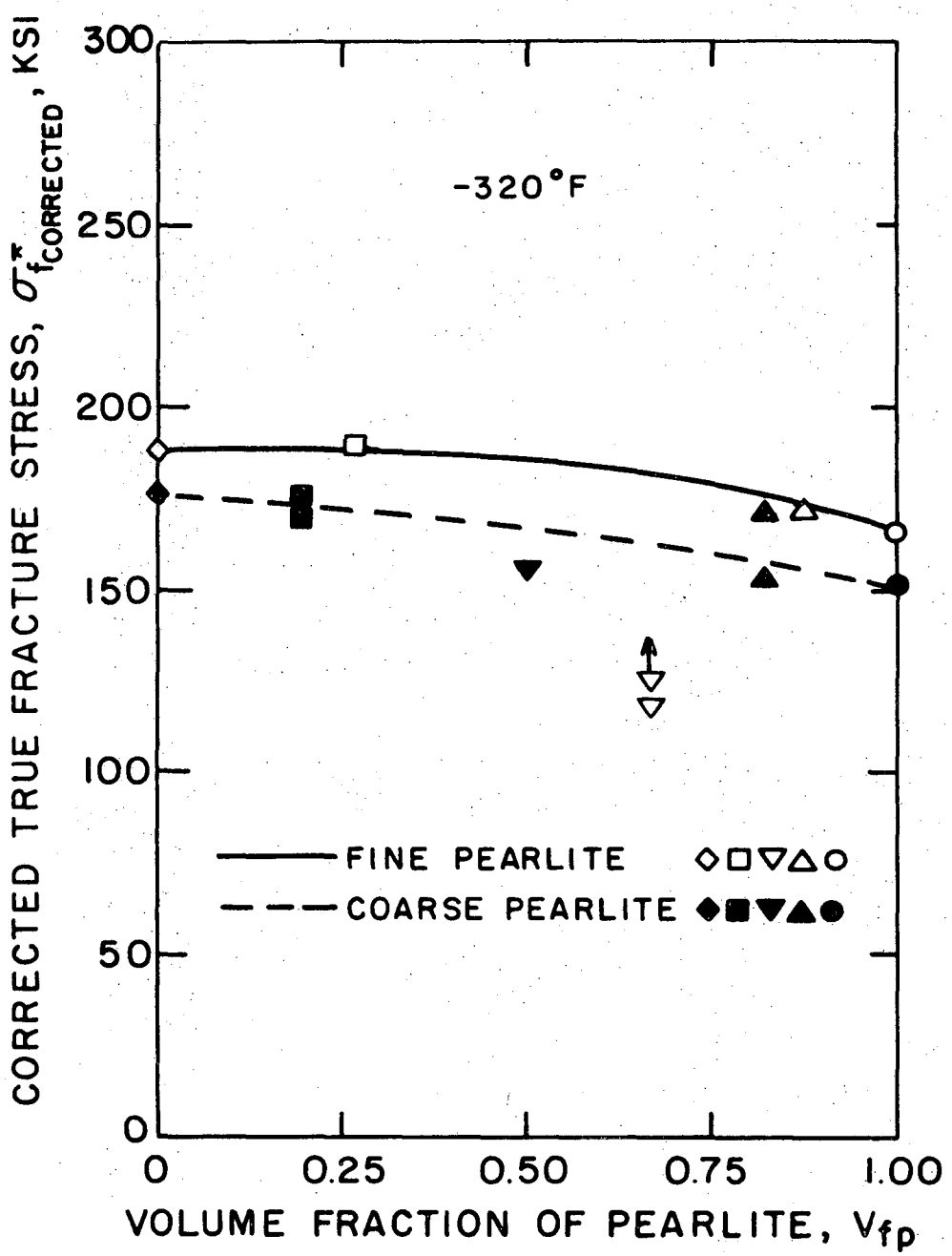

XBL 6910-5881

Fig. 56

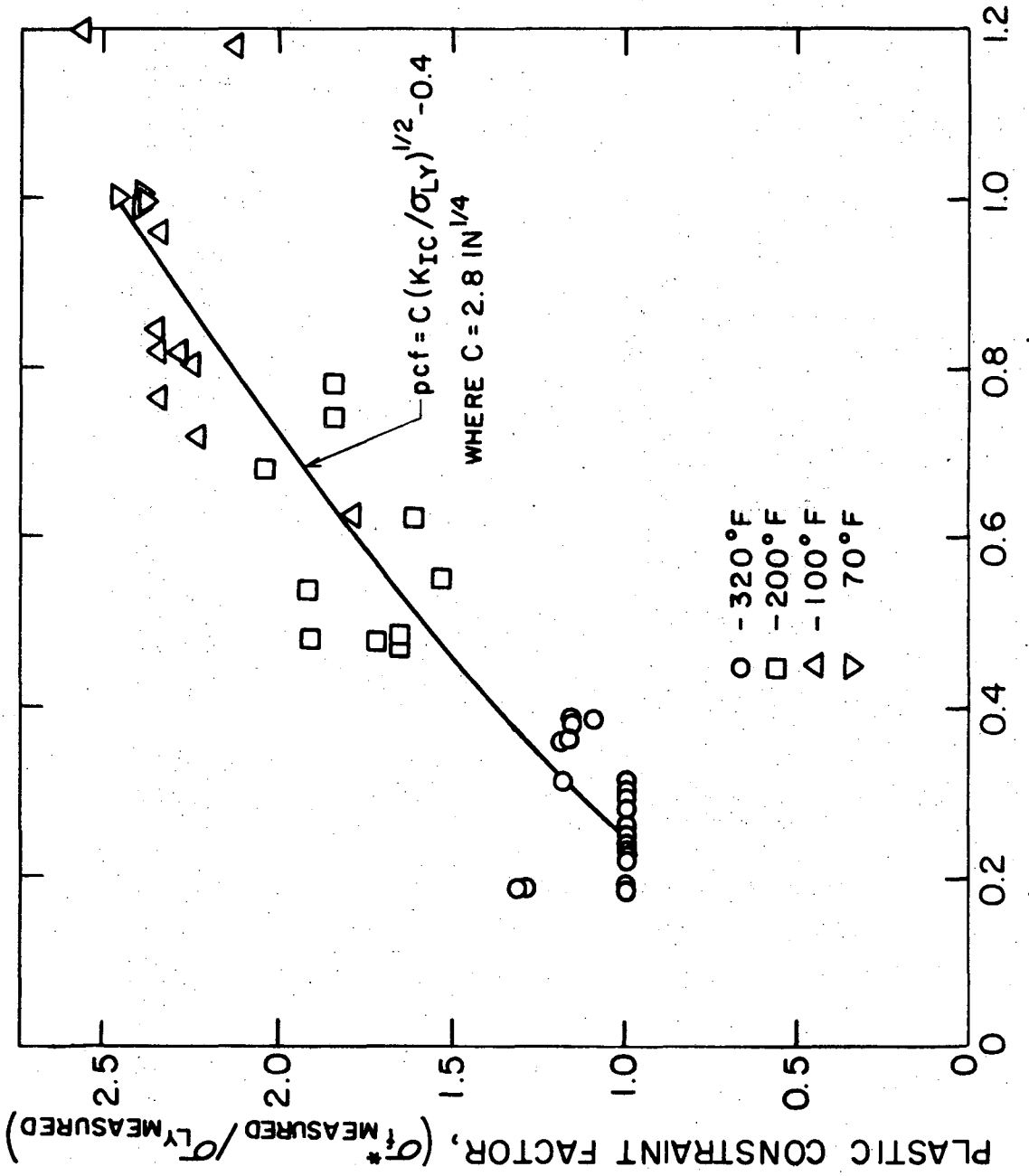

XBL 6911-6507

Fig. 57

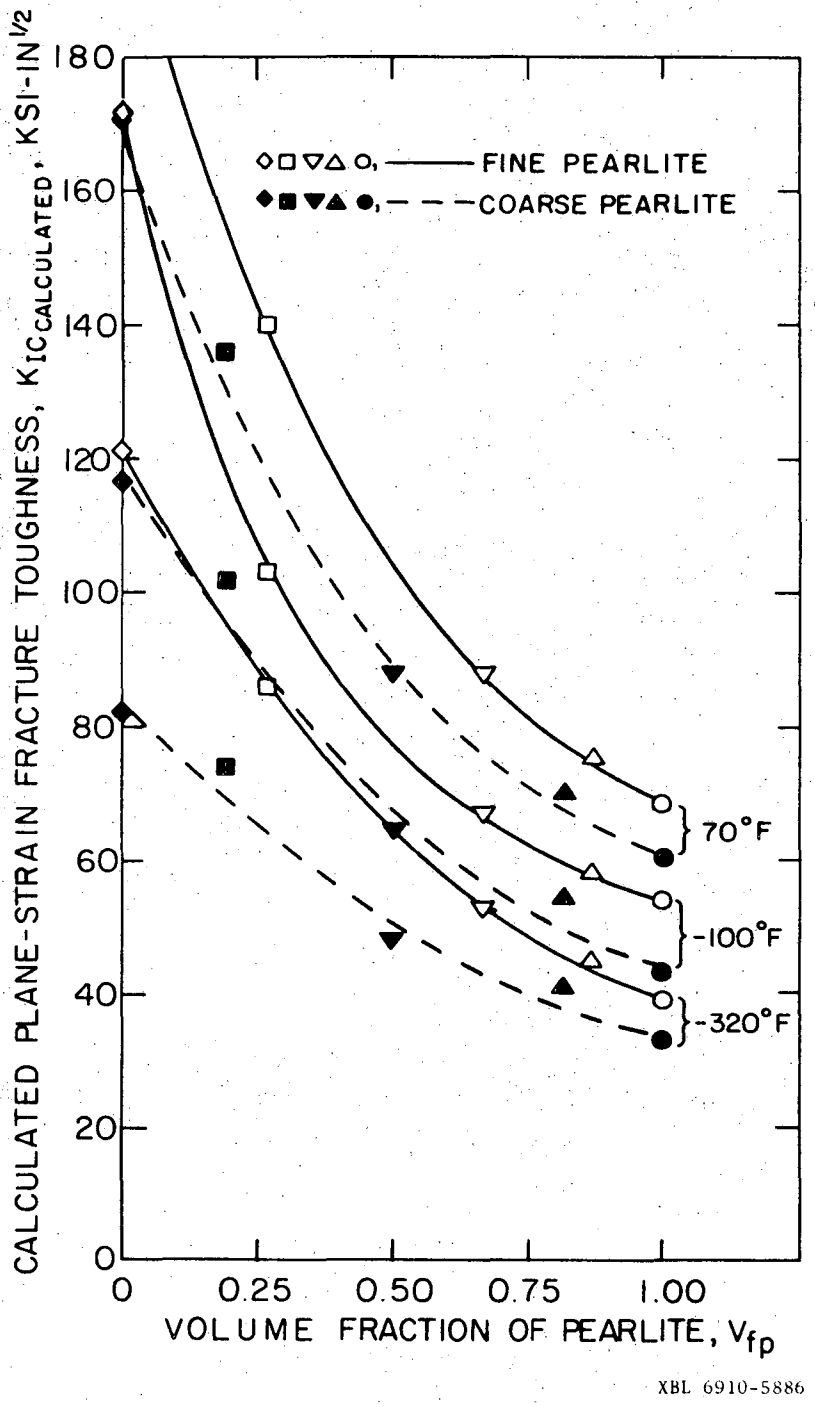
CALCULATED PLANE-STRAIN FRACTURE TOUGHNESS, $K_{IC_{CALCULATED}}$, KSI-IN$^{1/2}$
180
160
140
120
100
80
60
40
20
0
0
0.25
0.50
0.75
1.00
VOLUME FRACTION OF PEARLITE, V_{fp}
FINE PEARLITE
COARSE PEARLITE
70°F
-100°F
-320°F
XBL 6910-5886

Fig. 58

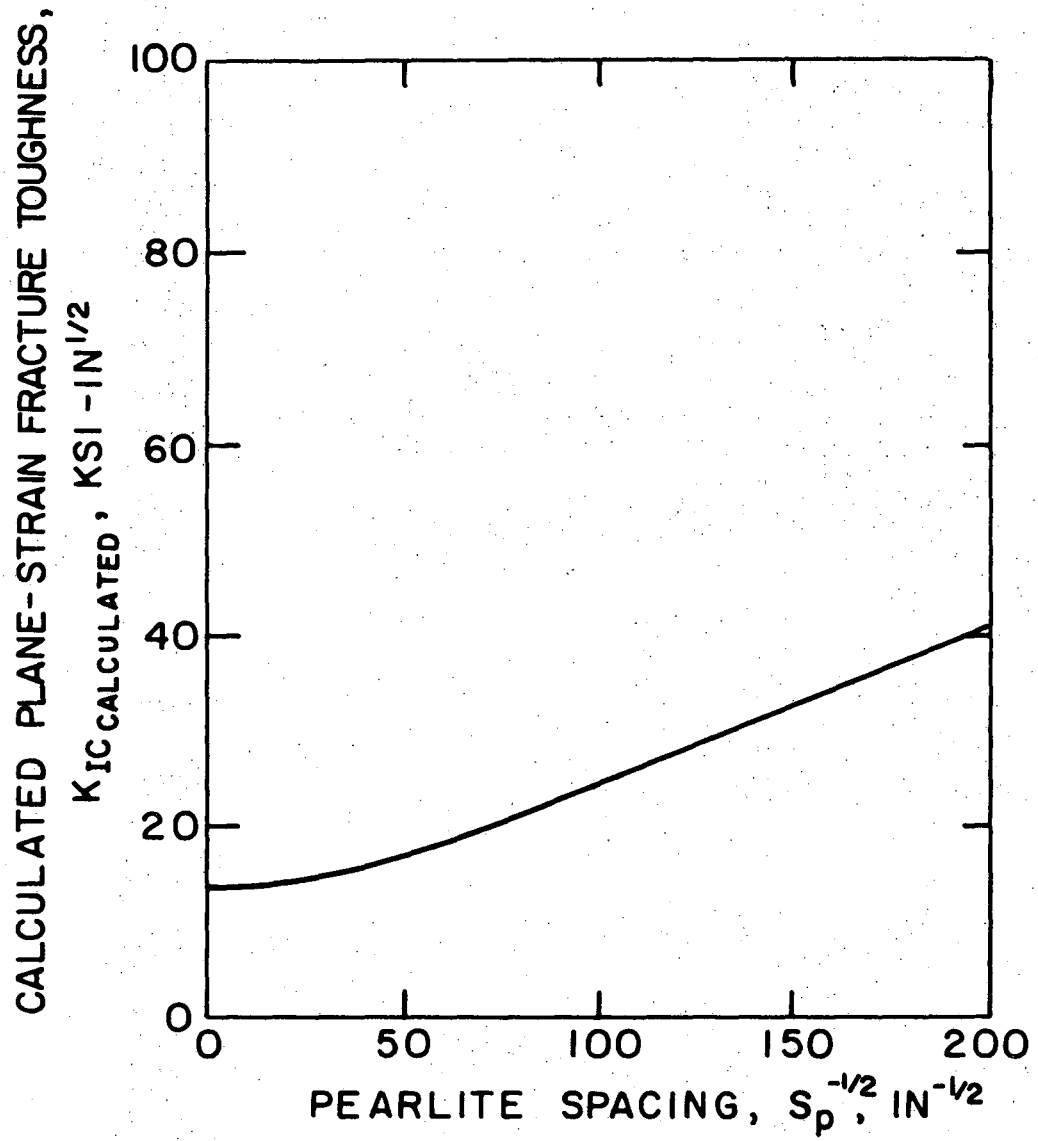

XBL 6910-5869

Fig. 59

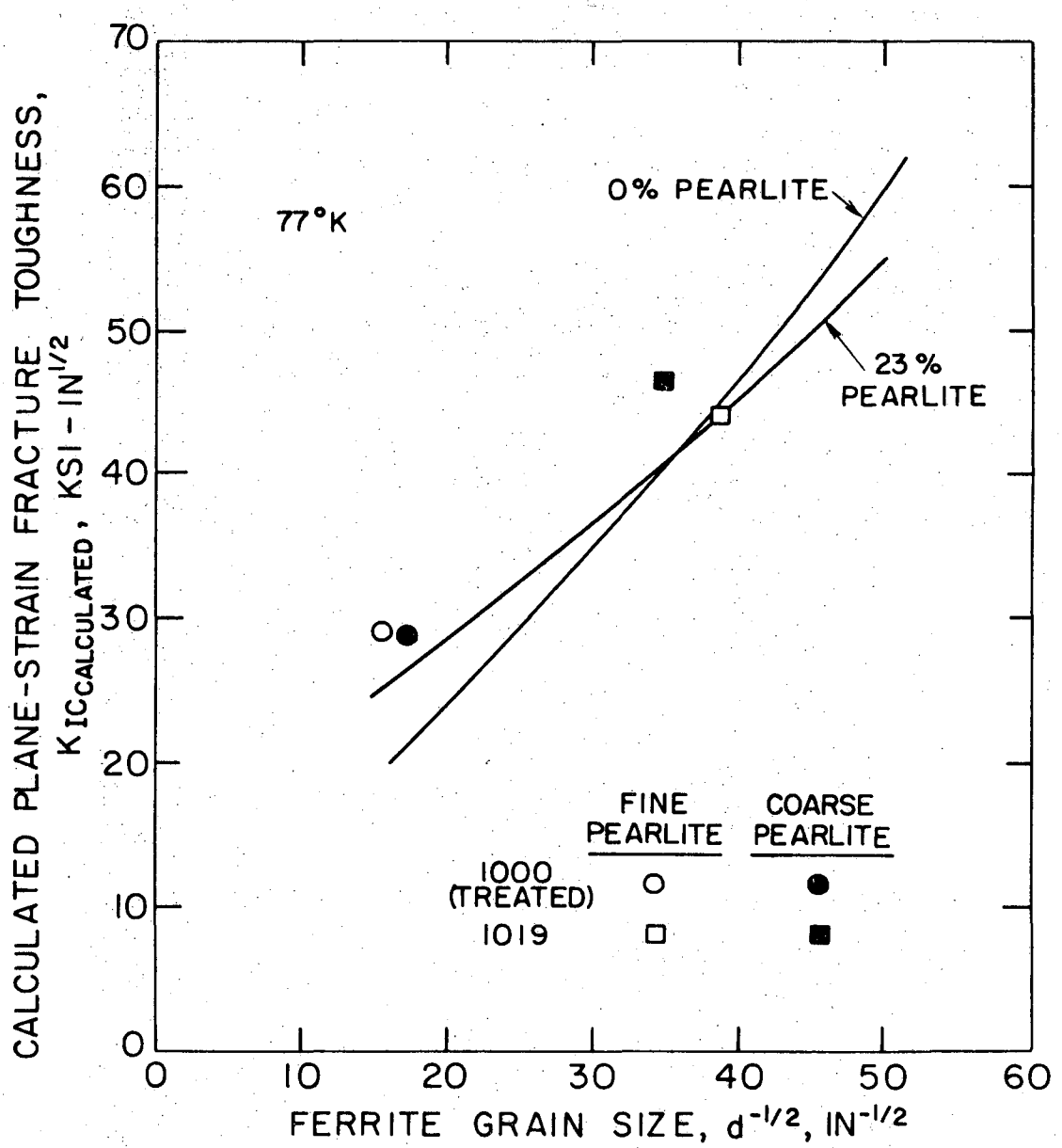

XBL 6910-5891

Fig. 60

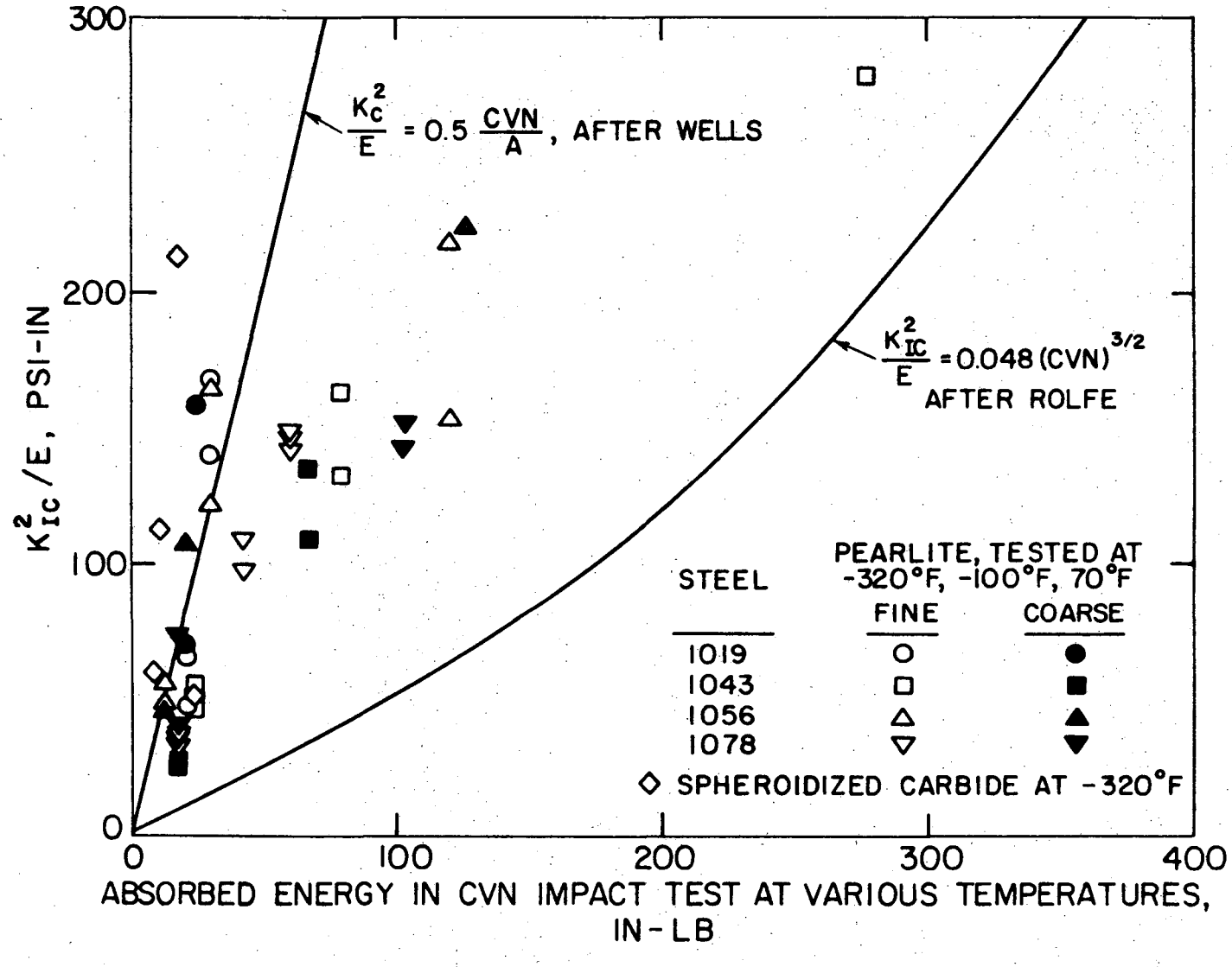

XBL 6910-5868

Fig. 61

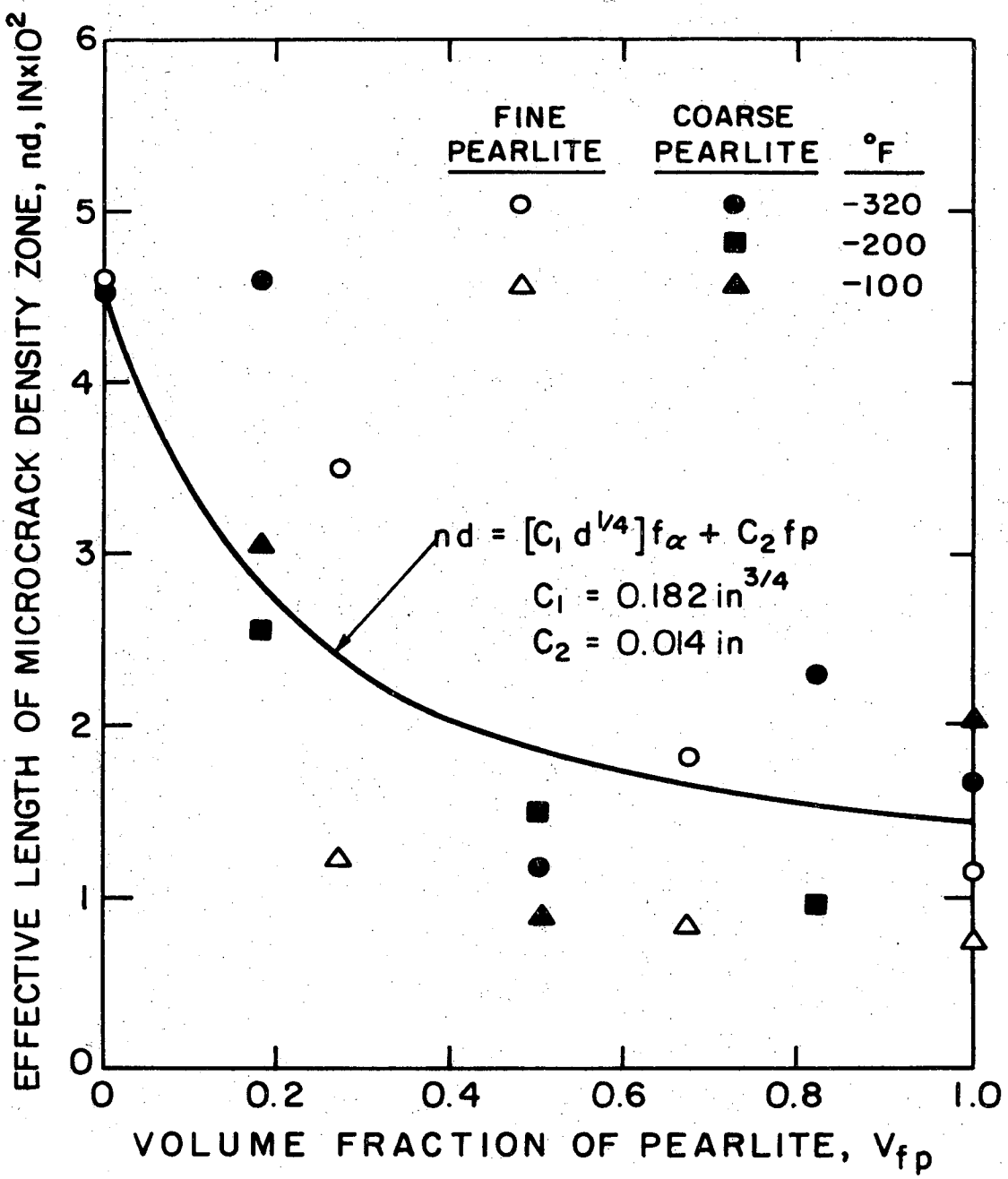

XBL 6910-5878

Fig. 62

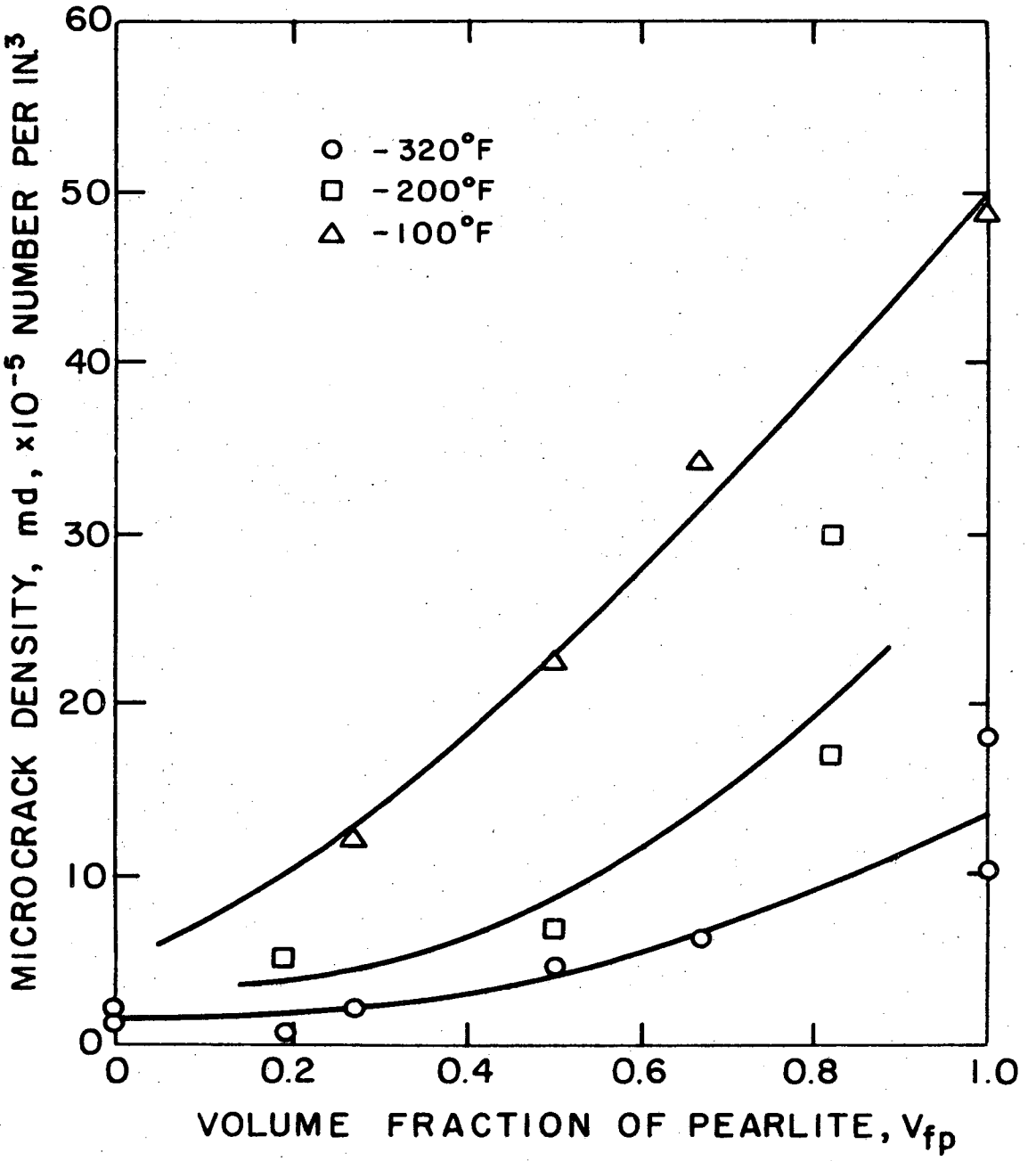

XBL 6910-5879

Fig. 63

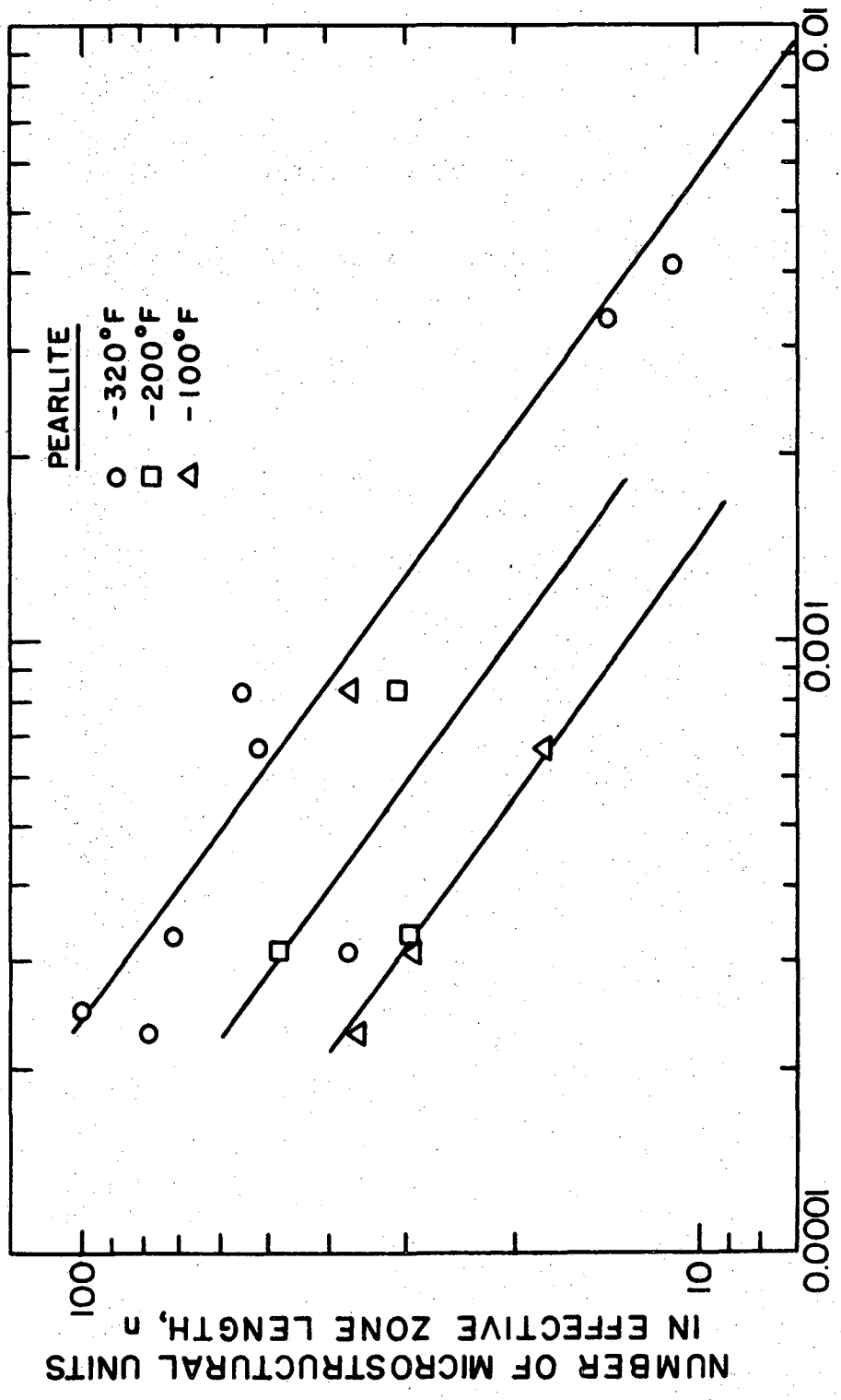

XBL 6910-5888

Fig. 64

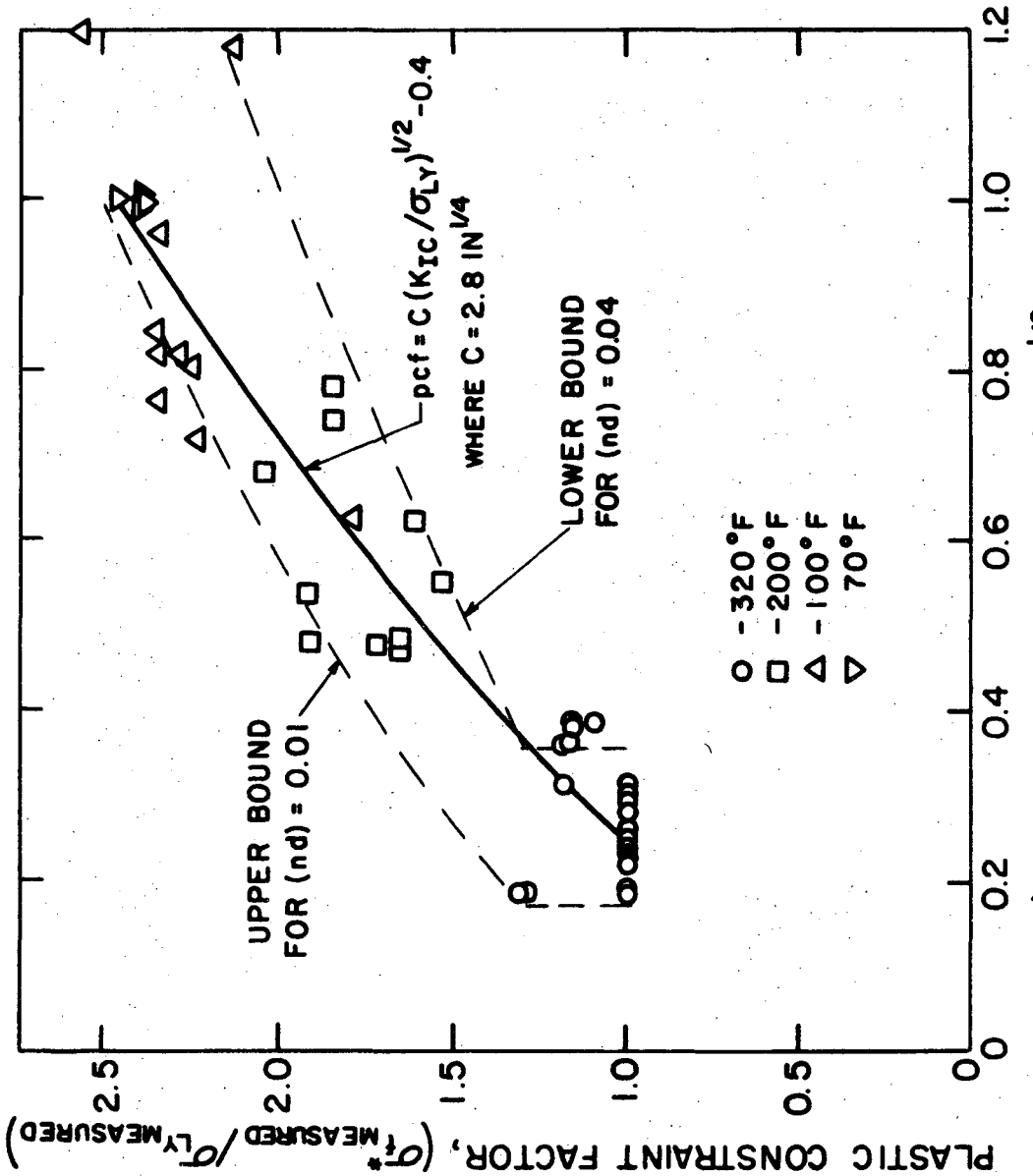

XBL 6910-5880

Fig. 65

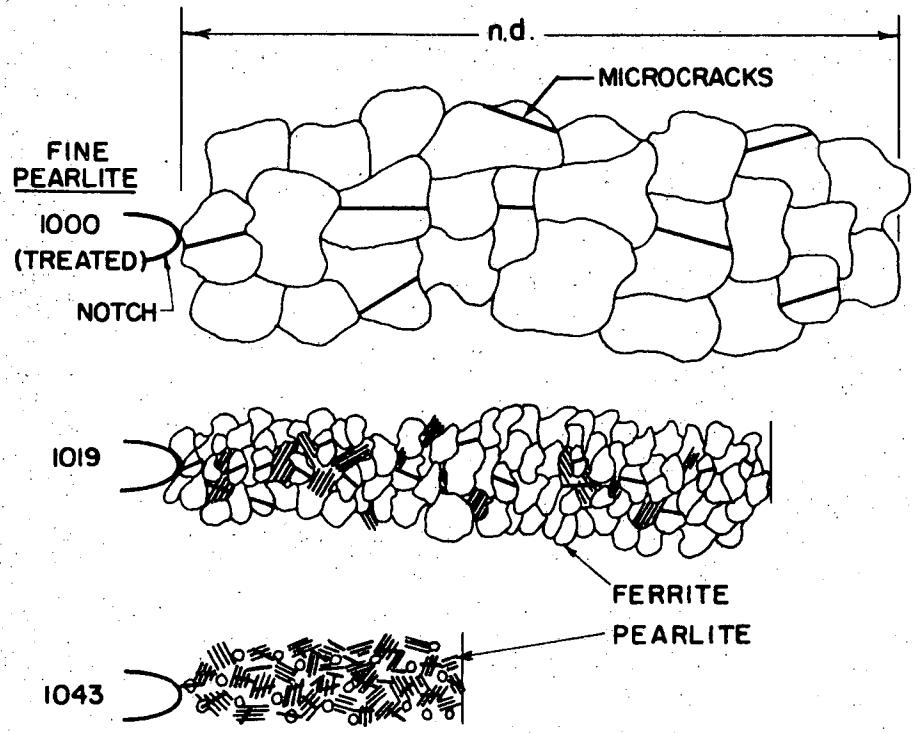

	CALCULATED VALUES AT -320°F				
	1000	1019	1043	1056	1078
MICROCRACK DENSITY m.d.x 10^5	1.38	2.02	6.18	4.0	18.2
EFFECTIVE LENGTH OF MICROCRACK DENSITY ZONE n.d.	0.046	0.035	0.018	0.025	0.0115

XBL 6910-5889

Fig. 66

TECHNICAL INFORMATION DIVISION
LAWRENCE RADIATION LABORATORY
UNIVERSITY OF CALIFORNIA
BERKELEY, CALIFORNIA 94720